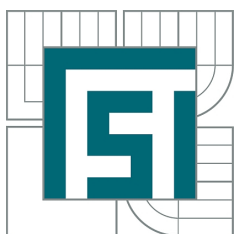


VYSOKÉ UČENÍ TECHNICKÉ V BRNĚ  
BRNO UNIVERSITY OF TECHNOLOGY



FAKULTA STROJNÍHO INŽENÝRSTVÍ  
ÚSTAV FYZIKÁLNÍHO INŽENÝRSTVÍ  
FACULTY OF MECHANICAL ENGINEERING  
INSTITUTE OF PHYSICAL ENGINEERING

## MODELOVÁNÍ ŠÍŘENÍ POVRCHOVÝCH PLAZMONŮ V GRAFENU MODELING OF SURFACE-PLASMON PROPAGATION IN GRAPHENE

DIPLOMOVÁ PRÁCE  
MASTER'S THESIS

AUTOR PRÁCE  
AUTHOR

Bc. MARTIN HRTOŇ

VEDOUČÍ PRÁCE  
SUPERVISOR

Ing. RADEK KALOUSEK, Ph.D.



## **Abstrakt**

Tato diplomová práce se zabývá transportními a optickými vlastnostmi grafenu, a to zejména v kontextu jejich možné ovládní pomocí elektrostatického gatování. Autor představuje návrh experimentu, který by demonstroval praktické možnosti využití grafenu v oblasti aktivní plazmoniky. Těžiště práce spočívá v počítačových simulacích rozptylu světla na hybridních strukturách na bázi grafenu a drahých kovů. Rozptylové vlastnosti těchto struktur jsou diskutovány v závislosti na hustotě volných nosičů náboje v grafenu. Autor dochází k závěru, že navrhovaný způsob řízení odezvy osamocené plazmonické antény elektrostatickým gatováním je nedostačující a k zvýšení tohoto efektu bude potřeba najít jinou vhodnější konfiguraci.

## **Summary**

The diploma thesis provides an introduction to electronic and optical properties of graphene, emphasizing their tunability through the ambipolar field effect. Furthermore, an experiment, which would demonstrate the possible utilization of graphene in active plasmonics, is presented. The author focuses on light scattering simulations involving hybrid plasmonic structures made of noble metals and graphene. The scattering properties of those structures and their dependence on the density of free charge carriers in graphene are investigated. The author concludes that the proposed tuning of the response of a single metallic antenna through the electrostatic doping of graphene proves to be inefficient, and a more elaborate configuration will be required to enhance the effect and achieve the desired control.

## **Klíčová slova**

grafen, aktivní plazmonika, laditelné rozptylové vlastnosti

## **Keywords**

graphene, active plasmonics, tunable scattering properties



Hereby I declare that I have created this work autonomously under a scientific supervision of Ing. Radek Kalousek, Ph.D. All sources, references and literature used or excerpted during the elaboration of this work are properly cited and listed in the complete reference.

Bc. Martin Hrtoň



I would like to thank my supervisor Ing. Radek Kalousek, Ph.D. for his valuable suggestions and inspiring discussions. Furthermore, I would like to appreciate the help of Prof. RNDr. Petr Dub, CSc. and the technical support provided by the research group of Prof. RNDr. Miloslav Ohlídál, CSc. Last but not least, this thesis would never see the light without the boundless support of my family.

Bc. Martin Hrtoň



# Contents

<b>Introduction</b>	<b>3</b>
<b>1 Optical properties of graphene</b>	<b>5</b>
1.1 Crystal lattice and reciprocal lattice . . . . .	5
1.2 Tight binding method . . . . .	6
1.3 Band structure of graphene . . . . .	8
1.4 Band structure at the Dirac points . . . . .	11
1.5 Electron wavefunctions at the Dirac points . . . . .	14
1.6 Self consistent field method . . . . .	16
1.7 Dynamical conductivity of graphene . . . . .	21
1.8 Plasmons in graphene . . . . .	28
<b>2 Fabrication of graphene</b>	<b>33</b>
<b>3 Applications of graphene</b>	<b>35</b>
<b>4 Proposed experimental setup: Motivation</b>	<b>37</b>
<b>5 Calculations based on the transformation optics method</b>	<b>43</b>
5.1 Conformal transformations . . . . .	43
5.2 Geometry of the problem . . . . .	44
5.3 Potentials . . . . .	45
5.4 Dyadic Green's functions . . . . .	55
5.5 Results . . . . .	60
<b>6 Calculations based on the boundary element method</b>	<b>65</b>
6.1 Formalism . . . . .	65
6.2 Modeling of graphene and substrates in BEM . . . . .	67
6.3 BEM calculations . . . . .	70
<b>7 Conclusion</b>	<b>77</b>
<b>Appendix A</b>	<b>79</b>
<b>Appendix B</b>	<b>81</b>



# Introduction

Graphene is a transparent, two dimensional crystal composed of carbon atoms arranged into a hexagonal lattice and it can be basically viewed as a limiting case of a graphite crystal only one monolayer thick. Due to its planar structure, graphene possesses several interesting properties like high tensile strength, flexibility and superb free charge carrier mobility. The last property follows from the graphene's unique electronic band structure, in which the valence and the conduction bands are touching each other in a single point, to which it is usually referred as to the Dirac point. Interestingly, the electrons in the vicinity of the Dirac point can be described as massless Dirac fermions, making graphene an intriguing material even for high energy physicists.

In the fields of plasmonics and photonics, graphene draws attention especially due to the possibility of changing dynamically the density of free charge carriers, thus allowing one to tune both its electronic and optical properties. Such ability can find a utilization not only in the current technology of optical modulators, photodetectors, high-frequency transistors and other electric and optoelectronic devices, but it might also lead to a major progress in the area of active plasmonics and optical computation.

This thesis concerns mainly with the intriguing concept of hybrid plasmonic structures with a tunable response to the external electromagnetic radiation. The control is achieved through the electrostatic doping of graphene using the ambipolar field effect. The author attempts to estimate theoretically the strength of the interaction between a single plasmonic antenna made of a noble metal and electrostatically doped graphene by means of light scattering simulations. The calculations take into account neither the influence of the gating electrode nor the possible changes in the electronic structure of graphene due to the presence of the metal. Especially the latter might be of great importance and the scientific community is currently striving to shed some light on the issue. Nevertheless, the author believes that the presented results capture the main features of the response of such hybrid structures and that this thesis might help to determine the future course of the research in this area at our institute.

Since the theory behind the optical properties of graphene is quite extensive and the author did not encounter a text, which would present their complete description in a comprehensible and compact form, Chapter 1 provides the reader with an easy to follow derivation of the dynamical conductivity and optical properties of graphene, with emphasis on its metallic character enabling the existence of plasmonic surface modes.

Chapters 2 and 3 present a short overview of the fabrication methods and possible applications of graphene.

One of the goals of this thesis is to propose an experiment, which would demonstrate the possible control over the plasmonic resonance of ordinary metallic antennas through the variations of the doping level in graphene. Chapter 4 introduces a hypothetical device allowing one to tune the angle of refraction at interfaces by means of graphene based plasmonic structures.

The core of the thesis resides in the light scattering simulations involving hybrid structures made of noble metals and graphene. Chapters 5 and 6 give the reader a brief introduction to two different techniques, which were employed to calculate the scattering properties of several model structures. The results of the simulations are summarized in Conclusion.

*CONTENTS*

# 1. Optical properties of graphene

For a long time, graphene was considered to be an unstable, hypothetical material, interesting only from the theoretical point of view. Presently, it is one of the most intensively researched objects with a possibly far-reaching impact on the future development of electronic and optoelectronic devices. This chapter concerns with the electronic band structure and derivation of the frequency-dependent conductivity of graphene, which is necessary for calculations of radiation scattering from structures involving graphene.

## 1.1. Crystal lattice and reciprocal lattice

Graphene consists of carbon atoms, the elementary building block of organic molecules and living organisms. In the ground state, the electronic structure of a carbon atom is in the language of chemistry standardly written as  $1s^2 2s^2 2p^2$  so that two of the total of six electrons are enclosed in the inner K shell and the four remaining valence electrons occupy the L shell and ensure the bonding with surrounding atoms.

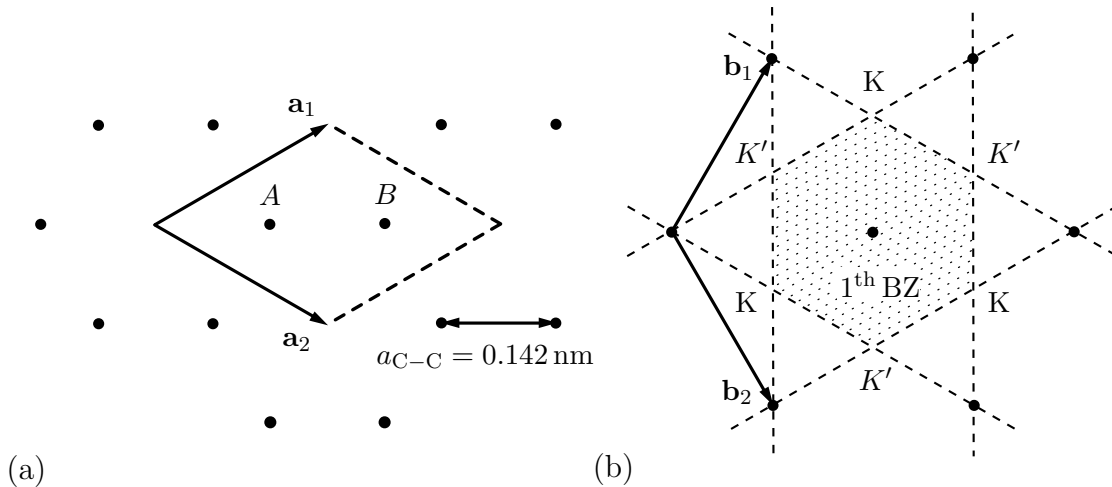


Figure 1.1: (a) The honeycomb arrangement of carbon atoms in graphene with spacing  $a_{C-C} = 0.142$  nm. The primitive unit cell contains two inequivalent carbon atoms (marked  $A$  and  $B$ ) and it is defined through the lattice vectors  $\mathbf{a}_1$  and  $\mathbf{a}_2$ . (b) The reciprocal lattice of graphene. The high-symmetry corner points of the first Brillouin zone ( $1^{\text{th}}$  BZ) are marked  $K$  and  $K'$ .

The carbon atoms in graphene are arranged into a honeycomb (hexagonal) lattice with a distance  $a_{C-C} = 0.142$  nm between each two carbon atoms (Fig. 1.1 (a)). They are found to be in the state of  $sp^2$  hybridization, which means that the  $2s$ ,  $2p_x$  and  $2p_y$  orbitals superpose to form three equivalent  $\sigma$  orbitals (Fig. 1.2) oriented in the  $xy$  plane and "protruding" in the directions mutually separated by an angle of  $120^\circ$ . Those three  $\sigma$  orbitals (each of them occupied by one electron) interact with the  $\sigma$  orbitals of the three closest carbon atoms and form strong covalent  $\sigma$  bonds, which are responsible for the high durability and tensile strength of graphene. The remaining electron occupying the  $2p_z$  orbital, unaffected by the hybridization and oriented out of the crystal plane, interacts with the  $2p_z$  orbitals of neighbouring carbon atoms forming weaker and delocalized  $\pi$  bonds.

Although the crystal structure of graphene is commonly described by the honeycomb lattice, its vertices do not form the basis of primitive vectors of a Bravais cell, since the lattice appears differently from two adjacent carbon sites. There exists a suitable primitive unit cell with a basis containing the two inequivalent carbon atoms (marked  $A$  and  $B$ ) and primitive vectors  $\mathbf{a}_1 = \left(\frac{\sqrt{3}a}{2}, \frac{a}{2}\right)$

## 1.2. TIGHT BINDING METHOD

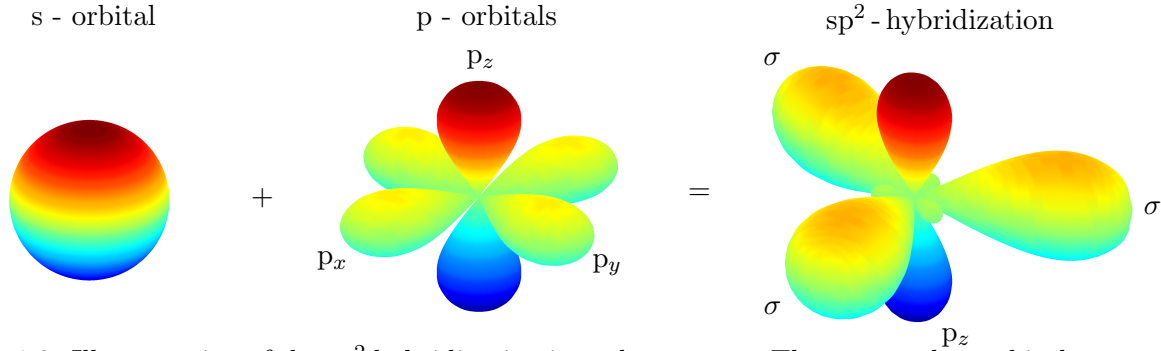


Figure 1.2: Illustration of the  $sp^2$  hybridization in carbon atoms. The  $s$ ,  $p_x$  and  $p_y$  orbitals superpose to form three equivalent  $\sigma$  orbitals. The  $p_z$  orbital remains unaffected by this process.

and  $\mathbf{a}_2 = \left(\frac{\sqrt{3}a}{2}, -\frac{a}{2}\right)$  as depicted in Figure 1.1 (a) (the magnitude of the vectors has been denoted  $a = |\mathbf{a}_1| = |\mathbf{a}_2| = \sqrt{3}a_{C-C}$ ). The reciprocal lattice vectors  $\mathbf{b}_1$  and  $\mathbf{b}_2$  can be derived from the primitive vectors

$$\mathbf{b}_1 = 2\pi \frac{\mathbf{a}_2 \times \mathbf{a}_3}{\mathbf{a}_1 \cdot (\mathbf{a}_2 \times \mathbf{a}_3)} = \left(\frac{2\pi}{\sqrt{3}a}, \frac{2\pi}{a}\right), \quad (1.1)$$

$$\mathbf{b}_2 = 2\pi \frac{\mathbf{a}_3 \times \mathbf{a}_1}{\mathbf{a}_1 \cdot (\mathbf{a}_2 \times \mathbf{a}_3)} = \left(\frac{2\pi}{\sqrt{3}a}, -\frac{2\pi}{a}\right), \quad (1.2)$$

where the out-of-plane primitive vector tends to infinity  $\mathbf{a}_3 \rightarrow \infty$ . The first Brillouin zone, resp. the primitive unit cell in the reciprocal space, is then obtained by the Wigner-Seitz construction, where the boundary of the cell for the respective lattice point is given by the region of the reciprocal space that is closer to that point than to any other point of the lattice (Fig. 1.1 (b)).

## 1.2. Tight binding method

The band structure of graphene within the first Brillouin zone can be calculated using the so called tight binding method, which relies on the Bloch's theorem and which is in many aspects similar to the calculations of band structure for nearly free conducting electrons in metals. The following introduction to this method and its application to graphene are built mainly on certain passages from Mermin and Ashcroft [4] (Chap. 10) and Saito et al. [29] (Chap. 2).

First let us assume a periodic crystal potential  $U(\mathbf{r} + \mathbf{R}) = U(\mathbf{r})$ , where  $\mathbf{r}$  is a position vector and  $\mathbf{R}$  spans over all the crystal lattice points. Then according to the Bloch's theorem, the electron wavefunction  $\Phi$  satisfying the one-electron Hamiltonian  $H = -\frac{\hbar^2}{2m}\nabla^2 + U(\mathbf{r})$  can be chosen in the form

$$\Phi^{(\mathbf{k})}(\mathbf{r} + \mathbf{R}) = e^{i\mathbf{k}\cdot\mathbf{R}}\Phi^{(\mathbf{k})}(\mathbf{r}), \quad (1.3)$$

where  $\mathbf{k}$  is a wavevector associated with the particular wavefunction. Clearly, Equation (1.3) satisfies the requirement that the probability density of finding an electron  $|\Phi|^2$  is periodic over the lattice.

The tight binding approximation is based on the assumption that the electron wavefunctions  $\psi$  satisfying the full periodic crystal Hamiltonian  $H$  differ only slightly from those of a single atom, thus they can be approximated by an appropriate superposition of atomic wavefunctions  $\varphi$ . This is quite the opposite compared to the case of the nearly free electron model for metals, where the wavefunctions are expressed in terms of plane waves. The assumptions for the tight binding approximation mentioned above are met for crystals, where the electrons are tightly bound to their respective atoms and the

crystal potential  $H$  does not substantially deviate from the atomic potential  $H_{\text{at}}$  within the range of the electron wavefunction  $\varphi$ .

A suitable electron wavefunction satisfying the Bloch's theorem and having the form prescribed by the tight binding approximation can be written as

$$\Phi_j^{(\mathbf{k})}(\mathbf{r}) = \frac{1}{\sqrt{N}} \sum_{\mathbf{R}_j}^N e^{i\mathbf{k}\cdot\mathbf{R}_j} \varphi_j(\mathbf{r} - \mathbf{R}_j), \quad (1.4)$$

where  $\varphi_j$  is the  $j$ -th atomic wavefunction,  $\mathbf{R}_j$  is the position vector spanning all the associated atomic sites and  $N$  is the number of the respective atoms in the crystal (this can differ from the total number of atoms in the crystal, since we can have a multiple-atomic basis). The fact that the wavefunction given by Equation (1.4) indeed obeys the Bloch's theorem can be straightforwardly shown by inserting it into Equation (1.3)

$$\begin{aligned} \Phi_j^{(\mathbf{k})}(\mathbf{r} + \mathbf{R}) &= \frac{1}{\sqrt{N}} \sum_{\mathbf{R}_j}^N e^{i\mathbf{k}\cdot\mathbf{R}_j} \varphi_j(\mathbf{r} + \mathbf{R} - \mathbf{R}_j) = \frac{1}{\sqrt{N}} \sum_{\mathbf{R}_j}^N e^{i\mathbf{k}\cdot(\mathbf{R}_j - \mathbf{R})} e^{i\mathbf{k}\cdot\mathbf{R}} \varphi_j(\mathbf{r} - (\mathbf{R}_j - \mathbf{R})) = \\ &= e^{i\mathbf{k}\cdot\mathbf{R}} \frac{1}{\sqrt{N}} \sum_{\mathbf{R}_j}^N e^{i\mathbf{k}\cdot\mathbf{R}_j} \varphi_j(\mathbf{r} - \mathbf{R}_j) = e^{i\mathbf{k}\cdot\mathbf{R}} \Phi_j^{(\mathbf{k})}(\mathbf{r}), \end{aligned}$$

where we have used the property  $\sum_{\mathbf{R}_j - \mathbf{R}} = \sum_{\mathbf{R}_j}$ .

Finally, the crystal wavefunction  $\psi$  is given by a linear combination of all the Bloch's atomic wavefunctions (Eq. (1.4))

$$\psi_i^{(\mathbf{k})}(\mathbf{r}) = \sum_j^n C_{ij}^{(\mathbf{k})} \Phi_j^{(\mathbf{k})}(\mathbf{r}), \quad (1.5)$$

where coefficients  $C_{ij}^{(\mathbf{k})}$  are yet to be determined and index  $i$  spans over the  $n$  bands, which are formed as the result of the superposition of  $n$  different atomic wavefunctions.

The desired band structure described by the energy dispersion  $e^{(\mathbf{k})}$  is now obtained as the expectation value of the crystal Hamiltonian

$$E_i^{(\mathbf{k})} = \frac{\langle \psi_i^{(\mathbf{k})} | H | \psi_i^{(\mathbf{k})} \rangle}{\langle \psi_i^{(\mathbf{k})} | \psi_i^{(\mathbf{k})} \rangle}. \quad (1.6)$$

Expressing the wavefunction  $\psi_i^{(\mathbf{k})}$  in terms of the Bloch's atomic wavefunctions (Eq. (1.4)) leads to

$$E_i^{(\mathbf{k})} = \frac{\langle \sum_j^n C_{ij}^{(\mathbf{k})} \Phi_j^{(\mathbf{k})} | H | \sum_{j'}^n C_{ij'}^{(\mathbf{k})} \Phi_{j'}^{(\mathbf{k})} \rangle}{\langle \sum_j^n C_{ij}^{(\mathbf{k})} \Phi_j^{(\mathbf{k})} | \sum_{j'}^n C_{ij'}^{(\mathbf{k})} \Phi_{j'}^{(\mathbf{k})} \rangle} = \frac{\sum_{j,j'}^n C_{ij}^{*(\mathbf{k})} C_{ij'}^{(\mathbf{k})} \langle \Phi_j^{(\mathbf{k})} | H | \Phi_{j'}^{(\mathbf{k})} \rangle}{\sum_{j,j'}^n C_{ij}^{*(\mathbf{k})} C_{ij'}^{(\mathbf{k})} \langle \Phi_j^{(\mathbf{k})} | \Phi_{j'}^{(\mathbf{k})} \rangle} = \frac{\sum_{j,j'}^n C_{ij}^{*(\mathbf{k})} C_{ij'}^{(\mathbf{k})} H_{jj'}^{(\mathbf{k})}}{\sum_{j,j'}^n C_{ij}^{*(\mathbf{k})} C_{ij'}^{(\mathbf{k})} S_{jj'}^{(\mathbf{k})}}, \quad (1.7)$$

$$S_{jj'}^{(\mathbf{k})} = \langle \Phi_j^{(\mathbf{k})} | \Phi_{j'}^{(\mathbf{k})} \rangle, \quad H_{jj'}^{(\mathbf{k})} = \langle \Phi_j^{(\mathbf{k})} | H | \Phi_{j'}^{(\mathbf{k})} \rangle, \quad (1.8)$$

where the elements of the overlap matrix  $S_{jj'}^{(\mathbf{k})}$  and the transfer matrix  $H_{jj'}^{(\mathbf{k})}$  assess the orthogonality and the energy transfer between the pair of states  $\Phi_j^{(\mathbf{k})}$ ,  $\Phi_{j'}^{(\mathbf{k})}$  respectively.

### 1.3. BAND STRUCTURE OF GRAPHENE

In the spirit of the variation principle (Griffiths [15], p. 293), the ground state of the system is obtained by looking for the minimal value of the energy  $E_i^{(\mathbf{k})}$  with respect to the coefficients  $C_{ij}^{(\mathbf{k})}$

$$\frac{\partial E_i^{(\mathbf{k})}}{\partial C_{ij}^{*(\mathbf{k})}} = \frac{\sum_{j'}^n C_{ij'}^{(\mathbf{k})} H_{jj'}^{(\mathbf{k})}}{\sum_{j,j'}^n C_{ij}^{*(\mathbf{k})} C_{ij'}^{(\mathbf{k})} S_{jj'}^{(\mathbf{k})}} - E_i^{(\mathbf{k})} \frac{\sum_{j'}^n C_{ij'}^{(\mathbf{k})} S_{jj'}^{(\mathbf{k})}}{\sum_{j,j'}^n C_{ij}^{*(\mathbf{k})} C_{ij'}^{(\mathbf{k})} S_{jj'}^{(\mathbf{k})}} = 0, \quad (1.9)$$

leading to a homogenous system of  $n$  linear equations for each  $i$

$$\sum_{j'}^n \left( H_{jj'}^{(\mathbf{k})} - E_i^{(\mathbf{k})} S_{jj'}^{(\mathbf{k})} \right) C_{ij'}^{(\mathbf{k})} = 0, \quad j = 1, 2 \dots n. \quad (1.10)$$

Rewriting the above set of equations in terms of matrices and column vectors simplifies the notation

$$\mathcal{H}^{(\mathbf{k})} = \begin{pmatrix} H_{11}^{(\mathbf{k})} & H_{12}^{(\mathbf{k})} & \dots \\ H_{21}^{(\mathbf{k})} & H_{22}^{(\mathbf{k})} & \dots \\ \vdots & \vdots & \ddots \end{pmatrix}, \quad \mathcal{S}^{(\mathbf{k})} = \begin{pmatrix} S_{11}^{(\mathbf{k})} & S_{12}^{(\mathbf{k})} & \dots \\ S_{21}^{(\mathbf{k})} & S_{22}^{(\mathbf{k})} & \dots \\ \vdots & \vdots & \ddots \end{pmatrix}, \quad \mathcal{C}_i^{(\mathbf{k})} = \begin{pmatrix} C_{i1}^{(\mathbf{k})} \\ C_{i2}^{(\mathbf{k})} \\ \vdots \end{pmatrix}, \quad (1.11)$$

$$\left( \mathcal{H}^{(\mathbf{k})} - E_i^{(\mathbf{k})} \mathcal{S}^{(\mathbf{k})} \right) \mathcal{C}_i^{(\mathbf{k})} = 0. \quad (1.12)$$

Equation (1.12) has a nontrivial solution only if the determinant of the expression in the brackets is equal to zero

$$\det \left( \mathcal{H} - E_i^{(\mathbf{k})} \mathcal{S} \right) = 0. \quad (1.13)$$

Equation (1.13) is known as the secular equation and for given values of the transfer and overlap matrices it allows one to directly calculate the energy dispersion  $E_i^{(\mathbf{k})}$ .

### 1.3. Band structure of graphene

Application of the tight binding method to graphene is straightforward. Since electric and optical properties of materials are governed mainly by the electronic states at Fermi level, one needs to take into account only those atomic orbitals, which contribute to the density of states near the Fermi level. In the case of graphene, the electronic bands arising from the strongly bound  $\sigma$  electrons are found to be well below the Fermi level, thus calculations incorporating only  $\pi$  orbitals should capture all the important features of the graphene's electrodynamical response.

The graphene's primitive unit cell contains two inequivalent carbon atoms (see Section 1.1), each contributing to the crystal wavefunction by one atomic  $\pi$  orbital. Invoking Equations (1.4) and (1.5), the crystal wavefunction  $\psi_i^{(\mathbf{k})}$  can be written as

$$\psi_i^{(\mathbf{k})}(\mathbf{r}) = a_i(\mathbf{k}) \sum_{\mathbf{R}_A}^N \frac{e^{i\mathbf{k} \cdot \mathbf{R}_A}}{\sqrt{N}} \varphi_A(\mathbf{r} - \mathbf{R}_A) + b_i(\mathbf{k}) \sum_{\mathbf{R}_B}^N \frac{e^{i\mathbf{k} \cdot \mathbf{R}_B}}{\sqrt{N}} \varphi_B(\mathbf{r} - \mathbf{R}_B), \quad (1.14)$$

where the coefficients  $a_i(\mathbf{k})$  and  $b_i(\mathbf{k})$  account for the coefficients  $C_{ij}^{(\mathbf{k})}$ ,  $\mathbf{R}_A$ ,  $\mathbf{R}_B$  are the position vectors of the two inequivalent atomic sites and  $\varphi_A$ ,  $\varphi_B$  are the respective atomic  $\pi$  orbital wavefunctions.

The next step is the evaluation of the transfer and overlap matrices. Insertion of the crystal wavefunction  $\psi_i^{(\mathbf{k})}$  into Equations (1.8) leads to

$$H_{\alpha\beta}^{(\mathbf{k})} = \sum_{\mathbf{R}_\alpha, \mathbf{R}'_\beta} \frac{e^{i\mathbf{k}\cdot(\mathbf{R}'_\beta - \mathbf{R}_\alpha)}}{N} \langle \varphi_\alpha(\mathbf{r} - \mathbf{R}_\alpha) | H | \varphi_\beta(\mathbf{r} - \mathbf{R}'_\beta) \rangle, \quad (1.15)$$

$$S_{\alpha\beta}^{(\mathbf{k})} = \sum_{\mathbf{R}_\alpha, \mathbf{R}'_\beta} \frac{e^{i\mathbf{k}\cdot(\mathbf{R}'_\beta - \mathbf{R}_\alpha)}}{N} \langle \varphi_\alpha(\mathbf{r} - \mathbf{R}_\alpha) | \varphi_\beta(\mathbf{r} - \mathbf{R}'_\beta) \rangle, \quad (1.16)$$

where the indices  $\alpha, \beta = A, B$  run over all the four possible combinations.

Since the atomic wavefunctions  $\varphi_{A,B}$  are appreciable only in a limited region around their respective atomic cores, one does not have to calculate the interaction with all the carbon atoms in the crystal, but to some extent it will suffice to take into account only the nearest neighbours. In mathematical terms

$$\varphi_\alpha(\mathbf{r} - \mathbf{R}_\alpha) \approx 0 \quad \text{for } \mathbf{R}_\alpha \neq 0, \quad (1.17)$$

$$\varphi_\alpha(\mathbf{r} - \mathbf{R}_\beta) \neq 0 \quad \text{for } \mathbf{R}_\beta = \boldsymbol{\delta}_\nu^{\alpha\beta}, \quad \alpha \neq \beta, \quad \nu = 1, 2, 3, \quad (1.18)$$

$$\boldsymbol{\delta}_1^{AB} = \left( \frac{a}{\sqrt{3}}, 0 \right), \quad \boldsymbol{\delta}_2^{AB} = \left( -\frac{a}{2\sqrt{3}}, \frac{a}{2} \right), \quad \boldsymbol{\delta}_3^{AB} = \left( -\frac{a}{2\sqrt{3}}, -\frac{a}{2} \right), \quad \boldsymbol{\delta}_\nu^{BA} = -\boldsymbol{\delta}_\nu^{AB}, \quad (1.19)$$

where  $\boldsymbol{\delta}_\nu^{\alpha\beta}$  are the position vectors of the nearest atoms with respect to the central atom (Fig. 1.3).

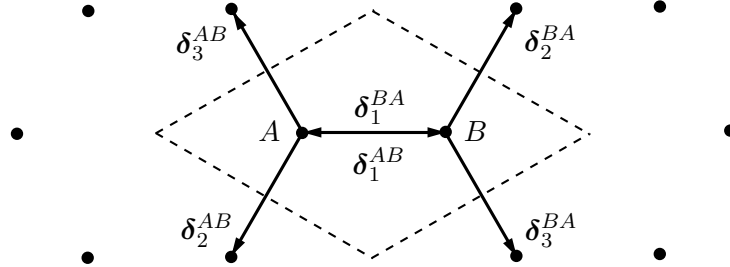


Figure 1.3: The nearest neighbour carbon atoms and their position vectors  $\boldsymbol{\delta}_\nu^{\alpha\beta}$  with respect to the central atoms marked  $A$  and  $B$ .

Adopting the above assumptions, the diagonal elements of the transfer and overlap matrices are readily evaluated

$$\begin{aligned} H_{AA}^{(\mathbf{k})} = H_{BB}^{(\mathbf{k})} &= \frac{1}{N} \sum_{\mathbf{R}_\alpha = \mathbf{R}'_\alpha} e^{i\mathbf{k}\cdot(\mathbf{R}'_\alpha - \mathbf{R}_\alpha)} \langle \varphi_\alpha(\mathbf{r} - \mathbf{R}_\alpha) | H | \varphi_\alpha(\mathbf{r} - \mathbf{R}'_\alpha) \rangle = \\ &= \frac{1}{N} \sum_{\mathbf{R}_\alpha} \langle \varphi_\alpha(\mathbf{r} - \mathbf{R}_\alpha) | H | \varphi_\alpha(\mathbf{r} - \mathbf{R}_\alpha) \rangle = E_{2p}, \end{aligned} \quad (1.20)$$

$$\begin{aligned} S_{AA}^{(\mathbf{k})} = S_{BB}^{(\mathbf{k})} &= \frac{1}{N} \sum_{\mathbf{R}_\alpha = \mathbf{R}'_\alpha} e^{i\mathbf{k}\cdot(\mathbf{R}'_\alpha - \mathbf{R}_\alpha)} \langle \varphi_\alpha(\mathbf{r} - \mathbf{R}_\alpha) | \varphi_\alpha(\mathbf{r} - \mathbf{R}'_\alpha) \rangle = \\ &= \frac{1}{N} \sum_{\mathbf{R}_\alpha} \langle \varphi_\alpha(\mathbf{r} - \mathbf{R}_\alpha) | \varphi_\alpha(\mathbf{r} - \mathbf{R}_\alpha) \rangle = 1, \end{aligned} \quad (1.21)$$

### 1.3. BAND STRUCTURE OF GRAPHENE

where  $E_{2p}$  denotes the energy, which the 2p orbital acquires in the crystal potential. Furthermore, the assumption that the atomic wavefunctions  $\varphi_{A,B}$  are normalized to one has been made.

According to Equation (1.18), for the evaluation of the off-diagonal elements of the transfer and overlap matrices one needs to consider only the three closest carbon atoms with position vectors  $\delta_\nu^{\alpha\beta}$

$$\begin{aligned} H_{AB}^{(\mathbf{k})} &= \sum_{\nu=1}^3 \frac{1}{N} \sum_{\mathbf{R}_A, \mathbf{R}_A + \delta_\nu^{AB}} e^{i\mathbf{k} \cdot \delta_\nu^{AB}} \langle \varphi_A(\mathbf{r} - \mathbf{R}_A) | H | \varphi_B(\mathbf{r} - \mathbf{R}_A - \delta_\nu^{AB}) \rangle = \\ &= \sum_{\nu=1}^3 e^{i\mathbf{k} \cdot \delta_\nu^{AB}} \langle \varphi_A(\mathbf{r}) | H | \varphi_B(\mathbf{r} - \delta_\nu^{AB}) \rangle, \end{aligned} \quad (1.22)$$

$$\begin{aligned} S_{AB}^{(\mathbf{k})} &= \sum_{\nu=1}^3 \frac{1}{N} \sum_{\mathbf{R}_A, \mathbf{R}_A + \delta_\nu^{AB}} e^{i\mathbf{k} \cdot \delta_\nu^{AB}} \langle \varphi_A(\mathbf{r} - \mathbf{R}_A) | \varphi_B(\mathbf{r} - \mathbf{R}_A - \delta_\nu^{AB}) \rangle = \\ &= \sum_{\nu=1}^3 e^{i\mathbf{k} \cdot \delta_\nu^{AB}} \langle \varphi_A(\mathbf{r}) | \varphi_B(\mathbf{r} - \delta_\nu^{AB}) \rangle. \end{aligned} \quad (1.23)$$

Due to the spatial symmetry of the 2p<sub>z</sub> orbital and the fact that  $|\delta_1^{AB}| = |\delta_2^{AB}| = |\delta_3^{AB}|$ , the two terms  $\langle \varphi_A(\mathbf{r}) | H | \varphi_B(\mathbf{r} - \delta_\nu^{AB}) \rangle$  and  $\langle \varphi_A(\mathbf{r}) | \varphi_B(\mathbf{r} - \delta_\nu^{AB}) \rangle$  have the same value for all the three position vectors  $\delta_\nu^{AB}$  and they can be taken out of the summation over the index  $\nu$ . By denoting those two terms  $t$  and  $s$ , one can rewrite Equations (1.22), (1.23) as

$$H_{AB}^{(\mathbf{k})} = t \sum_{\nu=1}^3 e^{i\mathbf{k} \cdot \delta_\nu^{AB}} = t f^{(\mathbf{k})}, \quad (1.24)$$

$$S_{AB}^{(\mathbf{k})} = s \sum_{\nu=1}^3 e^{i\mathbf{k} \cdot \delta_\nu^{AB}} = s f^{(\mathbf{k})}, \quad (1.25)$$

$$f^{(\mathbf{k})} = \sum_{\nu=1}^3 e^{i\mathbf{k} \cdot \delta_\nu^{AB}} = \exp\left(-i \frac{k_x a}{2\sqrt{3}}\right) \left[ 2 \cos\left(\frac{k_y a}{2}\right) + \exp\left(i \frac{k_x a \sqrt{3}}{2}\right) \right], \quad \mathbf{k} = (k_x, k_y), \quad (1.26)$$

where the factor  $f^{(\mathbf{k})}$  has been introduced.

The matrix elements  $H_{BA}^{(\mathbf{k})}$  and  $S_{BA}^{(\mathbf{k})}$  might be obtained in a similar manner, but because both  $H_{\alpha\beta}^{(\mathbf{k})}$  and  $S_{\alpha\beta}^{(\mathbf{k})}$  are Hermitian, they can be derived from the matrix elements  $H_{AB}^{(\mathbf{k})}$  and  $S_{AB}^{(\mathbf{k})}$  using the property

$$H_{BA}^{(\mathbf{k})} = H_{AB}^{*(\mathbf{k})} = t^* f^{*(\mathbf{k})}, \quad (1.27)$$

$$S_{BA}^{(\mathbf{k})} = S_{AB}^{*(\mathbf{k})} = s^* f^{*(\mathbf{k})}. \quad (1.28)$$

Since the atomic wavefunctions  $\varphi_A(\mathbf{r})$  and  $\varphi_B(\mathbf{r})$  are identical, their order of appearance in the integral  $t = \langle \varphi_A(\mathbf{r}) | H | \varphi_B(\mathbf{r} - \delta_\nu^{AB}) \rangle$ , resp.  $s = \langle \varphi_A(\mathbf{r}) | \varphi_B(\mathbf{r} - \delta_\nu^{AB}) \rangle$  should be interchangeable without a change of its value, which means both  $t = t^*$  and  $s = s^*$  have to be real. Their values can be determined by fitting the energy dispersion curves obtained through the tight binding method to those acquired from the first principle calculations of the graphite band structure. Within this thesis the values  $t = -3.033$  eV and  $s = 0.129$  shall be used.

Once all the elements of the transfer and overlap matrices are known, one can proceed with the calculation of the graphene's energy dispersion  $E_i^{(\mathbf{k})}$  using the secular equation (Eq. (1.13))

$$\begin{aligned} \det \left( \mathcal{H} - E_i^{(\mathbf{k})} \mathcal{S} \right) &= \begin{vmatrix} E_{2p} - E_i^{(\mathbf{k})} & t f^{(\mathbf{k})} - E_i^{(\mathbf{k})} s f^{(\mathbf{k})} \\ t f^{*(\mathbf{k})} - E_i^{(\mathbf{k})} s f^{*(\mathbf{k})} & E_{2p} - E_i^{(\mathbf{k})} \end{vmatrix} = \\ &= \left( E_{2p} - E_i^{(\mathbf{k})} \right)^2 - \left| f^{(\mathbf{k})} \right|^2 \left( t - s E_i^{(\mathbf{k})} \right)^2 = 0. \end{aligned} \quad (1.29)$$

The above equation has two solutions marked as + or -, reflecting the chosen sign of the square root

$$E_{\pm}^{(\mathbf{k})} = \frac{E_{2p} \pm t \sqrt{|f^{(\mathbf{k})}|^2}}{1 \pm s \sqrt{|f^{(\mathbf{k})}|^2}}. \quad (1.30)$$

This expression can be further simplified by setting the zero energy level to  $E_{2p}$  and neglecting the term  $s \sqrt{|f^{(\mathbf{k})}|^2}$  in the denominator against one leading to

$$E_{\pm}^{(\mathbf{k})} = \pm t \sqrt{|f^{(\mathbf{k})}|^2} = \pm t \sqrt{4 \cos^2 \left( \frac{k_y a}{2} \right) + 4 \cos \left( \frac{k_y a}{2} \right) \cos \left( \frac{k_x a \sqrt{3}}{2} \right) + 1}. \quad (1.31)$$

The band structure of graphene throughout the first Brillouin zone given by Equation (1.31) is plotted in Figure 1.4. It consists of two bands, each of which contains the same number of states, that is the number of primitive unit cells in the crystal. Since each of those contributes with two electrons and there can be only two electrons with the same  $E$  and  $\mathbf{k}$  (spin  $\pm \frac{1}{2}$ ), the lower bonding band will be fully occupied in the ground state, whereas the upper antibonding band will be completely empty. The Fermi energy  $E_F$  is, therefore, equal to  $E_{2p} = 0$  and situated at the corner points of the first Brillouin zone labeled as  $K$  and  $K'$ , where the lower band touches the upper band, making graphene a semiconductor with a zero bandgap. The reason for marking the corner points by two different labels is explained later in the text.

Notice that the two energy bands are symmetrical with respect to the Fermi energy only when the terms containing the off-diagonal elements  $s f^{(\mathbf{k})}$  of the overlap matrix are neglected. Inclusion of these terms or terms accounting for the higher order interaction with more distant carbon atoms will lift the electron-hole symmetry.

## 1.4. Band structure at the Dirac points

As stated in the previous section, graphene is in the natural state a zero bandgap semiconductor (as we shall see it is not entirely the truth), thus its electrodynamical response will be governed mainly by the optical processes taking place just at the Fermi level and in its vicinity. Furthermore, to make the calculations of the electrodynamic response feasible, it is necessary to express the electron wavefunctions in terms of simple functions. For these reasons it is wise to focus only on the small regions around the points  $K$  and  $K'$  of the first Brillouin zones and approximate the energy dispersion curves and electron wavefunctions by appropriate expansions around those points.

The first step is to determine the positions of the  $K$  and  $K'$  points within the first Brillouin zone by solving the equation  $E_{\pm}^{(\mathbf{K})} = E_F = 0$ , which is the same as searching for the roots of the equation

$$f^{(\mathbf{K})} = \exp \left( -i \frac{K_x a}{2\sqrt{3}} \right) \left[ 2 \cos \left( \frac{K_y a}{2} \right) + \exp \left( i \frac{K_x a \sqrt{3}}{2} \right) \right] = 0. \quad (1.32)$$

#### 1.4. BAND STRUCTURE AT THE DIRAC POINTS

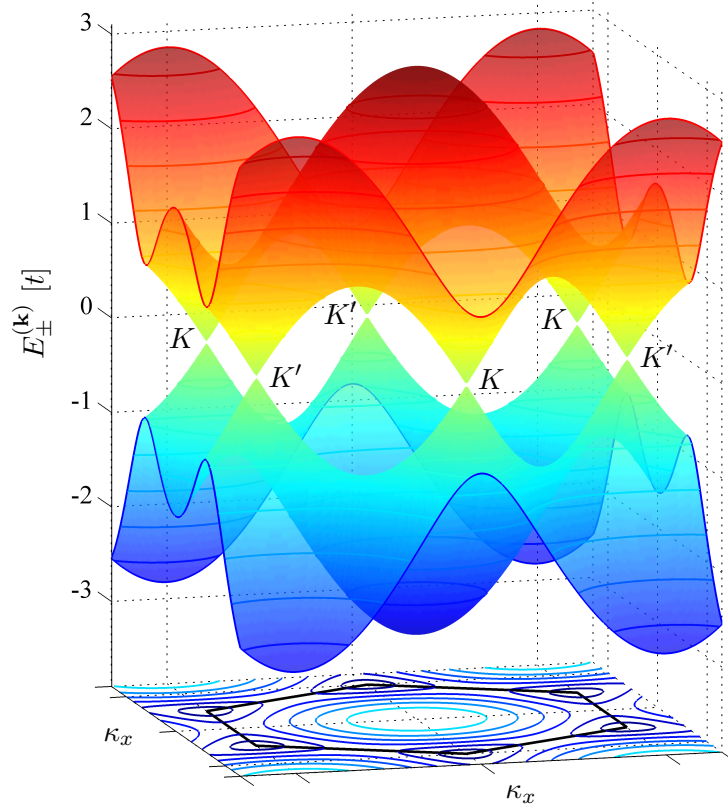


Figure 1.4: The band structure of graphene. The conduction band and the valence band are touching each other at the corner points of the first Brillouin zone marked as  $K$  and  $K'$ .

The left-hand side of the equation is zero if at least one of the factors is equal to zero. The exponential factor in front of the brackets is always different from zero, leaving as the only option the expression in the brackets

$$2 \cos\left(\frac{K_y a}{2}\right) + \exp\left(i \frac{K_x a \sqrt{3}}{2}\right) = 2 \cos\left(\frac{K_y a}{2}\right) + \cos\left(\frac{K_x a \sqrt{3}}{2}\right) + i \sin\left(\frac{K_x a \sqrt{3}}{2}\right) = 0. \quad (1.33)$$

The values of  $K_x$  and  $K_y$  are obtained by demanding both the real and imaginary parts on the left-hand side of Equation (1.33) to be equal to zero

$$\sin\left(\frac{K_x a \sqrt{3}}{2}\right) = 0 \quad \Rightarrow \quad K_x = \frac{2n\pi}{a\sqrt{3}}, \quad n \in \mathcal{Z}, \quad (1.34)$$

$$2 \cos\left(\frac{K_y a}{2}\right) = \pm 1 \quad \Rightarrow \quad K_y = \begin{cases} \pm \frac{4\pi}{3a} + 2m\pi, & n \text{ even,} \\ \pm \frac{2\pi}{3a} + 2m\pi, & n \text{ odd} \end{cases}. \quad (1.35)$$

The above equations describe two superimposed nets of inequivalent points marked  $K$  and  $K'$  as depicted in Fig. 1.1. The remark inequivalent comes from the fact that there is no lattice transformation by which one net could be obtained from the other. The shape of the first Brillouin zone might suggest that it contains six inequivalent corner points, but one has to remember that any two points which can be connected by a reciprocal lattice vector are equivalent and correspond to one and the

same electronic state, leaving us with only two inequivalent points  $K$  and  $K'$  described by the vectors  $\mathbf{K} = (0, \frac{4\pi}{3a})$  and  $\mathbf{K}' = (0, -\frac{4\pi}{3a})$ .

Having those two position vectors, one can proceed with the approximation of the energy dispersion curves given by Equation (1.31) in the vicinity of  $K$  and  $K'$  using the Taylor's expansion. Rather than to work directly with the expression for energy, it is more convenient to apply the Taylor's expansion on the factor  $f^{(\mathbf{k})}$  given by Equation (1.26)

$$f^{(\mathbf{k}+\boldsymbol{\kappa})} = f^{(\mathbf{K})} + \mathbf{q} \cdot \nabla_{\mathbf{k}} f^{(\mathbf{k})} \Big|_{\mathbf{k}=\mathbf{K}} = i \frac{\sqrt{3}a}{2} (\kappa_x + i\kappa_y), \quad (1.36)$$

$$f^{(\mathbf{K}'+\boldsymbol{\kappa})} = f^{(\mathbf{K}')} + \boldsymbol{\kappa} \cdot \nabla_{\mathbf{k}} f^{(\mathbf{k})} \Big|_{\mathbf{k}=\mathbf{K}'} = i \frac{\sqrt{3}a}{2} (\kappa_x - i\kappa_y), \quad (1.37)$$

where  $\boldsymbol{\kappa} = \mathbf{k} - \mathbf{K}$ , resp.  $\boldsymbol{\kappa} = \mathbf{k} - \mathbf{K}'$ . The energy dispersion near the band extrema is now easily obtained through Equation (1.30)

$$E_{\pm}(\boldsymbol{\kappa}) = E_{\pm}^{(\mathbf{K}+\boldsymbol{\kappa})} = E_{\pm}^{(\mathbf{K}'+\boldsymbol{\kappa})} = \pm \frac{\sqrt{3}}{2} at |\boldsymbol{\kappa}|. \quad (1.38)$$

The above equation corresponds to a band structure in the shape of two cones touching at their apexes as depicted in Fig. 1.5. The linear energy dispersion has intriguing consequences for the physics of the electrons. By comparing the outcome of Equation (1.38) with the energy-momentum dependence  $E = \sqrt{m_0^2 c^4 + \hbar^2 |\mathbf{k}|^2 c^2}$  of a relativistic particle

$$E_{\pm}(\boldsymbol{\kappa}) = \pm \frac{\sqrt{3}}{2} at |\boldsymbol{\kappa}| = \pm \hbar v_F |\boldsymbol{\kappa}| = \pm \sqrt{m_0^2 v_F^4 + \hbar^2 |\boldsymbol{\kappa}|^2 v_F^2} \Big|_{m_0=0}, \quad (1.39)$$

one can see that the electrons in graphene can be described as relativistic massless charged particles moving with speed  $v_F = \frac{\sqrt{3}at}{2\hbar} \approx 10^6 \text{ m} \cdot \text{s}^{-1}$ , which has no analogy in the realm of ordinary elementary particles. Furthermore, the proper description of their behaviour requires a treatment within the relativistic Dirac equation, which might be also the reason, why are the two cones in the bandstructure often called the Dirac cones and the point at their apexes the Dirac point.

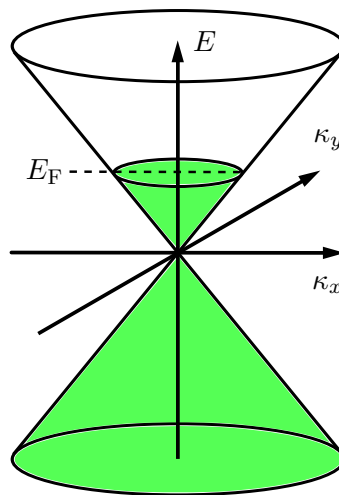


Figure 1.5: The band structure of graphene near the Dirac points. The energy dispersion of electrons is linear and reminds of the dispersion for massless relativistic particles. Furthermore, the Fermi energy is shifted from its default position at the Dirac point, giving graphene a metallic character.

## 1.5. ELECTRON WAVEFUNCTIONS AT THE DIRAC POINTS

As already mentioned, the Fermi energy of graphene in its natural state lies just at the Dirac point, but a contact with other materials with a different work function, doping or application of an external voltage can slightly shift the Fermi level both to the lower and higher energies, having a dramatic effect on the electric and optical properties. The peculiar behaviour of the electrons in graphene in the vicinity of the Dirac points is further emphasized by the Klein tunneling, which is basically the absence of the scattering from impurities, making graphene a very good conductor even for modest values of the free charge carrier density.

The density of free charge carriers  $n$  can be calculated from the Fermi energy  $E_F$  and vice versa using the well known quantity, the density of states  $\mathcal{D}(\mathcal{E})$ , which is defined as the number of electronic states per a unit area within a small energy interval  $dE$ . Let us first calculate the number of states enclosed by a circle of radius  $\kappa$  and centered at the Dirac point, which is given by the area of the circle divided by the area of the region in the reciprocal space assigned to one state

$$N(\kappa) = \frac{\pi \kappa^2}{\frac{(2\pi)^2}{\Omega}}, \quad (1.40)$$

where  $\Omega$  is the total area of the graphene surface. The density of states is then obtained as the derivative with respect to the energy  $E$  divided by  $\Omega$

$$\mathcal{D}(E) = \frac{1}{A} \frac{dN(\kappa)}{d\kappa} \frac{d\kappa}{dE} = \frac{g_s g_v |E|}{2\pi \hbar^2 v_F^2}, \quad (1.41)$$

where  $g_s = 2$  and  $g_v = 2$  account for the spin and valley degeneracies, since one electronic state can accommodate two electrons with opposite spins and there are two pairs of the Dirac cones within the first Brillouin zone (at  $K$  and  $K'$ ). The density of free charge carriers  $n$  is now obtained by integration of the density of states over the occupied, resp. unoccupied electronic states of the conduction, resp. valence band

$$n(E_F) = \int_0^{E_F} dE \mathcal{D}(E) = \frac{g_s g_v E_F^2}{4\pi \hbar^2 v_F^2}. \quad (1.42)$$

The above equation suggests that graphene becomes a perfect zero bandgap semiconductor, when the Fermi level is set exactly at the Dirac point. Interestingly, thorough calculations show that the peculiar nature of electrons near the Dirac points results in a non-zero DC conductivity even for  $E_F = 0$ , thus the previous designation is slightly incorrect and graphene should be referred to as a metal.

## 1.5. Electron wavefunctions at the Dirac points

In order to find the expressions for the electron wavefunctions near the Dirac points, one has to return to the matrix equation  $(\mathcal{H}(\mathbf{k}) - E_i^{(\mathbf{k})} \mathcal{S}(\mathbf{k})) \mathcal{C}_i^{(\mathbf{k})} = 0$  (Eq. (1.12)) for the coefficients  $a_i(\mathbf{k})$  and  $b_i(\mathbf{k})$  (Eq. (1.14)), which can be rewritten using the following notation

$$\begin{pmatrix} -E_\alpha^{(\mathbf{k})} & t f^{(\mathbf{k})} \\ t f^{*(\mathbf{k})} & -E_\alpha^{(\mathbf{k})} \end{pmatrix} \begin{pmatrix} a_\alpha(\mathbf{k}) \\ b_\alpha(\mathbf{k}) \end{pmatrix} = \begin{pmatrix} -\alpha t |f^{(\mathbf{k})}| & t f^{(\mathbf{k})} \\ t f^{*(\mathbf{k})} & -\alpha t |f^{(\mathbf{k})}| \end{pmatrix} \begin{pmatrix} a_\alpha(\mathbf{k}) \\ b_\alpha(\mathbf{k}) \end{pmatrix} = 0, \quad (1.43)$$

where  $\alpha = \pm$  denotes the upper, resp. lower band. These two equations are not independent and therefore allow only to express  $b_\alpha(\mathbf{k})$  in terms of  $a_\alpha(\mathbf{k})$

$$b_\alpha(\mathbf{k}) = \alpha \frac{a_\alpha(\mathbf{k}) f^{*(\mathbf{k})}}{|f^{(\mathbf{k})}|}. \quad (1.44)$$

Another equation can be acquired from the requirement that the wavefunction  $\psi_\alpha^{(\mathbf{k})}(\mathbf{r}) = a_\alpha(\mathbf{k})\Phi_A^{(\mathbf{k})}(\mathbf{r}) + b_\alpha(\mathbf{k})\Phi_B^{(\mathbf{k})}(\mathbf{r})$  should be normalized to one

$$\begin{aligned} \langle \psi_\alpha^{(\mathbf{k})}(\mathbf{r}) | \psi_\alpha^{(\mathbf{k})}(\mathbf{r}) \rangle &= |a_\alpha(\mathbf{k})|^2 S_{AA}^{(\mathbf{k})} + |b_\alpha(\mathbf{k})|^2 S_{BB}^{(\mathbf{k})} + a_\alpha^*(\mathbf{k}) b_\alpha(\mathbf{k}) S_{AB}^{(\mathbf{k})} + a_\alpha(\mathbf{k}) b_\alpha^*(\mathbf{k}) S_{BA}^{(\mathbf{k})} = \\ &= |a_\alpha(\mathbf{k})|^2 + |b_\alpha(\mathbf{k})|^2 = 1. \end{aligned} \quad (1.45)$$

Finally, by combining Equations (1.44) and (1.45), the expressions for the coefficients  $a_\alpha(\mathbf{k})$  and  $b_\alpha(\mathbf{k})$  are procured

$$a_\alpha(\mathbf{k}) = \frac{1}{\sqrt{2}}, \quad b_\alpha(\mathbf{k}) = \frac{1}{\sqrt{2}} \alpha \frac{f^{*(\mathbf{k})}}{|f(\mathbf{k})|}, \quad (1.46)$$

and the wavefunction  $\psi_\alpha^{(\mathbf{k})}(\mathbf{r})$  becomes

$$\psi_\alpha^{(\mathbf{k})}(\mathbf{r}) = \frac{1}{\sqrt{2}} \Phi_A^{(\mathbf{k})}(\mathbf{r}) + \frac{1}{\sqrt{2}} \alpha \frac{f^{*(\mathbf{k})}}{|f(\mathbf{k})|} \Phi_B^{(\mathbf{k})}(\mathbf{r}). \quad (1.47)$$

The above expression for the wavefunction is still rather complicated and calculations with it would become too involved. It turns out that using the so called  $\mathbf{k} \cdot \mathbf{p}$  method, one can expand the wavefunction around the Dirac points in a similar manner as in the case of the energy dispersion. Here we will not pursue the whole derivation, but we shall satisfy with its result. Detailed calculations can be found in [23]. After the application of the  $\mathbf{k} \cdot \mathbf{p}$  method, the wavefunction in the vicinity of the two Dirac points can be expressed as

$$\psi_\alpha^{(\mathbf{K}+\boldsymbol{\kappa})}(\mathbf{r}) = e^{i\boldsymbol{\kappa} \cdot \mathbf{r}} \left[ \frac{1}{\sqrt{2}} \Phi_A^{(\mathbf{K})}(\mathbf{r}) + \frac{1}{\sqrt{2}} \alpha \frac{f^{*(\mathbf{K}+\boldsymbol{\kappa})}}{|f(\mathbf{K}+\boldsymbol{\kappa})|} \Phi_B^{(\mathbf{K})}(\mathbf{r}) \right], \quad (1.48)$$

$$\psi_\alpha^{(\mathbf{K}'+\boldsymbol{\kappa})}(\mathbf{r}) = e^{i\boldsymbol{\kappa} \cdot \mathbf{r}} \left[ \frac{1}{\sqrt{2}} \Phi_A^{(\mathbf{K}')}(\mathbf{r}) + \frac{1}{\sqrt{2}} \alpha \frac{f^{*(\mathbf{K}'+\boldsymbol{\kappa})}}{|f(\mathbf{K}'+\boldsymbol{\kappa})|} \Phi_B^{(\mathbf{K}')}(\mathbf{r}) \right], \quad (1.49)$$

where the wavevector  $\boldsymbol{\kappa}$  is measured from the respective Dirac point. Replacing the factors  $f^{(\mathbf{K}+\boldsymbol{\kappa})}$  and  $f^{(\mathbf{K}'+\boldsymbol{\kappa})}$  with their approximated forms given by Equations (1.36) and (1.37), the above equations become

$$\psi_\alpha^{(\mathbf{K}+\boldsymbol{\kappa})}(\mathbf{r}) = e^{i\boldsymbol{\kappa} \cdot \mathbf{r}} \left[ \alpha_{F_A}^{(\mathbf{K})}(\boldsymbol{\kappa}) \Phi_A^{(\mathbf{K})}(\mathbf{r}) + \alpha_{F_B}^{(\mathbf{K})}(\boldsymbol{\kappa}) \Phi_B^{(\mathbf{K})}(\mathbf{r}) \right], \quad (1.50)$$

$$\psi_\alpha^{(\mathbf{K}'+\boldsymbol{\kappa})}(\mathbf{r}) = e^{i\boldsymbol{\kappa} \cdot \mathbf{r}} \left[ \alpha_{F_A}^{(\mathbf{K}')}(\boldsymbol{\kappa}) \Phi_A^{(\mathbf{K}')}(\mathbf{r}) + \alpha_{F_B}^{(\mathbf{K}')}(\boldsymbol{\kappa}) \Phi_B^{(\mathbf{K}')}(\mathbf{r}) \right], \quad (1.51)$$

where for lucidity the following coefficients have been introduced

$$\alpha_{F_A}^{(\mathbf{K})}(\boldsymbol{\kappa}) = \frac{1}{\sqrt{2}}, \quad \alpha_{F_B}^{(\mathbf{K})}(\boldsymbol{\kappa}) = \frac{1}{\sqrt{2}} \alpha \frac{\kappa_x - i\kappa_y}{\sqrt{\kappa_x^2 + \kappa_y^2}}, \quad \alpha_{F_A}^{(\mathbf{K}')}(\boldsymbol{\kappa}) = \frac{1}{\sqrt{2}}, \quad \alpha_{F_B}^{(\mathbf{K}')}(\boldsymbol{\kappa}) = \frac{1}{\sqrt{2}} \alpha \frac{\kappa_x + i\kappa_y}{\sqrt{\kappa_x^2 + \kappa_y^2}}.$$

Equations (1.50) and (1.51) represent approximated expressions for the electron wavefunctions in the neighbourhood of the Dirac points  $K$  and  $K'$ , suitable for further calculations. The above derivation relies on the work of Ando [2, 3], who extensively contributed to the present knowledge of graphene's electronic and optical properties.

## 1.6. Self consistent field method

In order to capture all the aspects of the electro-dynamical response of graphene including interband transitions, non-local effects and temperature dependence, one has to treat it fully within the framework of quantum statistical mechanics and quantum electrodynamics, making it a non-trivial issue. An approximate solution to this problem of mutually interacting electrons moving in a periodic crystal potential and exposed to a time-varying external electromagnetic field is provided by the self consistent field method [11].

It relies on the assumption that the interaction between electrons can be expressed in terms of a self-consistent potential  $V(\mathbf{r}, t)$ , or more precisely its induced part. One can look at this as though the fluctuations in the electron density produced by the external field give rise to an induced field, which then acts back on the electrons, making corrections to the electron density and so on. Adopting this assumption, one can write the one-particle Hamiltonian  $\hat{H}$  in the form

$$\hat{H} = \hat{H}_0 + \hat{V}(\mathbf{r}, t), \quad (1.52)$$

where  $\hat{H}_0$  is the unperturbed crystal Hamiltonian and  $\hat{V}(\mathbf{r}, t) = \hat{V}_{\text{ind}}(\mathbf{r}, t) + \hat{V}_{\text{ext}}(\mathbf{r}, t)$  corresponds to the aforementioned induced and external potentials (in this context the potential has to be interpreted as the potential energy). For clarity, the hat above a quantity indicates that it is an operator.

Since we are dealing with a system, which is presumably in a thermal equilibrium with its surroundings, repeated measurements on this system (assuming an identical initial preparation) will not generally give, due to chaotic processes, identical results (the same distribution of the possible outcomes). One must, therefore, treat the system on the footings of quantum statistical mechanics using the concept of a one-particle density matrix [13].

First let us assume an ensemble of  $Z$  identical systems (a construction equivalent to  $Z$  repeated measurements on one system), which, in this particular case, consists of an electron moving in a periodic crystal potential. Furthermore, each system is found to be in a thermal equilibrium with a reservoir, in this case the surrounding electron sea, and each system is described by a wavefunction  $|\psi^{(\alpha)}\rangle$ , which in terms of the eigenstates  $|\varphi_k\rangle$  of some operator  $\hat{A}$  reads

$$|\psi^{(\alpha)}\rangle = \sum_k C_k^{(\alpha)} |\varphi_k\rangle, \quad (1.53)$$

where the index  $\alpha = 1, 2, \dots, Z$  distinguishes the different systems of the ensemble. Using the representation given by the above equation, the expectation value of another operator  $\hat{B}$  is calculated as the statistical average over the expectation values obtained separately within each system of the ensemble.

$$\begin{aligned} \langle \hat{B} \rangle_{\text{ensemble}} &= \frac{1}{Z} \sum_{\alpha=1}^Z \langle \psi^{(\alpha)} | \hat{B} | \psi^{(\alpha)} \rangle = \frac{1}{Z} \sum_{\alpha=1}^Z \langle \sum_k C_k^{(\alpha)} \varphi_k | \hat{B} | \sum_l C_l^{(\alpha)} \varphi_l \rangle = \\ &= \sum_{k,l} \left( \frac{1}{Z} \sum_{\alpha=1}^Z C_l^{(\alpha)} C_k^{*(\alpha)} \right) \langle \varphi_k | \hat{B} | \varphi_l \rangle = \sum_{k,l} \rho_{lk} B_{kl}, \end{aligned} \quad (1.54)$$

where  $\rho_{lk} = \frac{1}{Z} \sum_{\alpha=1}^Z C_l^{(\alpha)} C_k^{*(\alpha)}$  determines the statistical probability that the outcome of the measurement will be  $B_{kl} = \langle \varphi_k | \hat{B} | \varphi_l \rangle$ . The elements  $\rho_{lk}$  form together the so called density matrix, which fully captures the chaotic aspects of the system's behaviour and enables to calculate the expectation value of an arbitrary quantity.

More importantly, considering the presented problem of mutually interacting electrons, the diagonal elements of the density matrix  $\rho_{kk}$  determine the statistical probability of finding an electron in the

eigenstate  $|\varphi_k\rangle$ , thus the density matrix itself can be directly related to the Fermi-Dirac distribution of electrons (assuming a time-independent Hamiltonian).

Later it will prove itself useful to be able to express the density matrix in the form of an operator, which can be done by expanding the matrix element  $\rho_{lk}$  in terms of the eigenstates  $|\varphi_k\rangle$

$$\begin{aligned} \rho_{lk} &= \frac{1}{Z} \sum_{\alpha=1}^Z C_l^{(\alpha)} C_k^{*(\alpha)} = \frac{1}{Z} \sum_{\alpha=1}^Z \left( \sum_i C_i^{(\alpha)} \langle \varphi_l | \varphi_i \rangle \sum_j C_j^{*(\alpha)} \langle \varphi_j | \varphi_k \rangle \right) = \\ &= \langle \varphi_l | \left[ \frac{1}{Z} \sum_{\alpha=1}^Z \left( \sum_i C_i^{(\alpha)} |\varphi_i\rangle \sum_j C_j^{*(\alpha)} \langle \varphi_j| \right) \right] | \varphi_k \rangle = \langle \varphi_l | \left( \frac{1}{Z} \sum_{\alpha=1}^Z |\psi^{(\alpha)}\rangle \langle \psi^{(\alpha)}| \right) | \varphi_k \rangle = \\ &= \langle \varphi_l | \hat{\rho} | \varphi_k \rangle. \end{aligned} \quad (1.55)$$

Since the derivation of the final expression for the dynamical conductivity of graphene is lengthy and not entirely straightforward, it might be reasonable to briefly outline the course of the derivation so that the reader does not get lost. The first step is to express the induced fluctuations of the density operator  $\hat{\rho}$  due to an external field in terms of the self-consistent potential and electron wavefunctions derived in the previous section. This extensive part relies on the first order time-dependent self-consistent perturbation theory. The density operator can be subsequently employed to calculate the induced electron density  $n_{2D}$  using the formalism presented above. Then comes the task of relating the induced electron density to the non-local dynamical susceptibility  $\chi_{2D}(\mathbf{q}, \omega)$ . Taking the local limit of this quantity, one can finally obtain the expression for the frequency-dependent dynamical conductivity  $\sigma(\omega)$ .

The presence of a time-varying external electromagnetic field distorts the equilibrium distribution of the electrons given by the Fermi-Dirac statistics. The new distribution can be fully described by the time-dependent density operator  $\hat{\rho}$  (Eq. (1.55)), which is tied to the external perturbation through the quantum-mechanical Liouville equation (also known as the von Neumann equation)

$$i\hbar \frac{\partial \hat{\rho}}{\partial t} = [\hat{H}, \hat{\rho}], \quad (1.56)$$

where  $\hat{H}$  is the one-particle Hamiltonian from Equation (1.52) and  $[\hat{H}, \hat{\rho}] = \hat{H}\hat{\rho} - \hat{\rho}\hat{H}$  is the commutator of the Hamiltonian and the density operator. The above equation can be easily derived from the time-dependent Schrödinger equation (see Appendix A).

According to Equation (1.55), the matrix elements of the operator  $\frac{\partial \hat{\rho}}{\partial t}$  are obtained by wrapping it with the respective eigenstates

$$i\hbar \langle \varphi_l | \frac{\partial \hat{\rho}}{\partial t} | \varphi_k \rangle = \langle \varphi_l | [\hat{H}, \hat{\rho}] | \varphi_k \rangle, \quad (1.57)$$

Furthermore, by recognizing the eigenstates  $|\varphi_k\rangle$  and  $|\varphi_l\rangle$  as the electron wavefunctions given by Equations (1.50) and (1.51), we arrive at the quantum-mechanical Liouville equation for graphene, the starting point for further calculations. Introducing the following notation

$$|\varphi_k\rangle = \psi_{\alpha}^{(\mathbf{k})}(\mathbf{r}) = e^{i(\mathbf{k}-\mathbf{\Lambda})\cdot\mathbf{r}} \left[ \alpha F_A^{(\mathbf{\Lambda})}(\mathbf{k}) \Phi_A^{(\mathbf{\Lambda})}(\mathbf{r}) + \alpha F_B^{(\mathbf{\Lambda})}(\mathbf{k}) \Phi_B^{(\mathbf{\Lambda})}(\mathbf{r}) \right] = |\alpha \mathbf{k}\rangle, \quad (1.58)$$

$$|\varphi_l\rangle = \psi_{\beta}^{(\mathbf{k}+\mathbf{q})}(\mathbf{r}) = e^{i(\mathbf{k}+\mathbf{q}-\mathbf{\Lambda})\cdot\mathbf{r}} \left[ \beta F_A^{(\mathbf{\Lambda})}(\mathbf{k}+\mathbf{q}) \Phi_A^{(\mathbf{\Lambda})}(\mathbf{r}) + \beta F_B^{(\mathbf{\Lambda})}(\mathbf{k}+\mathbf{q}) \Phi_B^{(\mathbf{\Lambda})}(\mathbf{r}) \right] = |\beta \mathbf{k}+\mathbf{q}\rangle, \quad (1.59)$$

where  $\alpha = \pm$  and  $\beta = \pm$  indicate, whether are the respective states  $|\alpha \mathbf{k}\rangle$  and  $|\beta \mathbf{k}+\mathbf{q}\rangle$  situated in the valence or the conduction band of graphene, the symbol  $\mathbf{\Lambda} = \mathbf{K}, \mathbf{K}'$  marks the two inequivalent Dirac

## 1.6. SELF CONSISTENT FIELD METHOD

points and the wavevector  $\mathbf{q}$  corresponds to the momentum mismatch between those two states, the Liouville equation for graphene becomes

$$i\hbar\langle\beta\mathbf{k}+\mathbf{q}|\frac{\partial\hat{\rho}}{\partial t}|\alpha\mathbf{k}\rangle=\langle\beta\mathbf{k}+\mathbf{q}|[\hat{H},\hat{\rho}]|\alpha\mathbf{k}\rangle, \quad (1.60)$$

In the spirit of the first order time-dependent perturbation theory, one can expand the density operator into an unperturbed component  $\hat{\rho}^{(0)}$  and a correction part  $\hat{\rho}^{(1)}$  accounting for the perturbation term  $\hat{V}(\mathbf{r}, t)$  in the one-particle Hamiltonian (Eq. (1.52))

$$\hat{\rho}=\hat{\rho}^{(0)}+\hat{\rho}^{(1)}. \quad (1.61)$$

Adopting the above expansion and expressing the Hamiltonian by means of the unperturbed crystal Hamiltonian  $\hat{H}_0$  and the self-consistent potential  $\hat{V}(\mathbf{r}, t)$  (Eq. (1.52)), the Liouville equation acquires the form

$$i\hbar\langle\beta\mathbf{k}+\mathbf{q}|\frac{\partial\hat{\rho}^{(0)}}{\partial t}+\frac{\partial\hat{\rho}^{(1)}}{\partial t}|\alpha\mathbf{k}\rangle=\langle\beta\mathbf{k}+\mathbf{q}|[\hat{H}_0+\hat{V}(\mathbf{r}, t),\hat{\rho}^{(0)}+\hat{\rho}^{(1)}]|\alpha\mathbf{k}\rangle. \quad (1.62)$$

As pointed out earlier, the equilibrium energy distribution of electrons prescribed by the unperturbed part of the density operator  $\hat{\rho}^{(0)}$  should be the same as that given by the Fermi-Dirac statistics. Furthermore, considering the unperturbed crystal Hamiltonian  $\hat{H}_0$ , the energy assigned to an electron in the eigenstate  $|\alpha\mathbf{k}\rangle$  should correspond to the energy of an electron in unperturbed graphene, that is one should recover the energy dispersion of graphene derived in Section (1.4). Put into language of the quantum-mechanical formalism

$$\hat{\rho}^{(0)}|\alpha\mathbf{k}\rangle=f_0(E_\alpha^{\mathbf{k}-\Lambda})|\alpha\mathbf{k}\rangle=f_0^{\alpha\mathbf{k}}|\alpha\mathbf{k}\rangle, \quad (1.63)$$

$$\hat{H}_0|\alpha\mathbf{k}\rangle=E_\alpha^{\mathbf{k}-\Lambda}|\alpha\mathbf{k}\rangle=E_0^{\alpha\mathbf{k}}|\alpha\mathbf{k}\rangle, \quad (1.64)$$

where  $f_0^{\alpha\mathbf{k}}=f_0(E_\alpha^{\mathbf{k}-\Lambda})$  stands for the Fermi-Dirac distribution function and  $E_0^{\alpha\mathbf{k}}=E_\alpha^{\mathbf{k}-\Lambda}$  is the energy assigned to the eigenstate  $|\alpha\mathbf{k}\rangle$  in unperturbed graphene (Eq. (1.31)). Moreover, the unperturbed part of the density operator  $\hat{\rho}^{(0)}$  characterizing the equilibrium state of the system should not depend on time, leaving on the left-hand side (LHS) of Equation (1.62) only the term

$$\text{LHS}=i\hbar\langle\beta\mathbf{k}+\mathbf{q}|\frac{\partial\hat{\rho}^{(1)}}{\partial t}|\alpha\mathbf{k}\rangle. \quad (1.65)$$

Utilizing the assumptions about the eigenvalues of the operators  $\hat{\rho}^{(0)}$  and  $\hat{H}_0$  given by Equations (1.63) and (1.64) and decomposing the commutator into separated terms, one can rewrite the right-hand side (RHS) of Equation (1.62) as

$$\begin{aligned} \text{RHS} &= \langle\beta\mathbf{k}+\mathbf{q}|(\hat{H}_0+\hat{V})(\hat{\rho}^{(0)}+\hat{\rho}^{(1)})-(\hat{\rho}^{(0)}+\hat{\rho}^{(1)})(\hat{H}_0+\hat{V})|\alpha\mathbf{k}\rangle= \\ &= \langle\beta\mathbf{k}+\mathbf{q}|\hat{H}_0\hat{\rho}^{(0)}-\hat{\rho}^{(0)}\hat{H}_0+\hat{H}_0\hat{\rho}^{(1)}-\hat{\rho}^{(1)}\hat{H}_0+\hat{V}\hat{\rho}^{(0)}-\hat{\rho}^{(0)}\hat{V}+\hat{V}\hat{\rho}^{(1)}-\hat{\rho}^{(1)}\hat{V}|\alpha\mathbf{k}\rangle= \\ &= (f_0^{\alpha\mathbf{k}}E_0^{\alpha\mathbf{k}}-E_0^{\alpha\mathbf{k}}f_0^{\alpha\mathbf{k}})\langle\beta\mathbf{k}+\mathbf{q}|\alpha\mathbf{k}\rangle+(E_0^{\beta\mathbf{k}+\mathbf{q}}-E_0^{\alpha\mathbf{k}})\langle\beta\mathbf{k}+\mathbf{q}|\hat{\rho}^{(1)}|\alpha\mathbf{k}\rangle+ \\ &+ (f_0^{\alpha\mathbf{k}}-f_0^{\beta\mathbf{k}+\mathbf{q}})\langle\beta\mathbf{k}+\mathbf{q}|\hat{V}(\mathbf{r}, t)|\alpha\mathbf{k}\rangle+\langle\beta\mathbf{k}+\mathbf{q}|\hat{V}(\mathbf{r}, t),\hat{\rho}^{(1)}|\alpha\mathbf{k}\rangle, \end{aligned} \quad (1.66)$$

where the property of the Hermiticity of the operators  $\hat{\rho}^{(0)}=\hat{\rho}^{(0)\dagger}$  and  $\hat{H}_0=\hat{H}_0^\dagger$  has been exploited in the following way

$$\begin{aligned} \langle \beta \mathbf{k} + \mathbf{q} | \hat{H}_0 \hat{\rho}^{(1)} | \alpha \mathbf{k} \rangle &= \langle \hat{H}_0^\dagger (\beta \mathbf{k} + \mathbf{q}) | \hat{\rho}^{(1)} | \alpha \mathbf{k} \rangle = \langle \hat{H}_0 (\beta \mathbf{k} + \mathbf{q}) | \hat{\rho}^{(1)} | \alpha \mathbf{k} \rangle = \\ &= E_0^{\alpha \mathbf{k}} \langle \beta \mathbf{k} + \mathbf{q} | \hat{\rho}^{(1)} | \alpha \mathbf{k} \rangle \end{aligned} \quad (1.67)$$

$$\begin{aligned} \langle \beta \mathbf{k} + \mathbf{q} | \hat{\rho}^{(0)} \hat{V} | \alpha \mathbf{k} \rangle &= \langle \hat{\rho}^{(0)\dagger} (\beta \mathbf{k} + \mathbf{q}) | \hat{V} | \alpha \mathbf{k} \rangle = \langle \hat{\rho}^{(0)} (\beta \mathbf{k} + \mathbf{q}) | \hat{V} | \alpha \mathbf{k} \rangle = \\ &= f_0^{\alpha \mathbf{k}} \langle \beta \mathbf{k} + \mathbf{q} | \hat{V} | \alpha \mathbf{k} \rangle. \end{aligned} \quad (1.68)$$

Putting the left-hand (LHS) and right-hand side (RHS) of Equation (1.62) back together and retaining only the terms up to the first order in the perturbation (assuming the perturbation is small), an equation containing only three yet unknown factors is acquired (one of them being the sought density matrix element  $\langle \beta \mathbf{k} + \mathbf{q} | \hat{\rho}^{(1)} | \alpha \mathbf{k} \rangle$ )

$$i\hbar \langle \beta \mathbf{k} + \mathbf{q} | \frac{\partial \hat{\rho}^{(1)}}{\partial t} | \alpha \mathbf{k} \rangle = \left( E_0^{\beta \mathbf{k} + \mathbf{q}} - E_0^{\alpha \mathbf{k}} \right) \langle \beta \mathbf{k} + \mathbf{q} | \hat{\rho}^{(1)} | \alpha \mathbf{k} \rangle + \left( f_0^{\alpha \mathbf{k}} - f_0^{\beta \mathbf{k} + \mathbf{q}} \right) \langle \beta \mathbf{k} + \mathbf{q} | \hat{V}(\mathbf{r}, t) | \alpha \mathbf{k} \rangle. \quad (1.69)$$

The next step is the evaluation of the last term on the right-hand side  $\langle \beta \mathbf{k} + \mathbf{q} | \hat{V}(\mathbf{r}, t) | \alpha \mathbf{k} \rangle$  characterizing the transition rate between the states  $|\alpha \mathbf{k}\rangle$  and  $|\beta \mathbf{k} + \mathbf{q}\rangle$ . Let us start by writing it in the integral form using the representation of the electronic states given by Equations (1.58) and (1.59)

$$\begin{aligned} \langle \beta \mathbf{k} + \mathbf{q} | \hat{V}(\mathbf{r}, t) | \alpha \mathbf{k} \rangle &= \int_{\Omega} d^2 \mathbf{r} e^{-i(\mathbf{k} + \mathbf{q} - \Lambda) \cdot \mathbf{r}} e^{i(\mathbf{k} - \Lambda) \cdot \mathbf{r}} \left[ \beta F_A^{(\Lambda)*}(\mathbf{k} + \mathbf{q}) \alpha F_A^{(\Lambda)}(\mathbf{k}) \left| \Phi_A^{(\Lambda)}(\mathbf{r}) \right|^2 + \right. \\ &+ \beta F_A^{(\Lambda)*}(\mathbf{k} + \mathbf{q}) \alpha F_B^{(\Lambda)}(\mathbf{k}) \Phi_A^{(\Lambda)*}(\mathbf{r}) \Phi_B^{(\Lambda)}(\mathbf{r}) + \beta F_B^{(\Lambda)*}(\mathbf{k} + \mathbf{q}) \alpha F_A^{(\Lambda)}(\mathbf{k}) \Phi_B^{(\Lambda)*}(\mathbf{r}) \Phi_A^{(\Lambda)}(\mathbf{r}) + \\ &\left. + \beta F_B^{(\Lambda)*}(\mathbf{k} + \mathbf{q}) \alpha F_B^{(\Lambda)}(\mathbf{k}) \left| \Phi_B^{(\Lambda)}(\mathbf{r}) \right|^2 \right] V(\mathbf{r}, t) = \int_{\Omega} d^2 \mathbf{r} e^{-i\mathbf{q} \cdot \mathbf{r}} \Gamma_{\mathbf{k}, \mathbf{q}}^{\alpha \beta}(\mathbf{r}) V(\mathbf{r}, t) \end{aligned} \quad (1.70)$$

where the function  $\Gamma_{\mathbf{k}, \mathbf{q}}^{\alpha \beta}(\mathbf{r})$  accounts for the microscopic distribution of the electron density with a higher probability of finding an electron at the atomic sites and a lower between them, just as follows from the tight binding model of graphene.

The above expression for  $\langle \beta \mathbf{k} + \mathbf{q} | \hat{V}(\mathbf{r}, t) | \alpha \mathbf{k} \rangle$  is still too complicated and difficult to work with. Provided that the self-consistent potential  $\hat{V}(\mathbf{r}, t)$  does not significantly vary within one unit cell of the graphene's crystal lattice, one can overlook the microscopic variations in the electron distribution and replace the function  $\Gamma_{\mathbf{k}, \mathbf{q}}^{\alpha \beta}(\mathbf{r})$  by its average over the unit cell. This approximation should be justified for the external perturbation in the form of an electromagnetic wave with a wavelength many times larger than the dimensions of the unit cell.

$$\begin{aligned} \Gamma_{\mathbf{k}, \mathbf{q}}^{\alpha \beta} &= \frac{1}{\Omega_0} \int_{\Omega_0} d^2 \mathbf{r} \left[ \beta F_A^{(\Lambda)*}(\mathbf{k} + \mathbf{q}) \alpha F_A^{(\Lambda)}(\mathbf{k}) \left| \Phi_A^{(\Lambda)}(\mathbf{r}) \right|^2 + \beta F_A^{(\Lambda)*}(\mathbf{k} + \mathbf{q}) \alpha F_B^{(\Lambda)}(\mathbf{k}) \Phi_A^{(\Lambda)*}(\mathbf{r}) \Phi_B^{(\Lambda)}(\mathbf{r}) + \right. \\ &+ \beta F_B^{(\Lambda)*}(\mathbf{k} + \mathbf{q}) \alpha F_A^{(\Lambda)}(\mathbf{k}) \Phi_B^{(\Lambda)*}(\mathbf{r}) \Phi_A^{(\Lambda)}(\mathbf{r}) + \beta F_B^{(\Lambda)*}(\mathbf{k} + \mathbf{q}) \alpha F_B^{(\Lambda)}(\mathbf{k}) \left| \Phi_B^{(\Lambda)}(\mathbf{r}) \right|^2 \left. \right] = \\ &= \frac{1}{N\Omega_0} \left[ \beta F_A^{(\Lambda)*}(\mathbf{k} + \mathbf{q}) \alpha F_A^{(\Lambda)}(\mathbf{k}) S_{AA}^{(\Lambda)} + \beta F_A^{(\Lambda)*}(\mathbf{k} + \mathbf{q}) \alpha F_B^{(\Lambda)}(\mathbf{k}) S_{AB}^{(\Lambda)} + \right. \\ &+ \beta F_B^{(\Lambda)*}(\mathbf{k} + \mathbf{q}) \alpha F_A^{(\Lambda)}(\mathbf{k}) S_{BA}^{(\Lambda)} + \beta F_B^{(\Lambda)*}(\mathbf{k} + \mathbf{q}) \alpha F_B^{(\Lambda)}(\mathbf{k}) S_{BB}^{(\Lambda)} \left. \right] = \\ &= \frac{1}{\Omega} \left[ \beta F_A^{(\Lambda)*}(\mathbf{k} + \mathbf{q}) \alpha F_A^{(\Lambda)}(\mathbf{k}) + \beta F_B^{(\Lambda)*}(\mathbf{k} + \mathbf{q}) \alpha F_B^{(\Lambda)}(\mathbf{k}) \right], \end{aligned} \quad (1.71)$$

## 1.6. SELF CONSISTENT FIELD METHOD

where  $\Omega_0$ , resp.  $\Omega = N\Omega_0$  is the area of the unit cell, resp. the area of the whole graphene sheet and where the normalization condition for the overlap integrals  $S_{AA}^{(\Lambda)} = S_{BB}^{(\Lambda)} = \int_{\Omega_0} d^2\mathbf{r} |\Phi_A|^2 = \int_{\Omega_0} d^2\mathbf{r} |\Phi_B|^2 = \frac{1}{N}$  has been used.

Employing the above approximation, the integral in Equation (1.70) can be readily evaluated by the means of the Fourier analysis

$$\langle \beta \mathbf{k} + \mathbf{q} | \hat{V}(\mathbf{r}, t) | \alpha \mathbf{k} \rangle = \Gamma_{\mathbf{k}, \mathbf{q}}^{\alpha\beta} \int_{\Omega} d^2\mathbf{r} e^{-i\mathbf{q}\cdot\mathbf{r}} V(\mathbf{r}, t) = \Gamma_{\mathbf{k}, \mathbf{q}}^{\alpha\beta} V(\mathbf{q}, t), \quad (1.72)$$

with the Fourier transform and the inverse Fourier transform defined in the following way

$$F(\mathbf{q}) = \int_{-\infty}^{\infty} d^n\mathbf{r} e^{-i\mathbf{q}\cdot\mathbf{r}} f(\mathbf{r}), \quad (1.73)$$

$$f(\mathbf{r}) = \frac{1}{(2\pi)^n} \int_{-\infty}^{\infty} d^n\mathbf{r} e^{i\mathbf{q}\cdot\mathbf{r}} F(\mathbf{q}). \quad (1.74)$$

Let us now focus on the expression on the left-hand side of Equation (1.69) containing the time derivative of the density operator. It is reasonable to assume that the time-dependence of the fluctuations in the electron density and the self-consistent potential should reflect the time-dependence of the external perturbation. By making an Ansatz that the perturbing force acting on the system evolves in time as  $e^{\gamma t} e^{-i\omega t}$ , where  $\omega$  is the angular frequency and  $\gamma \rightarrow 0$  corresponds to the adiabatic turning on of the perturbation, the left-hand side of Equation (1.69) becomes

$$i\hbar \langle \beta \mathbf{k} + \mathbf{q} | \frac{\partial \hat{\rho}^{(1)}}{\partial t} | \alpha \mathbf{k} \rangle = (\hbar\omega + i\hbar\gamma) \langle \beta \mathbf{k} + \mathbf{q} | \hat{\rho}^{(1)} | \alpha \mathbf{k} \rangle. \quad (1.75)$$

Applying the above assumption about the time-dependence of the potentials and density operators also on the right-hand side of that equation and employing the expression for  $\langle \beta \mathbf{k} + \mathbf{q} | \hat{V}(\mathbf{r}, t) | \alpha \mathbf{k} \rangle$  given by Equation (1.72), one finally obtains, after some elementary operations, an equation for the elements of the density matrix

$$\langle \beta \mathbf{k} + \mathbf{q} | \hat{\rho}^{(1)} | \alpha \mathbf{k} \rangle = \frac{f_0^{\alpha\mathbf{k}} - f_0^{\beta\mathbf{k}+\mathbf{q}}}{E_0^{\alpha\mathbf{k}} - E_0^{\beta\mathbf{k}+\mathbf{q}} + \hbar\omega + i\hbar\gamma} V(\mathbf{q}) \quad (1.76)$$

Notice that the argument  $t$  in the self-consistent potential has been dropped, leaving only the spatial dependence, since the whole equation has been divided by the common exponential factor  $e^{\gamma t} e^{-i\omega t}$  corresponding to the time-evolution of the system.

Having the equation relating the elements of the density matrix directly to the corresponding Fourier components of the self-consistent potential  $\hat{V}(\mathbf{q})$ , the last missing ingredient necessary for the derivation of the dynamical conductivity of graphene is the induced electron density  $n_{2D}$ . Invoking the formalism of the quantum statistical mechanics (Eq. (1.54)), it can be calculated as the expectation value of the electron density operator  $\hat{n}$  defined as  $\hat{n}(\mathbf{r}) = \delta^2(\mathbf{r} - \mathbf{r}')$ .

$$n_{2D}(\mathbf{r}, \omega) = \langle \hat{n} \rangle = \sum_{\mathbf{k}, \mathbf{q}, \alpha, \beta, \Lambda} \langle \beta \mathbf{k} + \mathbf{q} | \hat{\rho}^{(1)} | \alpha \mathbf{k} \rangle \langle \alpha \mathbf{k} | \hat{n} | \beta \mathbf{k} + \mathbf{q} \rangle. \quad (1.77)$$

The summation must be performed over all the possible pairs of eigenstates including the different bands and one should take into account also the contributions from both the Dirac points. Matrix elements  $\langle \alpha \mathbf{k} | \hat{n} | \beta \mathbf{k} + \mathbf{q} \rangle$  are acquired by a conversion into integral forms and their subsequent evaluation. Since the procedure is more or less the same as for  $\langle \beta \mathbf{k} + \mathbf{q} | \hat{V}(\mathbf{r}, t) | \alpha \mathbf{k} \rangle$  obtained earlier in Equation (1.72), the detailed derivation is omitted here and only its outline is provided.

$$\begin{aligned}
 n_{2D}(\mathbf{r}, \omega) &= \sum_{\mathbf{k}, \mathbf{q}, \alpha, \beta, \Lambda} \langle \beta \mathbf{k} + \mathbf{q} | \hat{\rho}^{(1)} | \alpha \mathbf{k} \rangle \int_{\Omega} d^2 \mathbf{r}' \delta^2(\mathbf{r} - \mathbf{r}') e^{i\mathbf{q} \cdot \mathbf{r}'} \Gamma_{\mathbf{k}, \mathbf{q}}^{\alpha\beta*}(\mathbf{r}') \approx \\
 &\approx \sum_{\mathbf{k}, \mathbf{q}, \alpha, \beta, \Lambda} \langle \beta \mathbf{k} + \mathbf{q} | \hat{\rho}^{(1)} | \alpha \mathbf{k} \rangle \Gamma_{\mathbf{k}, \mathbf{q}}^{\alpha\beta*} \int_{\Omega} d^2 \mathbf{r}' \delta^2(\mathbf{r} - \mathbf{r}') e^{i\mathbf{q} \cdot \mathbf{r}'} = \sum_{\mathbf{k}, \mathbf{q}, \alpha, \beta, \Lambda} e^{i\mathbf{q} \cdot \mathbf{r}} \Gamma_{\mathbf{k}, \mathbf{q}}^{\alpha\beta*} \langle \beta \mathbf{k} + \mathbf{q} | \hat{\rho}^{(1)} | \alpha \mathbf{k} \rangle,
 \end{aligned} \tag{1.78}$$

where  $\Gamma_{\mathbf{k}, \mathbf{q}}^{\alpha\beta*}$  stands for the complex conjugate of  $\Gamma_{\mathbf{k}, \mathbf{q}}^{\alpha\beta}$  given in Equation (1.71).

The above expression for the induced electron density can be already used for a direct derivation of the dynamical susceptibility  $\chi_{2D}$ , but it will prove to be more convenient to work in the domain of spatial frequencies rather than in the direct space. The conversion into the Fourier domain is straightforward, since the above expression, apart from a yet unknown prefactor, already has the sought form. Replacing the discrete summation with a continuous integration (with emphasis on the proper normalization), Equation (1.78) becomes

$$n_{2D}(\mathbf{r}, \omega) = \int_{-\infty}^{\infty} d^2 \mathbf{q} e^{i\mathbf{q} \cdot \mathbf{r}} \frac{\Omega}{(2\pi)^2} \sum_{\mathbf{k}, \alpha, \beta, \Lambda} \Gamma_{\mathbf{k}, \mathbf{q}}^{\alpha\beta*} \langle \beta \mathbf{k} + \mathbf{q} | \hat{\rho}^{(1)} | \alpha \mathbf{k} \rangle = \frac{1}{(2\pi)^2} \int_{-\infty}^{\infty} d^2 \mathbf{q} e^{i\mathbf{q} \cdot \mathbf{r}} n_{2D}(\mathbf{q}, \omega). \tag{1.79}$$

Knowing the relations for the Fourier components of the induced electron density, one can proceed by replacing  $\langle \beta \mathbf{k} + \mathbf{q} | \hat{\rho}^{(1)} | \alpha \mathbf{k} \rangle$  and  $\Gamma_{\mathbf{k}, \mathbf{q}}^{\alpha\beta}$  with their full forms provided by Equations (1.71) and (1.76).

$$\begin{aligned}
 n_{2D}(\mathbf{q}, \omega) &= \Omega \sum_{\mathbf{k}, \alpha, \beta, \Lambda} \Gamma_{\mathbf{k}, \mathbf{q}}^{\alpha\beta*} \langle \beta \mathbf{k} + \mathbf{q} | \hat{\rho}^{(1)} | \alpha \mathbf{k} \rangle = \Omega \sum_{\mathbf{k}, \alpha, \beta, \Lambda} \left| \Gamma_{\mathbf{k}, \mathbf{q}}^{\alpha\beta} \right|^2 \frac{f_0^{\alpha\mathbf{k}} - f_0^{\beta\mathbf{k}+\mathbf{q}}}{E_0^{\alpha\mathbf{k}} - E_0^{\beta\mathbf{k}+\mathbf{q}} + \hbar\omega + i\hbar\gamma} V(\mathbf{q}) = \\
 &= \frac{V(\mathbf{q})}{\Omega} \sum_{\mathbf{k}, \alpha, \beta, \Lambda} \frac{f_0^{\alpha\mathbf{k}} - f_0^{\beta\mathbf{k}+\mathbf{q}}}{E_0^{\alpha\mathbf{k}} - E_0^{\beta\mathbf{k}+\mathbf{q}} + \hbar\omega + i\hbar\gamma} \left| \beta F_A^{(\Lambda)*}(\mathbf{k} + \mathbf{q}) \alpha F_A^{(\Lambda)}(\mathbf{k}) + \beta F_B^{(\Lambda)*}(\mathbf{k} + \mathbf{q}) \alpha F_B^{(\Lambda)}(\mathbf{k}) \right|^2.
 \end{aligned} \tag{1.80}$$

The last step resides in recalling the original expressions for the coefficients  $\alpha F_A^{(\Lambda)}(\mathbf{k})$ ,  $\alpha F_B^{(\Lambda)}(\mathbf{k})$ ,  $\beta F_A^{(\Lambda)}(\mathbf{k} + \mathbf{q})$  and  $\beta F_B^{(\Lambda)}(\mathbf{k} + \mathbf{q})$  and inserting them into the above equation

$$n_{2D}(\mathbf{q}, \omega) = \frac{V(\mathbf{q})}{\Omega} \sum_{\mathbf{k}, \alpha, \beta, \Lambda} \frac{f_0^{\alpha\mathbf{k}} - f_0^{\beta\mathbf{k}+\mathbf{q}}}{E_0^{\alpha\mathbf{k}} - E_0^{\beta\mathbf{k}+\mathbf{q}} + \hbar\omega + i\hbar\gamma} \left( \frac{1}{2} + \frac{1}{2} \alpha\beta \frac{|\mathbf{k}|^2 + |\mathbf{k} \cdot \mathbf{q}|}{|\mathbf{k}| |\mathbf{k} + \mathbf{q}|} \right). \tag{1.81}$$

Notice that in the above expression for the electron density, it does not matter anymore, whether we consider an eigenstate in the vicinity of the  $K$  or  $K'$  point, the dependence on the choice of the Dirac point has vanished. The summation over  $\Lambda$  then turns out to be just a multiplication of the above expression by a factor  $g_v = 2$  (known as the valley degeneracy). Furthermore, one should also account for the fact that one eigenstate can accommodate two electrons with opposite spins by introducing another factor  $g_s = 2$  (spin degeneracy).

Equation (1.81), linking together the induced electron density  $n_{2D}(\mathbf{q}, \omega)$  and the self-consistent potential  $V(\mathbf{q})$ , concludes this extensive section consisting mainly of quantum-mechanical calculations of graphene's response to an external perturbation.

## 1.7. Dynamical conductivity of graphene

The theory of electromagnetism in matter comprises many intriguing effects including the non-linearity and the anisotropy, but those phenomena are beyond the scope of this thesis. Throughout this work,

## 1.7. DYNAMICAL CONDUCTIVITY OF GRAPHENE

graphene is being treated only within the boundaries of the non-local linear response theory. In spite of this simplified description, there appears to be a plethora of effects in graphene worth of attention.

In the spirit of the non-local linear response theory (Bohren and Huffman [7], Chap. 2), the polarization vector  $\mathbf{P}(\mathbf{r}, t)$  in graphene is generally calculated as the convolution of the non-local dynamical susceptibility  $\chi_{2D}(\mathbf{r}, t)$  with the electric field vector  $\mathbf{E}(\mathbf{r}, t)$

$$\mathbf{P}(\mathbf{r}, t) = \frac{1}{(2\pi)^3} \int_{-\infty}^{\infty} d^2\mathbf{r}' \int_{-\infty}^{\infty} dt' \varepsilon_0 \chi_{2D}(\mathbf{r}-\mathbf{r}', t-t') \mathbf{E}(\mathbf{r}', z'=0, t'). \quad (1.82)$$

where  $\varepsilon_0$  stands for the vacuum permittivity.

Apparently, the polarization vector and the dynamical susceptibility are non-zero only in the plane of the graphene sheet set at  $z = 0$ , whereas the electric field must be defined in the whole space. This may have some interesting consequences for the mutual relations between the susceptibility, the conductivity and the dielectric function. The integration over the whole space and time reflects the possibility that the polarization of the material at some point in space and time may depend not only on the electric field at the given point and in the given time, but also on the field in the vicinity of that point and the field in the preceding time.

Although the above formulation of the graphene's response to an external electric field provides us with a good understanding of the spatial and temporal non-locality, the presence of the integrals makes further calculations cumbersome. A more suitable form is obtained by expressing the dynamical susceptibility in terms of its Fourier spectra and changing the order of integrations

$$\begin{aligned} \mathbf{P}(\mathbf{r}, t) &= \frac{1}{(2\pi)^3} \int_{-\infty}^{\infty} d^2\mathbf{r}' \int_{-\infty}^{\infty} dt' \int_{-\infty}^{\infty} d^2\mathbf{q} \int_{-\infty}^{\infty} d\omega e^{i\mathbf{q}\cdot(\mathbf{r}-\mathbf{r}')} e^{-i\omega(t-t')} \varepsilon_0 \chi_{2D}(\mathbf{q}, \omega) \mathbf{E}(\mathbf{r}', z'=0, t') = \\ &= \int_{-\infty}^{\infty} \frac{d^2\mathbf{q}}{(2\pi)^2} \int_{-\infty}^{\infty} d\omega e^{i\mathbf{q}\cdot\mathbf{r}} e^{-i\omega t} \varepsilon_0 \chi_{2D}(\mathbf{q}, \omega) \int_{-\infty}^{\infty} d^2\mathbf{r}' \int_{-\infty}^{\infty} \frac{dt'}{2\pi} e^{-i\mathbf{q}\cdot\mathbf{r}'} e^{i\omega t'} \mathbf{E}(\mathbf{r}', z'=0, t') = \\ &= \int_{-\infty}^{\infty} \frac{d^2\mathbf{q}}{(2\pi)^2} \int_{-\infty}^{\infty} d\omega e^{i\mathbf{q}\cdot\mathbf{r}} e^{-i\omega t} \varepsilon_0 \chi_{2D}(\mathbf{q}, \omega) \mathbf{E}(\mathbf{q}, z'=0, \omega) = \int_{-\infty}^{\infty} \frac{d^2\mathbf{q}}{(2\pi)^2} \int_{-\infty}^{\infty} d\omega e^{i\mathbf{q}\cdot\mathbf{r}} e^{-i\omega t} \mathbf{P}(\mathbf{q}, \omega), \end{aligned} \quad (1.83)$$

which is actually the well known convolution theorem.

According to the Gauss's law of electromagnetism, the induced charge density can be obtained as the divergence of the corresponding vector field, in this case the polarization  $\mathbf{P}(\mathbf{r}, t)$

$$-e n_{2D}(\mathbf{r}, t) = -\nabla \cdot \mathbf{P}(\mathbf{r}, t), \quad (1.84)$$

where  $e = 1.602 \cdot 10^{-19} \text{ C}$  is the elementary charge. The conversion to the Fourier domain is straightforward, assuming one may reverse the order of differentiation and integration

$$\begin{aligned}
 -e \int_{-\infty}^{\infty} \frac{d^2 \mathbf{q}}{(2\pi)^2} \int_{-\infty}^{\infty} d\omega e^{i\mathbf{q}\cdot\mathbf{r}} e^{-i\omega t} n_{2D}(\mathbf{q}, \omega) &= -\nabla \cdot \left[ \int_{-\infty}^{\infty} \frac{d^2 \mathbf{q}}{(2\pi)^2} \int_{-\infty}^{\infty} d\omega e^{i\mathbf{q}\cdot\mathbf{r}} e^{-i\omega t} \mathbf{P}(\mathbf{q}, \omega) \right], \\
 -e \int_{-\infty}^{\infty} \frac{d^2 \mathbf{q}}{(2\pi)^2} \int_{-\infty}^{\infty} d\omega e^{i\mathbf{q}\cdot\mathbf{r}} e^{-i\omega t} n_{2D}(\mathbf{q}, \omega) &= - \int_{-\infty}^{\infty} \frac{d^2 \mathbf{q}}{(2\pi)^2} \int_{-\infty}^{\infty} d\omega e^{i\mathbf{q}\cdot\mathbf{r}} e^{-i\omega t} [\mathbf{i} \mathbf{q} \cdot \mathbf{P}(\mathbf{q}, \omega)], \\
 \int_{-\infty}^{\infty} \frac{d^2 \mathbf{q}}{(2\pi)^2} \int_{-\infty}^{\infty} d\omega e^{i\mathbf{q}\cdot\mathbf{r}} e^{-i\omega t} [e n_{2D}(\mathbf{q}, \omega) - \mathbf{i} \mathbf{q} \cdot \mathbf{P}(\mathbf{q}, \omega)] &= 0,
 \end{aligned}$$

The last equation is fulfilled only if the integrand in the square brackets is identically equal to zero for all the frequencies  $\omega$  and wavevectors  $\mathbf{q}$ , leading to an equation linking the Fourier components of the induced electron density and the polarization vector

$$e n_{2D}(\mathbf{q}, \omega) = \mathbf{i} \mathbf{q} \cdot \mathbf{P}(\mathbf{q}, \omega) \quad (1.85)$$

The above procedure can be repeated for another pair of quantities, namely the electric field vector  $\mathbf{E}(\mathbf{r}, z, t)$  and a potential  $V(\mathbf{r}, z, t)$  (do not confuse with the self-consistent potential  $V(\mathbf{r}, t)$ ) tied through the following equation

$$\mathbf{E}(\mathbf{r}, z, t) = -\nabla V(\mathbf{r}, z, t), \quad (1.86)$$

with the result

$$\mathbf{E}(\mathbf{q}, z, \omega) = -\mathbf{i} \mathbf{q} V(\mathbf{q}, z, \omega). \quad (1.87)$$

Notice that by omitting the vector potential both in the above definition of the electric field and in the perturbed Hamiltonian introduced in the previous section, one neglects the retardation effects between distant parts of the graphene, thus treats its response within the quasistatic approximation.

Equations (1.83), (1.85) and (1.88) can be combined to give

$$e n_{2D}(\mathbf{q}, \omega) = \mathbf{i} \mathbf{q} \cdot \mathbf{P}(\mathbf{q}, \omega) = \mathbf{i} \varepsilon_0 \chi_{2D}(\mathbf{q}, \omega) \mathbf{q} \cdot \mathbf{E}(\mathbf{q}, z'=0, \omega) = q^2 \varepsilon_0 \chi_{2D}(\mathbf{q}, \omega) V(\mathbf{q}, z'=0, \omega), \quad (1.88)$$

where  $q = |\mathbf{q}|$  is the magnitude of the wavevector  $\mathbf{q}$ . Finally, by summoning the expression for the induced electron density given by Equation (1.81) and recalling that the self-consistent potential (or more precisely the potential energy) is, apart from a prefactor, equivalent to the electrostatic potential  $V(\mathbf{q}) = -e V(\mathbf{q}, z=0, \omega)$ , the desired expression for the non-local dynamical susceptibility is acquired

$$\begin{aligned}
 e g_v g_s \frac{V(\mathbf{q})}{\Omega} \sum_{\mathbf{k}, \alpha, \beta} \frac{f_0^{\alpha \mathbf{k}} - f_0^{\beta \mathbf{k} + \mathbf{q}}}{E_0^{\alpha \mathbf{k}} - E_0^{\beta \mathbf{k} + \mathbf{q}} + \hbar \omega + i \hbar \gamma} \left( \frac{1}{2} + \frac{1}{2} \alpha \beta \frac{|\mathbf{k}|^2 + |\mathbf{k} \cdot \mathbf{q}|}{|\mathbf{k}| |\mathbf{k} + \mathbf{q}|} \right) &= -\frac{q^2}{e} \varepsilon_0 \chi_{2D}(\mathbf{q}, \omega) V(\mathbf{q}), \\
 \chi_{2D}(\mathbf{q}, \omega) &= \frac{e^2 g_v g_s}{\Omega q^2 \varepsilon_0} \sum_{\mathbf{k}, \alpha, \beta} \frac{f_0^{\beta \mathbf{k} + \mathbf{q}} - f_0^{\alpha \mathbf{k}}}{E_0^{\alpha \mathbf{k}} - E_0^{\beta \mathbf{k} + \mathbf{q}} + \hbar \omega + i \hbar \gamma} \left( \frac{1}{2} + \frac{1}{2} \alpha \beta \frac{|\mathbf{k}|^2 + |\mathbf{k} \cdot \mathbf{q}|}{|\mathbf{k}| |\mathbf{k} + \mathbf{q}|} \right), \quad (1.89)
 \end{aligned}$$

with  $\gamma \rightarrow 0$ . Interestingly, the above equation has two degrees of freedom in the sense that there are two parameters, the temperature  $T$  and the Fermi energy  $E_F$ , which can be controlled from outside. Both these quantities enter the equation through the Fermi-Dirac distribution functions  $f_0^{\beta \mathbf{k} + \mathbf{q}}$  and

## 1.7. DYNAMICAL CONDUCTIVITY OF GRAPHENE

$f_0^{\alpha\mathbf{k}}$ . Invoking the expression describing the energy dispersion in the vicinity of the Dirac points given by Equation (1.31), one can write

$$f_0^{\alpha\mathbf{k}} = f_0(E_\alpha(\mathbf{k})) = \frac{1}{\exp\left(\frac{E_\alpha(\mathbf{k}) - E_F}{k_B T}\right) + 1} = \frac{1}{\exp\left(\frac{\alpha\hbar v_F |\mathbf{k}| - E_F}{k_B T}\right) + 1} \quad (1.90)$$

where  $k_B$  is the Boltzmann constant and  $\mathbf{k}$  is measured from the respective Dirac point  $\mathbf{\Lambda}$  (this does not affect the susceptibility nor any other related quantity, since the summation over  $\mathbf{k}$  is performed over the whole Brillouin zone so that  $\sum_{\mathbf{k}-\mathbf{\Lambda}} = \sum_{\mathbf{k}}$ ). Equation (1.89) is in many aspects very similar to the Linhard equation describing the electron screening in metals (Ashcroft and Mermin [4], p. 343, [25]).

The temperature  $T$  evidently affects the distribution of electrons in the vicinity of the Fermi level. Higher the temperature, the more is the distribution distorted from the Heaviside step function  $\theta(E_F - E_\alpha(\mathbf{k}))$ . As mentioned earlier, the adjustment of the Fermi level  $E_F$  has much more profound effect, since it can completely alter the optical properties of graphene. This can be seen by a detailed analysis of Equation (1.89).

First of all, the expression for the dynamical susceptibility is non-zero only if the difference of the two Fermi-Dirac distribution functions in the numerator is non-zero as well, which is equivalent to the statement that the scattering of electrons takes place only between occupied and unoccupied electronic states. The amplitude of the scattering is, besides other things, determined by the value of the denominator, which tends to infinity, when the difference in the energies assigned to those states is equal to the energy of the impinging photons, leading to a strong absorption of the incoming radiation. Figure 1.6 illustrates, how the adjustment of the Fermi level can suppress those strong optical transitions by setting a minimal energy required to overcome a newly created barrier between the occupied and eligible unoccupied states, where by eligible one means those states satisfying both the energy and the momentum conservation laws.

Since the momentum  $\hbar\mathbf{k}$  carried by photons is comparatively small (within the scale of the present diagram of graphene's energy dispersion the light line  $\hbar\omega = \hbar c\mathbf{k}$  practically coincides with the vertical axis), they can not induce lossy intraband transitions, in Figure 1.6 represented by the blue arrows. The only allowed optical transition is the vertical promotion of an electron from the lower to the upper band denoted by the red arrow.

First let us look, what happens if we shift the Fermi level from its default position at the Dirac point to higher energies (Fig. 1.6(b)). Some of the previously vacant states are now occupied and the corresponding transitions are therefore forbidden. Clearly, only those electrons with energy  $-E_F$  and less can be now scattered into the conduction band, provided that the energy of photons is at least twice the Fermi energy  $\hbar\omega = 2E_F$ . If the energy of photons does not reach this threshold value, there are no vertical interband transitions and the electrodynamic response of graphene is similar to that of a Drude metal (Maier [20], p. 11).

Shifting of the Fermi level to lower energies (Fig. 1.6(c)) leads to the formation of the barrier for the low energy interband transitions as well, only in this case it is due to an electron depletion in the valence band in the vicinity of the Dirac point.

Equation (1.89) describes the electrodynamic response of graphene, capturing both the intraband and interband processes. The effects of other types of scattering (impurities, phonons) can be incorporated through a phenomenological relaxation time constant  $\tau$ . Curiously, it can not be simply introduced to the present expressions as a small imaginary part of the frequency  $\omega + \frac{1}{\tau}$ , because such model would violate the local conservation of the electron number [24].

Mermin showed that the proper treatment provides a relaxation time approximation, where the collisions with impurities and phonons do not relax the electron density to its uniform distribution,

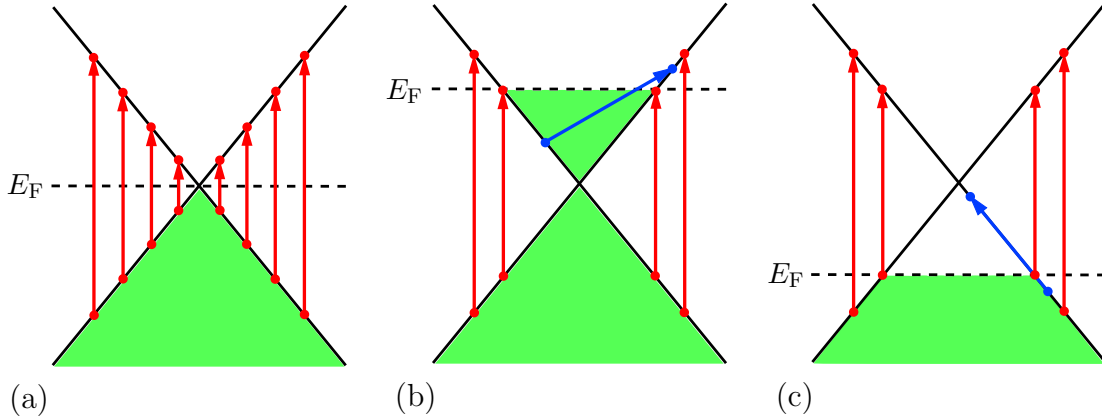


Figure 1.6: Optical transitions in graphene. (a) The allowed vertical interband transitions in undoped graphene. (b) By shifting the Fermi level to higher energies the low-energy transition become forbidden. (c) A depletion of the top of the valence band has a similar effect as in (b). The intraband transitions represented by blue arrows can not be induced by photons due to a large momentum mismatch.

but to a local equilibrium with respect to a local chemical potential, which may due to the external perturbation vary in space. Referring the reader for further information on this topic to [24], the dynamical susceptibility  $\chi_{2D}^{\tau}(\mathbf{q}, \omega)$  accounting for the scattering by impurities and phonons can be calculated in the following way

$$\chi_{2D}^{\tau}(\mathbf{q}, \omega) = \frac{\left(1 + \frac{i}{\omega\tau}\right) \chi_{2D}\left(\mathbf{q}, \omega + \frac{i}{\tau}\right)}{1 + \frac{i}{\omega\tau} \chi_{2D}\left(\mathbf{q}, \omega + \frac{i}{\tau}\right) \left[\chi_{2D}(\mathbf{q}, 0)\right]^{-1}}. \quad (1.91)$$

Although the above expressions for  $\chi_{2D}(\mathbf{q}, \omega)$  and  $\chi_{2D}^{\tau}(\mathbf{q}, \omega)$  provide a general and very illustrative description of the graphene's electrodynamical response, they are not that much suitable for calculations of the light scattering from systems involving graphene and other plasmonic structures, mainly because of the troublesome incorporation of the spatial dispersion into the current algorithms. These difficulties are usually solved by taking the  $q \rightarrow 0$  limit, entirely disregarding the spatial non-locality in graphene's response. Such approximation is perfectly justifiable for free-space electromagnetic waves with negligible in-plane momentum, but one has to be careful while dealing with structures with sharp edges and corners, where the fields may contain the high- $q$  Fourier components.

The local dynamical susceptibility  $\chi_{2D}^{\tau}(\omega)$  is obtained by evaluating the three sums over the wavevector  $\mathbf{k}$  and band indices  $\alpha, \beta$  in Equation (1.89) within the aforementioned limit  $q \rightarrow 0$ . Referring the reader for the detailed derivation to [12], the final expression for the local dynamical susceptibility reads

$$\chi_{2D}^{\tau}(\omega) = -\frac{2k_B T e^2}{\pi \epsilon_0 \hbar^2 \omega \left(\omega + \frac{i}{\tau}\right)} \ln \left[ 2 \cosh \left( \frac{E_F}{2k_B T} \right) \right] + i \frac{e^2}{4\hbar \epsilon_0 \omega} \left[ H\left(\frac{\omega}{2}\right) + \frac{4i\omega}{\pi} \int_0^{\infty} d\varepsilon \frac{H(\varepsilon) - H\left(\frac{\omega}{2}\right)}{\omega^2 - 4\varepsilon^2} \right] \quad (1.92)$$

$$H(\varepsilon) = \frac{\sinh\left(\frac{\hbar\varepsilon}{k_B T}\right)}{\cosh\left(\frac{E_F}{k_B T}\right) + \cosh\left(\frac{\hbar\varepsilon}{k_B T}\right)}. \quad (1.93)$$

## 1.7. DYNAMICAL CONDUCTIVITY OF GRAPHENE

Interestingly, there exists an analytical solution even for the non-local case provided that the temperature is approaching zero and the Fermi-Dirac statistic thus becomes a step function. The expressions for the non-local dynamical response of graphene in the  $T \rightarrow 0$  limit can be found for example in [32, 16, 18].

The dynamical susceptibility itself represents a suitable input for the light scattering calculations, but the response of graphene is, for some reasons, usually described in terms of the dynamical conductivity  $\sigma(\omega)$ . Invoking the Maxwell's equations and constitutive relations, the conductivity links together the induced current density  $\mathbf{j}$  and the electric field  $\mathbf{E}$  through

$$\mathbf{j}(\mathbf{r}, t) = \frac{1}{2\pi} \int_{-\infty}^{\infty} dt' \sigma(t-t') \mathbf{E}(\mathbf{r}, z=0, t'), \quad (1.94)$$

where only the non-locality in time is being considered. Employing the convolution theorem from Equation (1.83) and summoning the continuity equation  $\nabla \cdot \mathbf{j} + \frac{\partial}{\partial t} (-\nabla \cdot \mathbf{P}) = 0$ , one recovers the relation between the conductivity  $\sigma(\omega)$  and the dynamical susceptibility  $\chi_{2D}^T(\omega)$

$$\begin{aligned} \sigma(\omega) \mathbf{E}(\mathbf{r}, z'=0, \omega) &= \mathbf{j}(\mathbf{r}, \omega) = -i\omega \mathbf{P}(\mathbf{r}, \omega) = -i\omega \varepsilon_0 \chi_{2D}^T(\omega) \mathbf{E}(\mathbf{r}, z'=0, \omega) \\ \sigma(\omega) &= -i\omega \varepsilon_0 \chi_{2D}^T(\omega) \end{aligned} \quad (1.95)$$

Eventually, replacing  $\chi_{2D}^T(\omega)$  with its full form

$$\sigma(\omega) = \frac{2k_B T e^2}{\pi \hbar^2} \frac{i}{\left(\omega + \frac{i}{\tau}\right)} \ln \left[ 2 \cosh \left( \frac{E_F}{2k_B T} \right) \right] + \frac{e^2}{4\hbar} \left[ H\left(\frac{\omega}{2}\right) + \frac{4i\omega}{\pi} \int_0^{\infty} d\varepsilon \frac{H(\varepsilon) - H\left(\frac{\omega}{2}\right)}{\omega^2 - 4\varepsilon^2} \right] \quad (1.96)$$

where  $H(\varepsilon)$  is given by Equation (1.93). The crucial aspects of the local response become more lucid, if one decides to neglect the thermal effects by taking the  $T \rightarrow 0$  limit,

$$\sigma(\omega) = \frac{e^2 E_F}{\pi \hbar^2} \frac{i}{\left(\omega + \frac{i}{\tau}\right)} + \frac{e^2}{4\hbar} \left[ \theta(\hbar\omega - 2E_F) + \frac{i}{\pi} \ln \left| \frac{\hbar\omega - 2E_F}{\hbar\omega + 2E_F} \right| \right]. \quad (1.97)$$

The first term on the right-hand side of Equation (1.97) represents the Drude-like response of graphene, reflecting its metallic character when the Fermi level is shifted from its default position and the conduction band is partially filled (resp. the valence band is partially vacant). This term also accounts for the lossy intraband transitions due to impurities and lattice vibrations. The second term captures the influence of the interband transitions and their onset as the energy of impinging photons exceeds the threshold value  $2E_F$ .

For completeness, the real (dashed) and imaginary (solid) parts of the graphene's dynamical conductivity at two different temperatures (blue  $T = 10$  K, green  $T = 300$  K) are plotted in Figure 1.7. The Fermi level was set to  $E_F = 0.5$  eV and the relaxation time  $\tau = 10^{-13}$  s is assumed. There is a perceptible transition at the energy  $\hbar\omega = 2E_F$  between the low-frequency regime with graphene acting like a metal and the high-frequency regime, in which is the response of graphene governed by the interband processes. Apparently, the influence of temperature resides in the blurring of the transition between those two regimes.

Interestingly, for high frequencies the real part of the dynamical conductivity corresponding to losses acquires a universal value  $\sigma(\omega) = \frac{e^2}{4\hbar}$ , which results in the constant 97.7% transparency of graphene over a broad spectral range. The absorption of roughly 2.3% of the incoming light in the only one monolayer thick graphene sheet is a striking effect, although in terms of the utilization of graphene as a transparent conductor it might be rather perceived as a slight drawback.

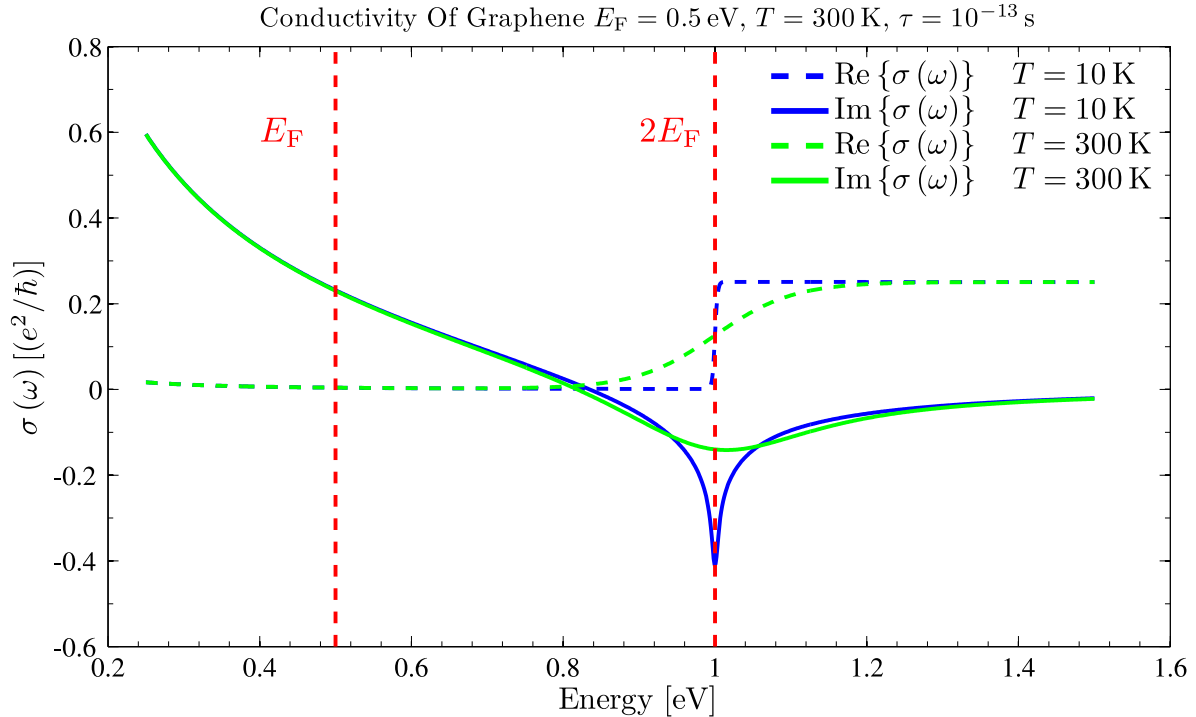


Figure 1.7: The real (dashed) and imaginary (solid) parts of the dynamical conductivity of graphene for two different temperatures  $T = 10$  K (blue) and  $T = 300$  K (green). The temperature affects the blurring of the onset of the interband transitions at the energy  $2E_F$ . The values  $E_F = 0.5$  eV for the Fermi energy and  $\tau = 10^{-13}$  s for the relaxation time have been used in both cases.

The electromagnetic power transmitted through or reflected from an infinite graphene sheet can be calculated using the Fresnel transmission and reflection coefficients. In principle, graphene could be modeled as a thin film with a nearly zero thickness [30], but such approach would require to assign to graphene some 3D dielectric function. Later we will derive for it an approximate expression, but the derivation itself is based on the preceding knowledge of the Fresnel coefficients. Ruling out the thin film approach, one can introduce the influence of the graphene sheet through surface charges and currents [18].

The graphene sheet divides the space into two halves, each characterized by a generally different dielectric constant  $\varepsilon$ . Without graphene, electromagnetic fields are required to satisfy the well known customary boundary conditions at the interface between those two halfspaces

$$\Delta \mathbf{E}_{\parallel} = 0, \quad \Delta (\varepsilon_0 \varepsilon \mathbf{E}_{\perp}) = 0, \quad \Delta \mathbf{H}_{\parallel} = 0, \quad \Delta \mathbf{H}_{\perp} = 0,$$

where  $\mathbf{E}$  and  $\mathbf{H}$  stand for the electric and magnetic fields,  $\varepsilon_0 \varepsilon \mathbf{E} = \mathbf{D}$  is the electric displacement and  $\parallel$  and  $\perp$  denote the parallel and perpendicular components with respect to the interface. The presence of graphene will, due to the surface charges and currents induced in it, result in a discontinuity in the normal component of the electric displacement and the tangential component of the magnetic field. Recalling the relations for the induced charge  $-en_{2D} = -\nabla \cdot \mathbf{P} = -\varepsilon_0 \chi_{2D}^T \nabla \cdot \mathbf{E}_{\parallel}$  and currents  $\mathbf{j} = \sigma \mathbf{E}_{\parallel}$ , the above boundary conditions become

$$\Delta \mathbf{E}_{\parallel} = 0, \quad \Delta (\varepsilon_0 \mathbf{E}_{\perp}) = -i \frac{\sigma}{\omega} \nabla \cdot \mathbf{E}_{\parallel}, \quad \Delta \mathbf{H}_{\parallel} = \sigma \mathbf{E}_{\parallel}, \quad \Delta \mathbf{H}_{\perp} = 0. \quad (1.98)$$

Figure 1.8 illustrates how an incident plane wave with a wavevector  $\mathbf{k}_i = (k_{\parallel}, 0, -k_{\perp}^{\perp})$  is partially reflected from, respectively partially transmitted through an interface consisting of an infinite graphene sheet squeezed between two media characterized by real dielectric constants  $\varepsilon_1$  (upper halfspace) and

## 1.8. PLASMONS IN GRAPHENE

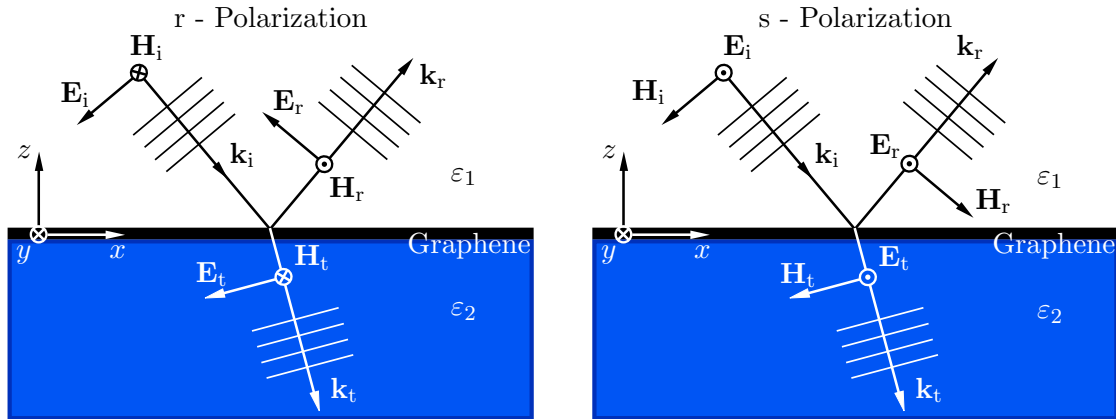


Figure 1.8: Schematic drawing of a plane wave being partially reflected from and transmitted through a graphene sheet squeezed between two media characterized by dielectric constants  $\varepsilon_1$  (upper halfspace) and  $\varepsilon_2$  (lower halfspace).

$\varepsilon_2$  (lower halfspace). The reflected and transmitted plane waves propagate in the directions given by the wavevectors  $\mathbf{k}_r = (k_{\parallel}, 0, k_1^{\perp})$  and  $\mathbf{k}_t = (k_{\parallel}, 0, -k_2^{\perp})$ . Using the notation and the orientation of the vectors as depicted in Figure 1.8, the Fresnel transmission and reflection coefficients in the presence of graphene read

$$t_p = \frac{2k_1^{\perp} \sqrt{\varepsilon_1} \sqrt{\varepsilon_2}}{\varepsilon_1 k_2^{\perp} + \varepsilon_2 k_1^{\perp} + \frac{\sigma}{\omega \varepsilon_0} k_1^{\perp} k_2^{\perp}}, \quad t_s = \frac{2k_1^{\perp}}{k_1^{\perp} + k_2^{\perp} + \frac{\sigma \omega}{\varepsilon_0 c^2}}, \quad (1.99)$$

$$r_p = \frac{\varepsilon_1 k_2^{\perp} - \varepsilon_2 k_1^{\perp} - \frac{\sigma}{\omega \varepsilon_0} k_1^{\perp} k_2^{\perp}}{\varepsilon_1 k_2^{\perp} + \varepsilon_2 k_1^{\perp} + \frac{\sigma}{\omega \varepsilon_0} k_1^{\perp} k_2^{\perp}}, \quad r_s = \frac{k_1^{\perp} - k_2^{\perp} - \frac{\sigma \omega}{\varepsilon_0 c^2}}{k_1^{\perp} + k_2^{\perp} + \frac{\sigma \omega}{\varepsilon_0 c^2}}, \quad (1.100)$$

where indices p and s denote the polarization of the electric field in the direction parallel and perpendicular to the plane of incidence.

## 1.8. Plasmons in graphene

The main reason for the increased interest in graphene within the plasmonic community over the past years is the existence of bound plasmonic modes in doped graphene, which is another manifestation of its metallic character.

Plasmons are coupled oscillations of the free electron plasma and the electromagnetic field. They appear in different forms, but graphene, being a planar structure, sustains only the surface mode denoted as a surface plasmon polariton (SPP). It can be described as a travelling evanescent wave, which propagates along the graphene sheet and decays exponentially in the directions perpendicular to it. The energy carried by these plasmons ranges from several meV up to 1 eV, the main parameter being the density of free charge carriers, resp. the Fermi energy  $E_F$ . Their propagation distance depends, besides other things, on the relaxation time  $\tau$ , which reflects the quality of the graphene's fabrication. Thanks to the suppression of scattering from defects and impurities due to the Klein tunneling [1], the relaxation time is considerably longer than in ordinary metals, resulting in acceptable propagation distances up to several microns, depending on the particular configuration [17]. Importantly, the confinement of the plasmons in graphene is quite remarkable, since it is possible to squeeze the light into volumes more than hundred times smaller compared to the free space.

The energy dispersion of the surface plasmon polaritons in graphene  $q_{sp}$  can be calculated using a standard procedure (Maier [20], p. 21), in which two surface waves, each of them exponentially

decaying into the respective halfspace, are matched at the graphene interface using the above boundary conditions. Here we choose an alternative approach exploiting the fact that the Fresnel reflection and transmission coefficients are valid also for evanescent waves.

Let us start with writing down the reflected electric field amplitudes  $\mathbf{E}_r$  in terms of the incident electric field  $\mathbf{E}_i$  for both polarizations s and p (notice that for evanescent waves the designation "reflected" and "transmitted" somewhat loses its original sense)

$$\mathbf{E}_r^p = r_p \mathbf{E}_i^p = \frac{\varepsilon_1 k_2^\perp - \varepsilon_2 k_1^\perp - \frac{\sigma}{\omega \varepsilon_0} k_1^\perp k_2^\perp}{\varepsilon_1 k_2^\perp + \varepsilon_2 k_1^\perp + \frac{\sigma}{\omega \varepsilon_0} k_1^\perp k_2^\perp} \mathbf{E}_i^p, \quad (1.101)$$

$$\mathbf{E}_r^s = r_s \mathbf{E}_i^p = \frac{k_1^\perp - k_2^\perp - \frac{\sigma \omega}{\varepsilon_0 c^2}}{k_1^\perp + k_2^\perp + \frac{\sigma \omega}{\varepsilon_0 c^2}} \mathbf{E}_i^s, \quad (1.102)$$

Since the surface plasmon polaritons are in fact the electromagnetic eigenmodes of the system, they should be self-sustainable and exist even if there is no external field to excite them  $\mathbf{E}_i^p = \mathbf{E}_i^s = 0$ . But such situation is possible only if the Fresnel coefficients in Equations (1.101), (1.102) tend to infinity and thus the problem of finding the energy dispersion of surface plasmon polaritons in graphene transforms into searching for the poles in the Fresnel coefficients.

First let us focus on the transverse magnetic (TM) mode associated with the p-polarization. Evidently, the expression for  $r_p$  diverges when the denominator is equal to zero

$$\varepsilon_1 k_2^\perp + \varepsilon_2 k_1^\perp + \frac{\sigma(\omega)}{\omega \varepsilon_0} k_1^\perp k_2^\perp = 0, \quad (1.103)$$

$$\frac{\varepsilon_1}{k_1^\perp} + \frac{\varepsilon_2}{k_2^\perp} + \frac{\sigma(\omega)}{\omega \varepsilon_0} = 0. \quad (1.104)$$

By rewriting the above equation using the in-plane wavenumber component  $k^\parallel = q_{\text{sp}} = \sqrt{\varepsilon_j \frac{\omega^2}{c^2} - k_j^{\perp 2}}$ ,  $j = 1, 2$ , the equation for the propagation constant  $q_{\text{sp}}$  is recovered

$$\frac{\varepsilon_1}{\sqrt{q_{\text{sp}}^2 - \varepsilon_1 \frac{\omega^2}{c^2}}} + \frac{\varepsilon_2}{\sqrt{q_{\text{sp}}^2 - \varepsilon_2 \frac{\omega^2}{c^2}}} + i \frac{\sigma(\omega)}{\omega \varepsilon_0} = 0. \quad (1.105)$$

Notice that  $q_{\text{sp}} > \sqrt{\varepsilon_j \frac{\omega}{c}}$  so that both  $k_1^\perp$  and  $k_2^\perp$  are imaginary, which is necessary in order the mode was bound to the graphene sheet.

The above equation provides a full description of the energy dispersion of TM surface plasmon polaritons in graphene, but the general solution lacks clarity. Fortunately, the main aspects of the dispersion are preserved if one simplifies the equation by supposing  $q_{\text{sp}} \gg \sqrt{\varepsilon_j \frac{\omega}{c}}$  and  $\hbar \omega < 2E_F$  so that  $\sqrt{q_{\text{sp}}^2 - \varepsilon_1 \frac{\omega^2}{c^2}} \approx q_{\text{sp}}$  and  $\sigma(\omega) \approx \frac{e^2 E_F}{\pi \hbar^2} \frac{i}{(\omega + \frac{i}{\tau})}$ . As we shall see, the first approximation is satisfied for all the TM modes except the ones with a very small energy compared to the Fermi level. The validity of the other approximation expires once the energy of the plasmon polaritons is large enough to induce an interband transition. Adopting the above assumptions, the relation for the energy dispersion of the TM plasmon polaritons becomes

$$q_{\text{sp}} = \frac{\varepsilon_1 + \varepsilon_2}{2} \frac{2\varepsilon_0 \pi \hbar^2}{e^2 E_F} \left( \omega^2 + i \frac{\omega}{\tau} \right). \quad (1.106)$$

The quadratic dependence of the propagation constant  $q_{\text{sp}}$  on the frequency  $\omega$  is characteristic for 2D electron gases. Figure 1.9 shows this dependence for two substrates  $\varepsilon_2 = 1$  (black) and  $\varepsilon_2 = 4$  (green) together with a map of eligible electronic transitions in graphene. A map in the sense that it tells us,

### 1.8. PLASMONS IN GRAPHENE

which combinations of the energy and the momentum can induce intraband (blue region) or interband (red region) transitions. Apparently, the TM surface plasmon polaritons can not directly decay into electron-hole pairs within one band, since the dispersion curve never enters the blue region of the energy-momentum space. On the other hand, the TM surface plasmon polaritons corresponding to that part of the dispersion curve lying inside the red region (dashed line) are strongly damped due to interband processes. It appears that the best propagation distance to confinement ratio is found for plasmons with an energy  $\hbar\omega_{\text{pl}} \approx E_{\text{F}}$ .

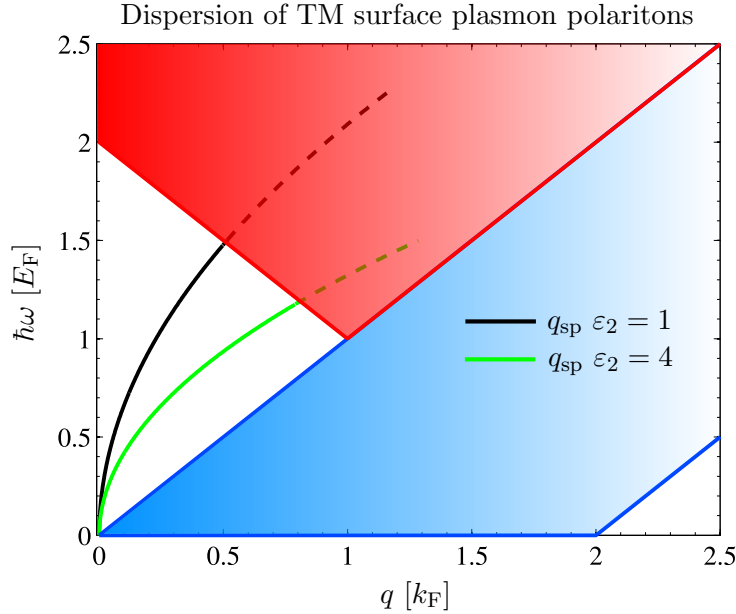


Figure 1.9: The energy dispersion of the TM surface plasmon polaritons in graphene for two values of the substrate dielectric constant  $\varepsilon_2 = 1$  (black) and  $\varepsilon_2 = 4$  (green). A strong damping of the plasmons due to intraband (blue region) and interband (red region) transitions is indicated by the dashed line.

The last remark regards the validity of the square root dispersion for small and large values of  $q_{\text{sp}}$ . It would seem that the dispersion curve crosses near the origin the light line, which in this case almost coincides with the vertical axis. But one has to keep in mind that we made some approximations and the proper dispersion curve is tangent to the light line in the limit  $q_{\text{sp}} \rightarrow 0$  as it should be. Similarly, the energy dispersion deviates significantly from the quadratic one for large values of the propagation constant due to the onset of the interband transitions.

The transverse electric (TE) mode associated with the s-polarization corresponds to poles in the Fresnel coefficients  $r_s$  and  $t_s$

$$k_1^\perp + k_2^\perp + \frac{\omega\sigma(\omega)}{\varepsilon_0 c^2} = 0, \quad (1.107)$$

$$\sqrt{q_{\text{sp}}^2 - \varepsilon_1 \frac{\omega^2}{c^2}} + \sqrt{q_{\text{sp}}^2 - \varepsilon_2 \frac{\omega^2}{c^2}} - i \frac{\omega\sigma(\omega)}{\varepsilon_0 c^2} = 0. \quad (1.108)$$

where  $q_{\text{sp}}$  is again assumed to be larger than  $\sqrt{\varepsilon_j} \frac{\omega}{c}$  so that the mode is bound. Unlike the TM mode, one can not neglect  $\varepsilon_j \frac{\omega^2}{c^2}$  against  $q_{\text{sp}}^2$  or disregard the influence of interband transitions without distorting substantially the proper general solution. In fact, the additional terms in the dynamical conductivity enable the very existence of the TE mode in the first place. That can be seen by a detailed analysis of the above equation.

Apparently, Equation (1.107) can be fulfilled only if the term  $i \frac{\omega\sigma(\omega)}{\varepsilon_0 c^2}$  is positive, which is true as long as the imaginary part of the conductivity is negative. Referring to Figure 1.7, such requirement is met only near the onset of the interband transitions and it corresponds to the logarithm term in the dynamical conductivity given by Equation (1.97).

Importantly, the proper solution of the above equation indicates that the propagation constant  $q_{\text{sp}}$  of the TE plasmonic polaritons in graphene is close to the propagation constant of light  $k = \frac{\omega}{c}$ , resulting in a large decay length in the direction perpendicular to the graphene sheet. Hence the TM mode appears to be a more suitable candidate for applications, in which the confinement plays a crucial role.

Let us conclude this topic with a remark that there is no counterpart to the TE modes in the classical plasmonic materials like gold or silver, which further emphasizes the graphene's uniqueness. A more extensive discussion on the TE modes in graphene can be found in [26].

## 1.8. PLASMONS IN GRAPHENE

## 2. Fabrication of graphene

If graphene is expected to find a utilization not only in the scientific community, but also in commercial devices, it is necessary to master its fabrication on a large scale and in sufficient quality using reliable and cheap methods. The research in this area has made a significant progress since the first successful isolation of graphene in 2004 by Novoselov and Geim. This chapter overviews the most promising fabrication techniques [9] and describes how one can tune the electric and optical properties of graphene.

The original method employed by Geim and Novoselov resides in the repeated peeling of small flakes from a piece of graphite using a Scotch tape. Although such mechanical exfoliation seems to be somewhat primitive, the graphene flakes prepared in this way boast with superior free charge carrier mobilities. Unfortunately, the procedure is limited to small sizes and it can not be scaled for the industrial production.

The next technique is based on the thermal decomposition of silicon carbide SiC, where the increased temperature causes the sublimation of Si atoms and the subsequent formation of a thin graphite layer on the top of the crystal. Even though this approach enables a large scale production, there are still several problems concerning the repeatability and the control over the number of grown monolayers.

The currently most spread fabrication method relies on growing graphene on a copper substrate using the chemical vapour deposition (CVD), where the Cu crystal is exposed to CH<sub>4</sub>-Ar-H<sub>2</sub> environment at an increased temperature and at the atmospheric pressure. Not only that the CVD enables a large scale production, the thickness of the grown carbon film is predominantly one monolayer regardless of the exposure time, indicating that the process is surface mediated and self limited. Moreover, by tuning the whole procedure, one can achieve mobilities of free charge carriers, which are comparable to those observed in exfoliated graphene. Table 2 summarizes the typical parameters of graphene flakes, resp. wafers fabricated using the above techniques.

Method	Layers	Size	Mobility (cm <sup>2</sup> V <sup>-1</sup> s <sup>-1</sup> )
Exfoliation	1-10+	1 mm <sup>2</sup>	15000
Thermal SiC	1-4	50 μm <sup>2</sup>	2000
Cu CVD	1	65 cm <sup>2</sup>	16000

Table 2.1: Comparison of the three, at the present most frequently used graphene fabrication techniques in terms of the number of grown monolayers, the size and the mobility of free charge carriers. (Adopted from [9])

Besides the methods described above, there exists a number of various preparation techniques such as the molecular beam epitaxy (MBE) or the carbon nanotubes unzipping, each with its advantages and drawbacks, but so far they remain in the shadow of the dominating CVD.

Importantly, the mobility of the free charge carriers in graphene is significantly affected by the type of the substrate it is lying on. For example, the values presented in Table 2 correspond to measurements on a glass substrate SiO<sub>2</sub>, but by using the boron nitride or suspended graphene one could achieve values even several times larger. The transfer of the graphene sheet from the "growing" material (Cu in the case of the CVD) on other substrates can be done using the following procedure.

At first a sufficiently thick layer of photoresistive poly-methyl-methacrylate (PMMA) is deposited onto the graphene sheet. Subsequently, the supporting material is carefully removed by etching so

that graphene itself remains glued to the photoresist. The whole structure is then transferred on the desired substrate and the PMMA is washed away by acetone.

As demonstrated in Section 1.8, the electrical and optical properties of graphene strongly depend on the position of the Fermi level with respect to the Dirac points. If one was able to control it dynamically, graphene might be used as an active element in modulators, transistors and many other devices. Interestingly, it can be accomplished through the ambipolar field effect, where graphene is used as an electrode in a parallel plate capacitor. The situation is illustrated in Figure 2.1. When a voltage is applied, the electrodes of the capacitor become oppositely charged, which projects into a slight shift of the Fermi levels within the electrodes. In the case of an electrode made of a classical metal, the effect would be negligible due to the huge intrinsic density of free charge carriers, but in graphene the shift can reach values up to 500 meV.

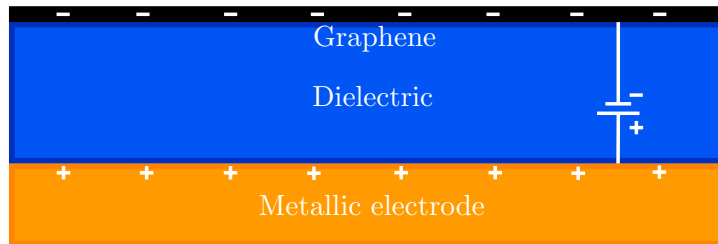


Figure 2.1: Schematic drawing of a parallel plate capacitor with a graphene sheet as one of the electrodes.

Invoking the Gauss's law of electromagnetism, the surface charge density  $n_S$  induced at the capacitor's electrodes is proportional to the applied voltage  $V$  and inversely proportional to the distance  $d$  between them

$$n_S = -\frac{\varepsilon_0 \varepsilon V}{d}, \quad (2.1)$$

where  $\varepsilon_0$  is the vacuum permittivity and  $\varepsilon$  is the permittivity of the dielectric separating those two electrodes. Identifying the surface charge density as the density of free charge carriers  $n$  given by Equation (1.42) multiplied by the elementary charge  $e$ , one finds that the shift of the Fermi level  $E_F$  due to the ambipolar field effect should be

$$E_F = \sqrt{\frac{4\pi\varepsilon_0\varepsilon\hbar^2 v_F^2 V}{g_s g_v e d}}. \quad (2.2)$$

The experimentally achieved values of the density of free charge carriers in graphene occur typically in the range of  $10^{11} - 10^{13} \text{ cm}^{-2}$ , which allows one to tune the Fermi level in the interval of roughly 10-400 meV (the lower limit originates in thermal and other effects).

### 3. Applications of graphene

The large number of published scientific articles and papers involving graphene reflects its huge potential for applications in optoelectronics, nanophotonics and other related areas, even though a long way has to be covered before the graphene-based devices will outperform the present ones relying on semiconductors. This chapter provides an overview of possible applications, in which graphene is expected to play a key role in the future.

The combination of the good conductivity and transparency makes graphene an interesting alternative to currently used indium-tin-oxide (ITO) as the top transparent electrode in touch screens and photovoltaic devices. Furthermore, its flexibility and durability could enable fabrication of rollable OLED displays and solar cells, which proves to be unfeasible with the brittle ITO [9]. Recently, 4-layer doped graphene sheets with resistivity as low as  $30 \Omega W^{-1}$  and optical transmittance greater than 90% have been produced, surpassing the currently commercially available ITO sheets with comparable transmittance and resistivity around  $100 \Omega W^{-1}$  [6].

Although the employment of graphene as a flexible transparent electrode will probably improve the performance of the current devices, it can be hardly perceived as a far-reaching breakthrough. On the other hand, the fact that graphene can act as an active element could lead to novel and disruptive technologies. This concerns mainly the optical modulators, photodetectors, lasers, high-frequency transistors, polarizers, optical insulators and other electric and optoelectronic devices [27].

As regards the utilization of graphene in plasmonics, there are basically two paths one can follow at the present. The first concept directly exploits graphene for guiding and controlling the plasmons, whereas the latter approach rather uses graphene to control the response and to enhance the performance of ordinary plasmonic structures, or even to form hybrid devices with novel features. Let us now inspect in a more detail some of the possible applications.

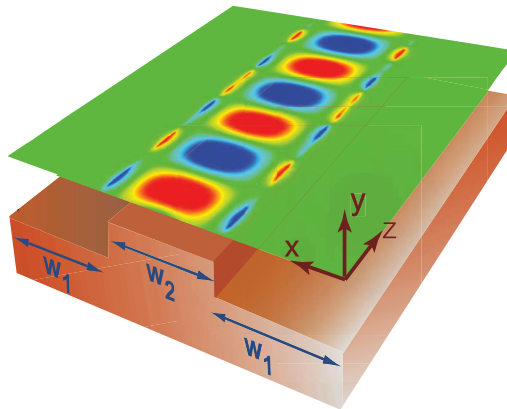


Figure 3.1: Schematic drawing of a graphene-based plasmonic waveguide. The transition between regions, which do or do not sustain TM surface plasmon polaritons, is achieved by structuring the dielectric layer between the graphene sheet and the gating electrode. (Adapted from [31])

Since the damping and confinement of plasmons in graphene is more favourable than in traditional noble metals, we might experience a revival in the plasmonic circuitry and the plasmonic transformation optics. Vakil and Engheta [31] presented a simple and intriguing way how to guide and control surface plasmon polaritons in graphene by structuring the dielectric layer between the graphene sheet and the gating electrode as depicted in Figure 3.1. The variations in the thickness or dielectric properties of that layer project into local changes in the chemical potential of graphene, which results in

a formation of regions with different conductivities. If the gating voltage is properly set, only certain regions will be able to sustain the TM surface plasmonic polaritons. By structuring the dielectric layer in the shape of stripes, one obtains plasmonic waveguides with properties tunable through the gating voltage. The authors also proposed that the above concept could be employed to create more sophisticated optical elements like plasmonic beamsplitters, lenses or 2D metamaterials.

The ability of graphene to influence the response of other plasmonic structures was clearly demonstrated by Kravets et al. [19]. They transferred a single graphene sheet on the top of a regular array of plasmonic antennas with ultranarrow diffractive-coupled plasmon resonances, which show extremely high phase sensitivity to the external environment. The presence of graphene resulted in a significant spectral shift of the coupled resonances and changes in other optical properties of the plasmonic array. Subsequently, they altered the properties of graphene by the reversible hydrogenation, observing a superb sensitivity to that process.

Those were only two examples of the possible utilization of graphene, but they should give the reader a certain feeling of its great potential to push the boundaries and limits of the current technologies.

## 4. Proposed experimental setup: Motivation

The major goals of this diploma thesis are to investigate the influence of graphene on a single plasmonic structure and to assess, whether it is possible to dynamically tune its response by changing the chemical potential in graphene through the electrostatic gating. Furthermore, one of the outcomes of this thesis should be a layout of an experiment, which would demonstrate the control over the response of the plasmonic structure.

Recently, Yu et al. [33] have presented an intriguing concept, in which plasmonic structures are used to transform a beam of light in such a way that an impression of the anomalous refraction is evoked. The proposed configuration is illustrated in Figure 4.1. An array of  $N$  noble metal plasmonic nanoantennas (their shape remains for now unspecified) is deposited onto a substrate characterized by a dielectric constant  $\varepsilon_2$ , while the superstrate is described by  $\varepsilon_1$ . Let us assume an incident plane wave propagating in the direction prescribed by a wavevector  $\mathbf{k}_i$ .

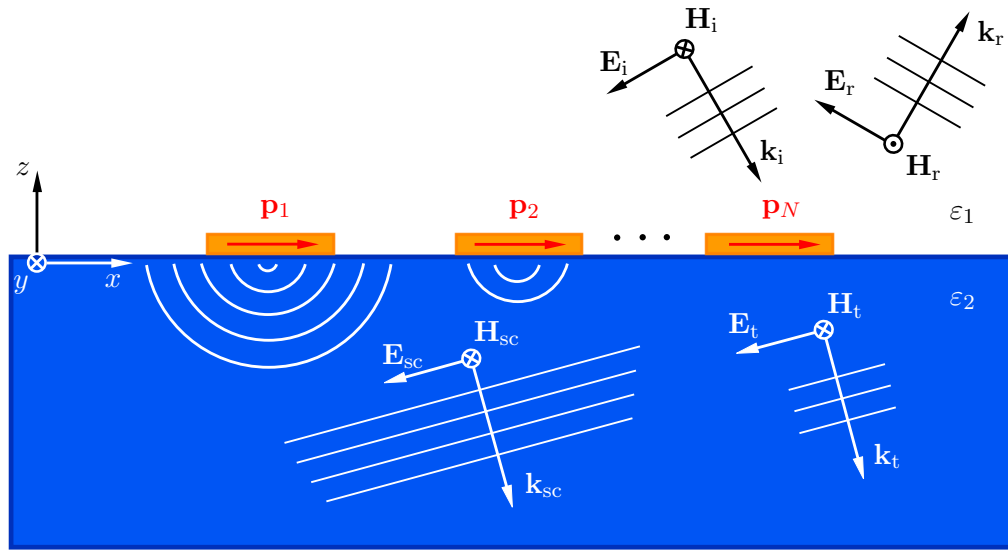


Figure 4.1: Schematic drawing of an array of  $N$  plasmonic antennas illuminated by an electromagnetic plane wave propagating in the direction given by a wavevector  $\mathbf{k}_i$ . The incident plane wave induces in the antennas oscillating dipoles  $\mathbf{p}$  so that apart from the reflected ( $\mathbf{k}_r$ ) and refracted ( $\mathbf{k}_t$ ) waves, radiation corresponding to scattering by the antennas ( $\mathbf{k}_{sc}$ ) is observed.

Evidently, the incident plane wave will be partially reflected, partially refracted and some of the power will be scattered and absorbed by the metallic antennas. If the antennas are identical, the radiation scattered by the individual antennas will superpose to form two plane waves propagating in the directions prescribed by the well known Snell's law. Therefore, the far field angular distribution consists of only two maxima corresponding to the ordinary reflection from, resp. transmission through a planar interface, although the amplitudes of the respective waves are modified by the presence of the plasmonic nanoarray. Let us now express the above statements in a suitable mathematical form.

For simplicity, we shall assume that the plasmonic antennas are shaped as infinitely long cylinders with radiation patterns similar to that of a line dipole. This will reduce the problem to only two dimensions, while preserving the main idea. The electric field at the point  $\mathbf{r} = (x, z)$  due to the  $j$ -th dipole positioned at  $\mathbf{r}_j = (x_j, z_j)$  can be written as

$$\mathbf{E}_j(x, z) = i\omega\mu_0 \overset{\leftrightarrow}{\mathbf{G}}(x, z, x_j, z_j) \mathbf{j}(x_j, z_j), \quad (4.1)$$

where  $\mathbf{j}(x_j, z_j)$  is the induced current associated with the  $j$ -th dipole and where the  $3 \times 3$  tensor  $\overset{\leftrightarrow}{\mathbf{G}}(x, z, x_j, z_j)$ , also known as the dyadic Green's function, captures all the aspects of the dipole's radiation pattern including the radial dependence and the angular distribution. At this point, we shall use only an approximate form of the dyadic Green's function, although later the exact expression will be derived.

Far away from the line dipole all the near-field components of  $\overset{\leftrightarrow}{\mathbf{G}}(x, z, x_j, z_j)$  practically vanish and the spatial dependence of the electric field is dominated by the term corresponding to an outgoing cylindrical wave, which amplitude falls as the square root of the distance from the dipole

$$\mathbf{E}_j(x, z) \sim \frac{e^{ik_\nu \sqrt{(x-x_j)^2 + (z-z_j)^2}}}{\sqrt[4]{(x-x_j)^2 + (z-z_j)^2}}, \quad (4.2)$$

where  $k_\nu = \sqrt{\varepsilon_\nu} \frac{\omega}{c}$ ,  $\nu = 1, 2$  is the magnitude of the wavevector in the respective medium. Introducing polar coordinates  $r = \sqrt{x^2 + z^2}$ ,  $\varphi = \arctan\left(\frac{z}{x}\right)$  and assuming that all the line dipoles are confined to a small region near the origin of the coordinate system  $x_j, z_j \ll r$ , the total electric field  $\mathbf{E}$  is approximately given by

$$\mathbf{E}(r, \varphi) = \sum_j^N \mathbf{E}_j(r, \varphi) \approx \overset{\leftrightarrow}{\mathbf{G}}_\nu(\varphi) \frac{e^{ik_\nu r}}{\sqrt{k_\nu r}} \sum_j^N e^{-ik_\nu(x_j \cos \varphi + z_j \sin \varphi)} \mathbf{j}(x_j, z_j), \quad (4.3)$$

where  $\overset{\leftrightarrow}{\mathbf{G}}(\varphi)$  accounts for the angular distribution of an individual line dipole. Notice that the binomial theorem  $(1+x)^n \approx 1+nx$ ,  $x \ll 1$  has been used for the approximate evaluation of the exponential factor in Equation (4.2).

Since the whole plasmonic nanoarray is illuminated by a plane wave, the induced dipole moments should all have the same magnitude and orientation, although their phases may be mutually shifted as the result of an oblique incidence of the plane wave. Furthermore, recalling that all the line dipoles are positioned at the superstrate-substrate interface set at  $z=0$ , the above equation reads

$$\mathbf{E}(r, \varphi) = \sum_j^N \mathbf{E}_j(r, \varphi) \approx \overset{\leftrightarrow}{\mathbf{G}}_\nu(\varphi) \frac{e^{ik_\nu r}}{\sqrt{k_\nu r}} \sum_j^N e^{-ik_\nu^\parallel x_j} \mathbf{j} e^{ik_i^\parallel x_j}, \quad (4.4)$$

where the exponential factor  $e^{ik_i^\parallel x_j}$  accounts for the possible tilted illumination and where the following notation has been introduced  $k_\nu \cos \varphi = k_\nu^\parallel$ ,  $k_\nu \sin \varphi = k_\nu^\perp$  (clearly, the symbols  $\parallel$  and  $\perp$  stand for the directions parallel and perpendicular to the superstrate-substrate interface).

Finally assuming that the spacing  $\Delta x_j$  between the individual antennas is much smaller than the wavelength associated with the incident plane wave  $\lambda = \frac{2\pi}{k_\nu} \gg \Delta x_j$ , one can replace (to some extent) the discrete summation over  $j$  by continuous integration

$$\mathbf{E}(r, \varphi) \approx \overset{\leftrightarrow}{\mathbf{G}}_\nu(\varphi) \frac{e^{ik_\nu r}}{\sqrt{k_\nu r}} \mathbf{j} \frac{N}{L} \int_{-\frac{L}{2}}^{\frac{L}{2}} dx' e^{i(k_i^\parallel - k_\nu^\parallel)x'}. \quad (4.5)$$

The antennas are confined in a region of a length  $L \ll \lambda$  and the factor  $\mathbf{j} \frac{N}{L}$  accounts for the proper normalization of the induced current density. The above integral is readily evaluated to give

$$\mathbf{E}(r, \varphi) \approx \overset{\leftrightarrow}{\mathbf{G}}_\nu(\varphi) \frac{e^{ik_\nu r}}{\sqrt{k_\nu r}} \mathbf{j} \frac{2N}{L} \frac{\sin\left[\left(k_i^\parallel - k_\nu^\parallel\right) \frac{L}{2}\right]}{\left(k_i^\parallel - k_\nu^\parallel\right)} = \overset{\leftrightarrow}{\mathbf{G}}_\nu(\varphi) \frac{e^{ik_\nu r}}{\sqrt{k_\nu r}} N \mathbf{j} \operatorname{sinc}\left[\left(k_i^\parallel - k_\nu^\parallel\right) \frac{L}{2}\right]. \quad (4.6)$$

#### 4. PROPOSED EXPERIMENTAL SETUP: MOTIVATION

The  $\text{sinc}(x)$  function (from the Latin sinus cardinalis) has only one distinct maximum at  $x = 0$ , thus the amplitude of the scattered field will be significant only in those directions, for which  $k_\nu^\parallel = k_i^\parallel$ . Evidently, it corresponds to the directions of the ordinary reflection and refraction given by the Snell's law, which can be seen by expressing the parallel components of the respective wavevectors in terms of the angles  $\theta_\nu$ ,  $\theta_i$  formed by those wavevectors and the normal vector of the superstrate-substrate interface

$$k_\nu^\parallel = \sqrt{\varepsilon_\nu} \frac{\omega}{c} \sin \theta_\nu, \quad k_i^\parallel = \sqrt{\varepsilon_1} \frac{\omega}{c} \sin \theta_i.$$

The conditions for the maximal amplitudes in the upper ( $\nu = 1$ ) and lower ( $\nu = 2$ ) halfspaces then become

$$\sin \theta_1 = \sin \theta_i, \quad \sqrt{\varepsilon_2} \sin \theta_2 = \sqrt{\varepsilon_1} \sin \theta_i. \quad (4.7)$$

Apparently, the array of plasmonic antennas acts as if it was a thin homogenous metallic layer, however with the spectral response of a single antenna. This is the consequence of the transition from the summation over discrete dipoles to the integration over a continuous current density. In reality, the spacing between the antennas may project into the far-field angular distribution as satellite peaks. Furthermore, the coupling between individual antennas may smooth or even suppress the resonant features in their spectral response.

Importantly, the above derivation was based on the assumption that the antennas are identical. Yu et al. [33] have demonstrated that by varying their shape in a certain fashion one can introduce an additional phase shift between the induced dipoles, leading to a deviation of the scattered waves from the directions associated with the ordinary reflection and refraction.

Denoting the additional phase shift  $\Phi(x_j)$ , the total scattered field reads

$$\mathbf{E}(r, \varphi) = \sum_j^N \mathbf{E}_j(r, \varphi) \approx \overset{\leftrightarrow}{\mathbf{G}}_\nu(\varphi) \frac{e^{ik_\nu r}}{\sqrt{k_\nu r}} \sum_j^N e^{-ik_\nu^\parallel x_j} \mathbf{j} e^{ik_i^\parallel x_j} e^{i\Phi(x_j)}. \quad (4.8)$$

Eventually, assuming the antennas are modified in such a way that the phase shift is linear in  $x_j$ , the above equation becomes

$$\mathbf{E}(r, \varphi) \approx \overset{\leftrightarrow}{\mathbf{G}}_\nu(\varphi) \frac{e^{ik_\nu r}}{\sqrt{k_\nu r}} \mathbf{j} \frac{N}{L} \int_{-\frac{L}{2}}^{\frac{L}{2}} dx' e^{i(k_i^\parallel - k_\nu^\parallel + \kappa)x'} = \overset{\leftrightarrow}{\mathbf{G}}_\nu(\varphi) \frac{e^{ik_\nu r}}{\sqrt{k_\nu r}} N \mathbf{j} \text{sinc} \left[ \left( k_i^\parallel - k_\nu^\parallel + \kappa \right) \frac{L}{2} \right]. \quad (4.9)$$

where  $\kappa = \frac{\partial}{\partial x} \Phi(x)$  indicates how rapidly the phase shift varies between two induced dipoles. Notice, that once more the summation was replaced by integration, which is justified for a sufficiently dense array of plasmonic antennas. Obviously, the directions with the maximal scattering amplitude no longer coincide with those corresponding to the ordinary reflection and refraction. This deviation can be both positive and negative, depending on the sign of  $\kappa$ .

Although one can tailor the phase shift of the antennas by modifying their shape, their collective response is set and can not be changed, once the whole array is fabricated. The novel concept, which this thesis brings up, resides in the following idea. If the electrostatically doped graphene proved to be capable of a control over the response of the individual antennas, one might be able to dynamically tune the scattering properties of the whole plasmonic array including the direction of the maximal scattering amplitude. Figure 4.2 illustrates how such a control could be achieved.

A gradual reduction in the thickness of the dielectric layer separating the graphene sheet from the gating electrode should project into a spatial variation of the chemical potential within graphene. Since the plasmonic structures are usually quite sensitive to the ambient environment, the non-uniform

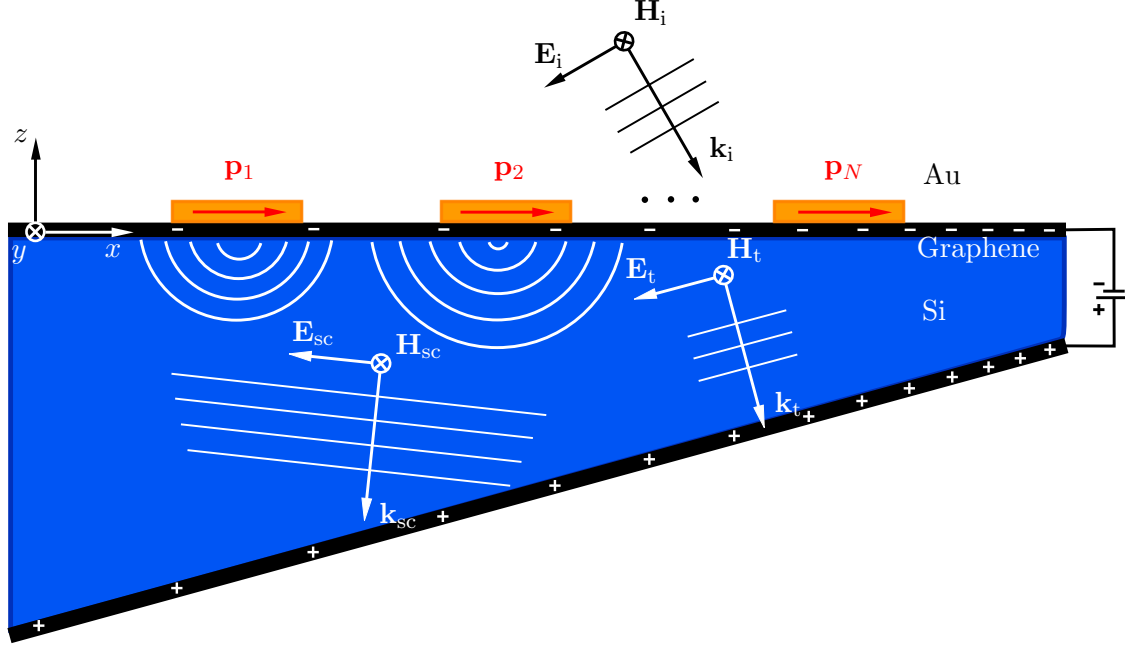


Figure 4.2: Schematic drawing of an array of  $N$  plasmonic antennas fabricated on top of a non-uniformly gated graphene sheet illuminated by an electromagnetic plane wave. The variations in the chemical potential within graphene may induce an additional phase shift between the dipoles  $\mathbf{p}$  so that the impression of a partial anomalous refraction is evoked.

gating of graphene might cause a variable shift in the resonant frequencies and lead to the desired additional phase shift between neighbouring antennas. That can be seen by a detailed analysis of the response of a single antenna near its resonance.

For simplicity, let us picture the antenna as a point dipole  $\mathbf{p}$  driven by an external electromagnetic field  $\mathbf{E}_{\text{ext}}(t)$ . The dipole is characterized by its natural frequency  $\omega_0$  and a damping constant  $\gamma$  accounting for both the internal and the radiation losses. Assuming the external field varies harmonically in time with a frequency  $\omega$ , the equation of motion for the electric dipole reads

$$\frac{\partial^2}{\partial t^2} \mathbf{p}(t) + \gamma \frac{\partial}{\partial t} \mathbf{p}(t) + \omega_0^2 \mathbf{p}(t) = \alpha_0 \omega_0^2 \mathbf{E}_{\text{ext}} e^{-i\omega t}, \quad (4.10)$$

where  $\alpha_0$  denotes the static polarizability of the dipole. Apparently, shortly after the turning on of the external field, the natural oscillations of the system will die out due to the damping and the dipole will adopt the time dependence of the driving force  $\mathbf{p}(t) = \mathbf{p} e^{-i\omega t}$ . Inserting this expression back into Equation (4.10), one acquires the frequency-dependent relation between the induced dipole moment and the external electric field

$$\mathbf{p} = \frac{\alpha_0 \omega_0^2}{\omega_0^2 - \omega^2 - i\omega\gamma} \mathbf{E}_{\text{ext}}. \quad (4.11)$$

Regarding the experimental design outlined above, we are interested mainly in the phase shift  $\Phi$  of the dipole with respect to the driving electromagnetic force

$$\cos \Phi = \frac{\text{Re} \{ \mathbf{p} \}}{|\mathbf{p}|} = \frac{\omega_0^2 - \omega^2}{\left[ (\omega_0^2 - \omega^2)^2 + \omega^2 \gamma^2 \right]^{\frac{1}{2}}} \quad (4.12)$$

#### 4. PROPOSED EXPERIMENTAL SETUP: MOTIVATION

In Figure 4.3, the phase shift  $\Phi$  (dashed line) as a function of the frequency  $\omega$  is plotted for two close values of the natural frequency  $\omega_0^+ = \omega_0$  and  $\omega_0^- = 0.95\omega_0$ . Clearly, by shifting slightly the resonance frequency, one can tune the phase of the dipole without a dramatic drop in its amplitude (solid line). The following chapters concern with the answer to the question, whether electrostatically doped graphene is capable to induce such shifts in the resonant frequencies of the antennas.

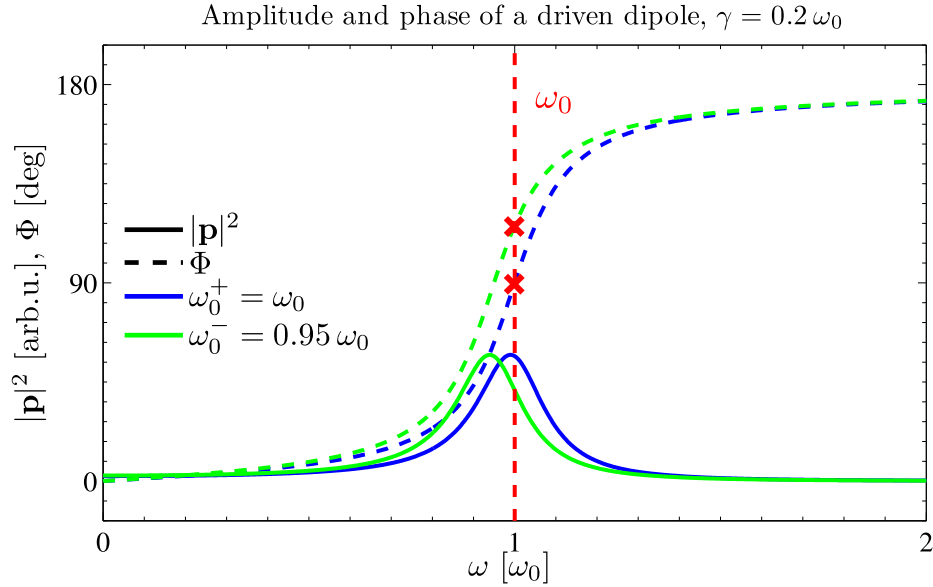


Figure 4.3: The amplitude (solid line) and phase (dashed line) of a driven electric dipole as a function of the frequency of the external field. The dependence is plotted for two different natural frequencies of the dipole  $\omega_0^+ = \omega_0$  and  $\omega_0^- = 0.95\omega_0$ .



## 5. Calculations based on the transformation optics method

The core of this thesis resides in the calculations of the scattering properties of hybrid devices, in which graphene is used as an active element to control the response of surrounding plasmonic structures. In order to perform such calculations, one needs a suitable method, which would be able to cope with the 2D character of graphene and which would provide correct results in a broad range of frequencies (from visible to IR).

It is possible to employ standard techniques like the FDTD (finite differences in the time-domain) or the FEM (finite element method), but those methods usually suffer from large computation times and considerable memory requirements for calculations in the IR. It is associated with the requirement that the dimensions of the simulation region should be at least twice the wavelength of the incident wave so that the evanescent components of the fields in the vicinity of the plasmonic structures do not overlap with the PML (perfectly matched layers) regions, which prevent the propagating waves scattered by the structures from being reflected back at the boundaries of the simulation region.

Instead, a different semi-analytical technique based on spatial transformations has been utilized. It enables to investigate the many possible configurations of parameters like the Fermi energy, the angle of incidence of the illuminating plane wave or the size of the plasmonic structures, all within a reasonable amount of time. This method has, however, two important disadvantages. The first one is the very limited set of geometries, to which it can be applied. The latter resides in the fact that it neglects the retardation effects, which become prominent for large metallic structures in the IR part of the spectrum. Nevertheless, the transformation optics method can be a powerful tool to estimate the strength of the interaction between graphene and a single plasmonic antenna.

### 5.1. Conformal transformations

First let us introduce the mathematical concept standing behind this technique. As mentioned above, the retardation effects shall be neglected so that the electric field is fully described by an electrostatic potential  $V(\mathbf{r}, t)$  (static only in the sense that it satisfies the Poisson's equation known from electrostatics, there are no restrictions on the time dependence of the fields). Furthermore, we shall restrict ourselves to two-dimensional problems, for which the algebra is considerably simpler and the electromagnetic calculations less computationally demanding. Hence, the 2D Poisson's equation for the potential  $V(x, y)$  reads

$$\nabla^2 V(x, y) = \left( \frac{\partial^2}{\partial x^2} + \frac{\partial^2}{\partial y^2} \right) V(x, y) = -\frac{\rho_{\text{ext}}(x, y)}{\varepsilon_0 \varepsilon}, \quad (5.1)$$

where  $x, y$  are the spatial coordinates,  $\varepsilon$  denotes the permittivity of the medium and  $\rho_{\text{ext}}(x, y)$  stands for the external charge density. Importantly, the two-dimensional space can be viewed as a complex plane, where each point is described only through a single coordinate  $z = x + iy$ . Adopting such notation, the partial derivatives from Equation (5.1) become

$$\begin{aligned} \frac{\partial}{\partial x} &= \frac{\partial}{\partial z} \frac{\partial z}{\partial x} + \frac{\partial}{\partial z^*} \frac{\partial z^*}{\partial x} = \frac{\partial}{\partial z} + \frac{\partial}{\partial z^*}, & \frac{\partial}{\partial y} &= \frac{\partial}{\partial z} \frac{\partial z}{\partial y} + \frac{\partial}{\partial z^*} \frac{\partial z^*}{\partial y} = i \frac{\partial}{\partial z} - i \frac{\partial}{\partial z^*}, \\ \nabla^2 &= \frac{\partial^2}{\partial x^2} + \frac{\partial^2}{\partial y^2} = \left( \frac{\partial}{\partial x} + i \frac{\partial}{\partial y} \right) \left( \frac{\partial}{\partial x} - i \frac{\partial}{\partial y} \right) = 4 \frac{\partial^2}{\partial z \partial z^*}, \end{aligned} \quad (5.2)$$

where  $z^* = x - iy$  represents the complex conjugate to  $z$ . Let us introduce a spatial transformation  $w(z) = x' + iy'$  with yet unspecified properties and express the operator  $\nabla^2$  in these new coordinates

## 5.2. GEOMETRY OF THE PROBLEM

$$\begin{aligned}\nabla^2 &= 4 \frac{\partial^2}{\partial z \partial z^*} = \left( \frac{\partial}{\partial w} \frac{\partial w}{\partial z} + \frac{\partial}{\partial w^*} \frac{\partial w^*}{\partial z} \right) \left( \frac{\partial}{\partial w} \frac{\partial w}{\partial z^*} + \frac{\partial}{\partial w^*} \frac{\partial w^*}{\partial z^*} \right) = \\ &= 4 \left( \frac{\partial^2}{\partial w^2} \frac{\partial w}{\partial z} \frac{\partial w}{\partial z^*} + \frac{\partial^2}{\partial w \partial w^*} \frac{\partial w^*}{\partial z} \frac{\partial w}{\partial z^*} + \frac{\partial^2}{\partial w \partial w^*} \frac{\partial w}{\partial z} \frac{\partial w^*}{\partial z^*} + \frac{\partial^2}{\partial w^{*2}} \frac{\partial w^*}{\partial z} \frac{\partial w}{\partial z^*} \right).\end{aligned}\quad (5.3)$$

Apparently, the transformation will not generally preserve the simple form of the above operator in the original cartesian coordinates, unless some assumptions regarding its properties are made. It would seem that the above equation will reduce to a more appealing form, if one of the two following conditions is satisfied

$$\frac{\partial w}{\partial z^*} = 0 \quad \Rightarrow \quad \nabla^2 = 4 \frac{\partial^2}{\partial w \partial w^*} \left| \frac{\partial w}{\partial z} \right|^2, \quad (5.4)$$

$$\frac{\partial w}{\partial z} = 0 \quad \Rightarrow \quad \nabla^2 = 4 \frac{\partial^2}{\partial w \partial w^*} \left| \frac{\partial w}{\partial z^*} \right|^2. \quad (5.5)$$

The first condition indicates that the function  $w(z)$  is, in the language of the complex analysis, holomorphic, whereas the latter is satisfied by anti-holomorphic functions. Importantly, spatial transformations prescribed by such functions preserve, apart from a scaling factor, the form of the Poisson's equation, which means that a solution to that equation in one space is automatically a valid solution to the same equation in the transformed space. That makes them a powerful tool, since one can work out otherwise unsolvable problems by switching to a space, where the geometry of the problem assumes a more convenient form and in which the solution can be, therefore, analytically calculated.

To conclude this section, the transformations, for which  $w(z)$  is holomorphic or anti-holomorphic, generally preserve angles between any two curves and they are denoted as conformal transformations.

## 5.2. Geometry of the problem

Aubry et al. [5] studied in their paper the light scattering from two touching infinitely long metallic cylinders as depicted in Figure 5.1 (a). They employed the following conformal transformation to convert the problem of the touching cylinders illuminated by a plane wave (in fact the plane wave is replaced by a uniform electric field) into a diametrically different problem of an electric line dipole trapped inside a multilayer structure (Figure 5.1 (b))

$$\eta(w) = \frac{g^2}{w^*}, \quad (5.6)$$

where  $w = x + iz$ , resp.  $\eta = \xi + i\zeta$  are the coordinates in the original, resp. the transformed space and  $g^2$  is a scaling factor.

Evidently, by varying the thickness of the intermediate layer in the the transformed space one controls the radii of the cylinders, more precisely  $R_a = \frac{g^2}{2a}$  and  $R_b = \frac{g^2}{2b}$ , where  $a$  and  $b$  characterize the thickness of the intermediate layer (see Figure 5.1 (b)).

Importantly, the above procedure can be useful for the estimation of the strength of the interaction between graphene and ordinary plasmonic structures, although some modifications to the presented geometry has to be introduced. If one substitutes the lower halfspace in the multilayer structure by a dielectric material with a graphene sheet on the top, then takes the limit  $b \rightarrow 0$  and finally performs the aforementioned transformation, the two touching metallic cylinders will be replaced with a single cylinder lying on the top of a dielectric substrate covered by a graphene sheet as illustrated in Figure 5.2.

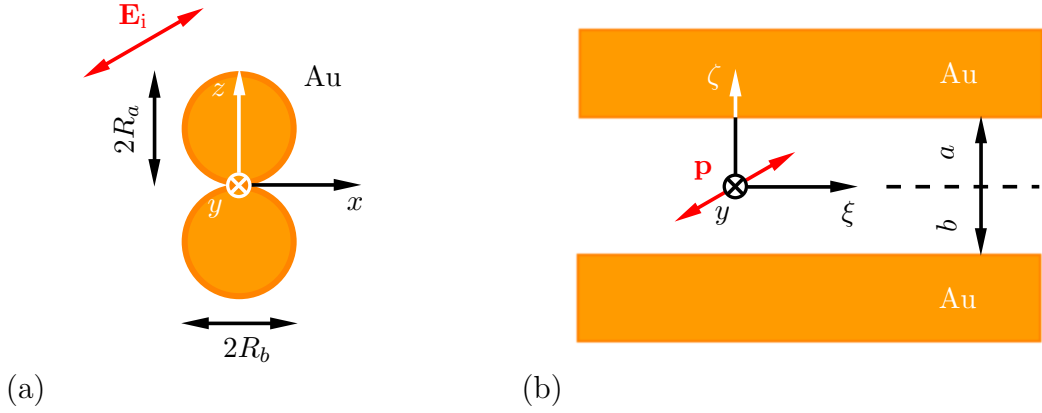


Figure 5.1: (a) Schematic drawing of two touching metallic cylinders with radii  $R_a$  and  $R_b$  inside a uniform electric field  $\mathbf{E}_i$ . (b) Employing the conformal transformation given by Equation (5.6), the geometry from (a) is converted into a multilayer structure with a dipolar source  $\mathbf{p}$ .

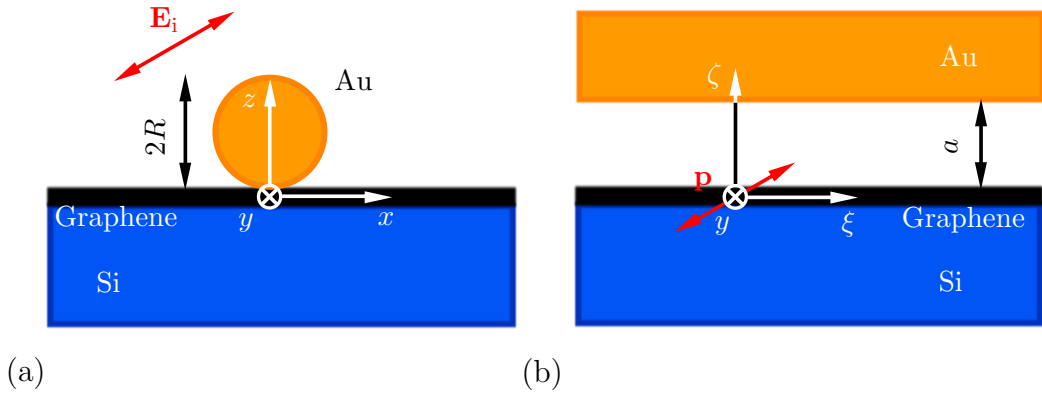


Figure 5.2: (a) Schematic drawing of the geometry suitable for the purposes of this thesis. A single metallic cylinder of radius  $R$  placed on the top of a silicon substrate covered by a graphene sheet and illuminated by a plane wave  $\mathbf{E}_i$  can be transformed into a multilayer structure with a dipolar source  $\mathbf{p}$  (b).

### 5.3. Potentials

Before we proceed with the calculation of the distribution of the electrostatic potential  $V(\xi, \zeta)$  within the multilayer structure, it is necessary to clarify, how the potential of an electric line dipole is transformed into a uniform electric field. The electrostatic potential of a unit line charge  $V_e(\xi, \zeta)$  inside a medium with permittivity  $\varepsilon$  is easily acquired from the Gauss's law of electromagnetism

$$V_e(\xi, \zeta) = -\frac{e}{2\pi\varepsilon_0\varepsilon} \ln\left(\sqrt{\xi^2 + \zeta^2}\right). \quad (5.7)$$

An electric dipole consists of two charges of the same magnitude but the opposite polarity, mutually shifted by a small vector  $\mathbf{\Delta} = (\Delta_\xi, \Delta_\zeta)$

### 5.3. POTENTIALS

$$\begin{aligned}
V_{\text{dip}}(\xi, \zeta) &= -\frac{e}{2\pi\epsilon_0\epsilon} \ln \left[ \sqrt{\left(\xi - \frac{\Delta_\xi}{2}\right)^2 + \left(\zeta - \frac{\Delta_\zeta}{2}\right)^2} \right] + \frac{e}{2\pi\epsilon_0\epsilon} \ln \left[ \sqrt{\left(\xi + \frac{\Delta_\xi}{2}\right)^2 + \left(\zeta + \frac{\Delta_\zeta}{2}\right)^2} \right] \approx \\
&\approx \frac{e}{2\pi\epsilon_0\epsilon} \nabla \ln \left( \sqrt{\xi^2 + \zeta^2} \right) \cdot \mathbf{\Delta} = \frac{e}{2\pi\epsilon_0\epsilon} \frac{\xi\Delta_\xi + \zeta\Delta_\zeta}{\xi^2 + \zeta^2}, \tag{5.8}
\end{aligned}$$

where the assumption  $|\mathbf{\Delta}| \ll \sqrt{\xi^2 + \zeta^2}$  has been made. Recalling that  $\xi$  and  $\zeta$  can be expressed using a single complex plane coordinate  $\eta = \xi + i\zeta$  and employing the conformal transformation  $w(\eta) = x + iz$  prescribed by Equation (5.6), one obtains

$$\begin{aligned}
V_{\text{dip}}(\xi, \zeta) &= \frac{e}{2\pi\epsilon_0\epsilon} \frac{\xi\Delta_\xi + \zeta\Delta_\zeta}{\xi^2 + \zeta^2} = \frac{e}{2\pi\epsilon_0\epsilon} \left[ \left( \frac{\eta + \eta^*}{\eta\eta^*} \right) \Delta_\xi + \left( \frac{\eta - \eta^*}{i\eta\eta^*} \right) \Delta_\zeta \right] = \\
&= \frac{e}{2\pi\epsilon_0\epsilon} \left[ \left( \frac{1}{\eta} + \frac{1}{\eta^*} \right) \Delta_\xi + \left( \frac{1}{i\eta} - \frac{1}{i\eta^*} \right) \Delta_\zeta \right] = \frac{e}{2\pi\epsilon_0\epsilon g^2} \left[ (w + w^*) \Delta_\xi + (w - w^*) \frac{\Delta_\zeta}{i} \right] = \\
&= \frac{e}{2\pi\epsilon_0\epsilon g^2} (x\Delta_\xi + z\Delta_\zeta) = V(x, z) \tag{5.9}
\end{aligned}$$

Clearly, the field of the line dipole corresponds after the transformation to a uniform electric field  $\mathbf{E}$  with a polarization in the direction of the original dipole

$$\mathbf{E}(x, z) = -\nabla V(x, z) = -\frac{e}{2\pi\epsilon_0\epsilon g^2} \mathbf{\Delta}. \tag{5.10}$$

Having the relation linking the strength of the dipole  $\mathbf{p} = e\mathbf{\Delta}$  to the intensity of the uniform electric field  $\mathbf{E}$  in the transformed space, we have everything prepared for the calculation of the distribution of the potential  $V(\xi, \zeta)$  within the multilayer structure in the presence of an electric line dipole. The procedure for solving problems with a planar geometry resides in decomposing the potentials in the individual regions into their Fourier spectra

$$V(\xi, \zeta) = \int_{-\infty}^{\infty} \frac{dq}{2\pi} e^{iq\xi} V(q, \zeta) \tag{5.11}$$

and then demanding that each Fourier component  $V(q, \zeta)$  satisfies the customary boundary conditions at the interfaces between the different media.

First let us consider a region without external charges, in which the Poisson's equation for the electrostatic potential reduces to the homogenous Laplace's equation

$$\nabla^2 V(\xi, \zeta) = \nabla^2 \int_{-\infty}^{\infty} \frac{dq}{2\pi} e^{iq\xi} V(q, \zeta) = \int_{-\infty}^{\infty} \frac{dq}{2\pi} e^{iq\xi} \left[ -q^2 V(q, \zeta) + \frac{\partial^2}{\partial \zeta^2} V(q, \zeta) \right] = 0. \tag{5.12}$$

The above equation is fulfilled only if the term in the square brackets is identically equal to zero for all the wavevectors  $q$ . The resulting equation for the Fourier components  $V(q, \zeta)$  is then standardly solved by assuming an exponential dependence of the potential on the spatial coordinate  $\zeta$

$$V(q, \zeta) = V(q) e^{\lambda\zeta} \quad \Rightarrow \quad -q^2 V(q) e^{\lambda\zeta} + \lambda^2 e^{\lambda\zeta} = 0 \quad \Rightarrow \quad \lambda = \pm|q|.$$

Evidently, there exist two solutions for the potential  $V(q, \zeta)$  corresponding to  $\lambda = \pm|q|$  and the general solution is given by their linear combination

$$V(q, \zeta) = A(q) e^{|q|\zeta} + B(q) e^{-|q|\zeta}, \tag{5.13}$$

## 5. CALCULATIONS BASED ON THE TRANSFORMATION OPTICS METHOD

where  $A(q)$ ,  $B(q)$  are arbitrary coefficients.

The procedure for obtaining the general solution for the inhomogenous Poisson's equation is considerably less straightforward. The starting point is again the decomposition of both the potential  $V(\xi, \zeta)$  and the external charge density  $\rho_{\text{ext}}(\xi, \zeta)$  into their Fourier spectra

$$\nabla^2 \int_{-\infty}^{\infty} \frac{dq}{2\pi} e^{iq\xi} V(q, \zeta) = - \int_{-\infty}^{\infty} \frac{dq}{2\pi} e^{iq\xi} \frac{\rho_{\text{ext}}(q, \zeta)}{\varepsilon_0 \varepsilon}, \quad (5.14)$$

$$\int_{-\infty}^{\infty} \frac{dq}{2\pi} e^{iq\xi} \left[ -q^2 V(q, \zeta) + \frac{\partial^2}{\partial \zeta^2} V(q, \zeta) + \frac{\rho_{\text{ext}}(q, \zeta)}{\varepsilon_0 \varepsilon} \right] = 0. \quad (5.15)$$

which is satisfied only if the expression in the square brackets is equal to zero. It will prove itself useful to rewrite the external charge density by means of the Dirac distribution function  $\delta(\zeta)$

$$\rho_{\text{ext}}(q, \zeta) = \int_{-\infty}^{\infty} d\zeta' \delta(\zeta - \zeta') \rho_{\text{ext}}(q, \zeta'). \quad (5.16)$$

The next step is to express  $V(q, \zeta)$  in terms of its Fourier components with respect to the coordinate  $\zeta$

$$\left( -q^2 + \frac{\partial^2}{\partial \zeta^2} \right) \int_{-\infty}^{\infty} \frac{dq}{2\pi} e^{ip\zeta} V(q, p) = \int_{-\infty}^{\infty} d\zeta' \delta(\zeta - \zeta') \frac{\rho_{\text{ext}}(q, \zeta')}{\varepsilon_0 \varepsilon} \quad (5.17)$$

$$- \int_{-\infty}^{\infty} \frac{dp}{2\pi} e^{ip\zeta} (q^2 + p^2) V(q, p) = \int_{-\infty}^{\infty} d\zeta' \delta(\zeta - \zeta') \frac{\rho_{\text{ext}}(q, \zeta')}{\varepsilon_0 \varepsilon}. \quad (5.18)$$

Recalling that

$$\delta(\zeta - \zeta') = \int_{-\infty}^{\infty} \frac{dp}{2\pi} e^{ip(\zeta - \zeta')}, \quad (5.19)$$

the preceding equation becomes

$$\int_{-\infty}^{\infty} \frac{dp}{2\pi} e^{ip\zeta} \left[ (q^2 + p^2) V(q, p) - \int_{-\infty}^{\infty} d\zeta' e^{-ip\zeta'} \frac{\rho_{\text{ext}}(q, \zeta')}{\varepsilon_0 \varepsilon} \right] = 0. \quad (5.20)$$

Once again, the equation is fulfilled only if the expression in the square brackets is identically equal to zero for each  $p$ , hence

$$V(q, p) = \int_{-\infty}^{\infty} d\zeta' e^{-ip\zeta'} \frac{\rho_{\text{ext}}(q, \zeta')}{\varepsilon_0 \varepsilon (q^2 + p^2)}. \quad (5.21)$$

Eventually, the Fourier components of the electrostatical potential  $V(q, \zeta)$  are acquired by the inverse Fourier transform

$$V(q, \zeta) = \int_{-\infty}^{\infty} \frac{dp}{2\pi} e^{ip\zeta} \int_{-\infty}^{\infty} d\zeta' e^{-ip\zeta'} \frac{\rho_{\text{ext}}(q, \zeta')}{\varepsilon_0 \varepsilon (q^2 + p^2)} = \int_{-\infty}^{\infty} d\zeta' \frac{\rho_{\text{ext}}(q, \zeta')}{2\pi \varepsilon_0 \varepsilon} \int_{-\infty}^{\infty} dp \frac{e^{ip(\zeta - \zeta')}}{q^2 + p^2}. \quad (5.22)$$

### 5.3. POTENTIALS

The value of the resulting integral over  $p$  can be found in tables (Gradshteyn [14], p. 342)

$$\int_{-\infty}^{\infty} dp \frac{e^{ip(\zeta-\zeta')}}{q^2 + p^2} = \frac{\pi}{|q|} e^{-|q||\zeta-\zeta'|}. \quad (5.23)$$

Inserting this expression into the previous equation, one finally obtains the desired distribution of the electrostatic potential in the presence of an external charge density

$$V(q, \zeta) = \int_{-\infty}^{\infty} d\zeta' \frac{\rho_{\text{ext}}(q, \zeta')}{2|q|\varepsilon_0\varepsilon} e^{-|q||\zeta-\zeta'|}. \quad (5.24)$$

At this point, it might be beneficial to summarize the results of the above calculations and outline the path we shall further follow. Utilizing the apparatus of the Fourier analysis, general expressions for the electrostatic potential in regions with a planar geometry have been derived. Both the homogenous solution (Eq. (5.13)) and the solution in the presence of external charges (Eq. (5.24)) have been presented. All that now remains to do is to calculate the Fourier components of the potential of an electric line dipole by means of the formula given by Equation (5.24) and then find the solution for the multilayer structure depicted in Figure 5.2 (b) by applying the customary boundary conditions at the interfaces between the different regions.

As mentioned earlier, the charge density of a an electric line dipole corresponds to two line charges of the same magnitude, but the opposite polarity mutually shifted by a small vector  $\mathbf{\Delta} = (\Delta_\xi, \Delta_\zeta)$ . In terms of the Dirac delta functions

$$\rho_{\text{ext}}(\xi, \zeta) = e \delta\left(\xi - \frac{\Delta_\xi}{2}\right) \delta\left(\zeta - \frac{\Delta_\zeta}{2}\right) - e \delta\left(\xi + \frac{\Delta_\xi}{2}\right) \delta\left(\zeta + \frac{\Delta_\zeta}{2}\right), \quad (5.25)$$

where the center of the dipole is assumed to be at the origin of the coordinate system. The Fourier components are easily obtained through the Fourier transform with respect to  $\xi$

$$\rho_{\text{ext}}(q, \zeta) = \int_{-\infty}^{\infty} d\xi e^{-iq\xi} \rho_{\text{ext}}(\xi, \zeta) = e \left[ e^{-iq\frac{\Delta_\xi}{2}} \delta\left(\zeta - \frac{\Delta_\zeta}{2}\right) - e^{iq\frac{\Delta_\xi}{2}} \delta\left(\zeta + \frac{\Delta_\zeta}{2}\right) \right]. \quad (5.26)$$

Employing the formula given by Equation (5.24), the potential of the electric line dipole  $V_{\text{dip}}(q, \zeta)$  in terms of its Fourier components is acquired

$$V_{\text{dip}}(q, \zeta) = \int_{-\infty}^{\infty} d\zeta' \frac{\rho_{\text{ext}}(q, \zeta')}{2|q|\varepsilon_0\varepsilon} e^{-|q||\zeta-\zeta'|} = \frac{e}{2|q|\varepsilon_0\varepsilon} \left[ e^{-iq\frac{\Delta_\xi}{2}} e^{-|q|\left|\zeta-\frac{\Delta_\zeta}{2}\right|} - e^{iq\frac{\Delta_\xi}{2}} e^{-|q|\left|\zeta+\frac{\Delta_\zeta}{2}\right|} \right] \quad (5.27)$$

Although there is no particular reason for not using the above expression for further calculations, we shall approximate it with a more lucid and compact form by replacing the exponential factors with their Taylor's expansions. Assuming both  $q\Delta_\xi \ll 1$ ,  $q\Delta_\zeta \ll 1$  and  $\Delta_\xi \ll \xi$ ,  $\Delta_\zeta \ll \zeta$ , the previous equation becomes

$$\begin{aligned} V_{\text{dip}}(q, \zeta) &\approx \frac{e e^{-|q||\zeta|}}{2|q|\varepsilon_0\varepsilon} \left[ \left(1 - iq\frac{\Delta_\xi}{2}\right) \left(1 + \text{sgn}(\zeta) |q| \frac{\Delta_\zeta}{2}\right) - \left(1 + iq\frac{\Delta_\xi}{2}\right) \left(1 - \text{sgn}(\zeta) |q| \frac{\Delta_\zeta}{2}\right) \right] = \\ &= \frac{e e^{-|q||\zeta|}}{2|q|\varepsilon_0\varepsilon} [-iq\Delta_\xi + |q|\Delta_\zeta \text{sgn}(\zeta)], \end{aligned} \quad (5.28)$$

## 5. CALCULATIONS BASED ON THE TRANSFORMATION OPTICS METHOD

where  $\text{sgn}(\zeta)$  denotes the signum function defined as

$$\text{sgn}(\zeta) = \begin{cases} -1 & \text{if } \zeta < 0 \\ 1 & \text{if } \zeta \geq 0 \end{cases}. \quad (5.29)$$

The fact that Equation (5.28) truly represents the correct Fourier spectrum of the potential of an electric line dipole can be verified using the inverse Fourier transform

$$V_{\text{dip}}(\xi, \zeta) = \int_{-\infty}^{\infty} \frac{dq}{2\pi} e^{iq\xi} V_{\text{dip}}(q, \zeta) = \int_{-\infty}^{\infty} \frac{dq}{2\pi} \left[ \underbrace{\cos(q\xi)}_{\text{even}} + i \underbrace{\sin(q\xi)}_{\text{odd}} \right] \underbrace{\frac{e e^{-|q|\zeta}}{2|q|\varepsilon_0\varepsilon}}_{\text{even}} \left[ \underbrace{-i q \Delta_\xi}_{\text{odd}} + \underbrace{|q| \Delta_\zeta \text{sgn}(\zeta)}_{\text{even}} \right]. \quad (5.30)$$

Apparently, only those terms in the integrand, which are even in  $q$ , shall give a nonzero value after the integration, hence

$$V_{\text{dip}}(\xi, \zeta) = \int_0^{\infty} dq \frac{e e^{-q|\zeta|}}{4\pi\varepsilon_0\varepsilon} [2 \sin(q\xi) \Delta_\xi + 2 \cos(q\xi) \Delta_\zeta \text{sgn}(\zeta)]. \quad (5.31)$$

The values of the resulting integrals over  $q$  can be found in tables (Gradshteyn [14], p. 486)

$$\int_0^{\infty} dq e^{-q|\zeta|} \sin(q\xi) = \frac{\xi}{\xi^2 + \zeta^2}, \quad \int_0^{\infty} dq e^{-q|\zeta|} \cos(q\xi) = \frac{|\zeta|}{\xi^2 + \zeta^2}. \quad (5.32)$$

Finally, inserting these expressions into the previous equation and recalling that  $|\zeta| \text{sgn}(\zeta) = \zeta$ , the potential from Equation (5.8) is recovered

$$V_{\text{dip}}(\xi, \zeta) = \frac{e}{2\pi\varepsilon_0\varepsilon} \frac{\xi \Delta_\xi + \zeta \Delta_\zeta}{\xi^2 + \zeta^2}. \quad (5.33)$$

The next step resides in matching the solutions in individual regions by applying the customary boundary conditions at the respective interfaces. As illustrated in Figure 5.3, the multilayer structure consists of three regions, each characterized by a possibly different dielectric function  $\varepsilon_i$ . The dipolar source  $\mathbf{p} = e \mathbf{\Delta}$  is situated at the origin of the coordinate system  $\xi, \zeta$  and the bottom interface practically coincides with the  $\xi$ -axis.

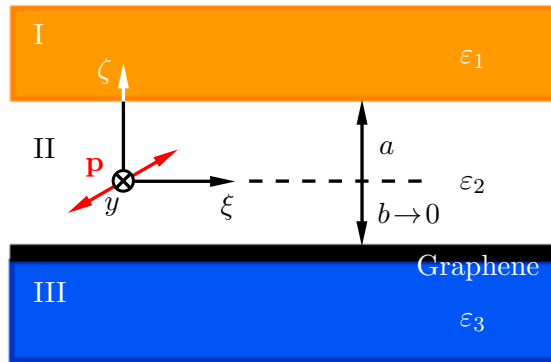


Figure 5.3: Schematic drawing of the considered multilayer structure. The space is divided into three distinct regions characterized by frequency-dependent dielectric functions  $\varepsilon_i$ , where  $i = 1, 2, 3$ . The bottom interface containing the graphene sheet is set to  $\zeta = 0$  and the dipolar source  $\mathbf{p}$  is positioned at the origin of the coordinate system.

### 5.3. POTENTIALS

First let us write down the solutions for the electrostatic potential in the individual regions

$$\text{Region I: } V_{\text{tot}}^{\text{I}}(\xi, \zeta) = \int_{-\infty}^{\infty} \frac{dq}{2\pi} e^{iq\xi} \left[ A_1(q) e^{|q|\zeta} + B_1(q) e^{-|q|\zeta} \right], \quad (5.34)$$

$$\text{Region II: } V_{\text{ind}}^{\text{II}}(\xi, \zeta) = \int_{-\infty}^{\infty} \frac{dq}{2\pi} e^{iq\xi} \left[ A_2(q) e^{|q|\zeta} + B_2(q) e^{-|q|\zeta} \right], \quad (5.35)$$

$$V_{\text{ext}}^{\text{II}}(\xi, \zeta) = \int_{-\infty}^{\infty} \frac{dq}{2\pi} e^{iq\xi} \frac{e e^{-|q||\zeta|}}{2|q|\varepsilon_0\varepsilon} [-iq\Delta_\xi + |q|\Delta_\zeta \text{sgn}(\zeta)] = \int_{-\infty}^{\infty} \frac{dq}{2\pi} e^{iq\xi} A_0(q) e^{-|q||\zeta|}, \quad (5.36)$$

$$\text{Region III: } V_{\text{tot}}^{\text{III}}(\xi, \zeta) = \int_{-\infty}^{\infty} \frac{dq}{2\pi} e^{iq\xi} \left[ A_3(q) e^{|q|\zeta} + B_3(q) e^{-|q|\zeta} \right], \quad (5.37)$$

where the total potential  $V_{\text{tot}}$  is the sum of the induced and external potentials  $V_{\text{tot}} = V_{\text{ind}} + V_{\text{ext}}$ .

Above all, we require that the electromagnetic fields should reach finite values, when one approaches infinity  $\zeta \rightarrow \pm\infty$ , thus the coefficients  $B_1(q)$  and  $A_3(q)$  has to be equal to zero. Furthermore, the electrostatic potential should be continuous when crossing the boundaries of the regions. The last condition prescribes that the discontinuity in the normal components of the electric displacement  $\varepsilon_0\varepsilon_i\mathbf{E}_i^\perp$  at the interfaces has to be equal to the accumulated surface charge. Combining all these requirements, one obtains a system of four linear equations for the four unknown coefficients  $A_1(q)$ ,  $B_2(q)$ ,  $A_2(q)$  and  $B_3(q)$

$$\zeta = a: \quad A_1 e^{-|q|a} = A_0 e^{-|q|a} + A_2 e^{-|q|a} + B_2 e^{|q|a}, \quad (5.38)$$

$$-A_1 \varepsilon_1 e^{-|q|b} = -A_0 \varepsilon_2 e^{-|q|b} - A_2 \varepsilon_2 e^{-|q|b} + B_2 \varepsilon_2 e^{|q|b}, \quad (5.39)$$

$$\zeta = -b: \quad B_3 e^{-|q|b} = A_0 e^{-|q|b} + A_2 e^{|q|b} + B_2 e^{-|q|b}, \quad (5.40)$$

$$B_3 \varepsilon_3 e^{-|q|b} - \frac{\sigma_S(q)}{\varepsilon_0 |q|} = A_0 \varepsilon_2 e^{-|q|b} - A_2 \varepsilon_2 e^{|q|b} + B_2 \varepsilon_2 e^{-|q|b}, \quad (5.41)$$

Notice that graphene enters the system through the Fourier components of the surface charge  $\sigma_S(q)$  induced at the lower interface of the multilayer structure

$$\begin{aligned} \sigma_S(\xi) &= -\nabla \cdot \mathbf{P} = -\varepsilon_0 \chi_{2\text{D}}^\tau(\omega) \nabla \cdot \mathbf{E}^\parallel(\xi, -b) = i \frac{\sigma(\omega)}{\omega} \nabla \cdot \nabla^\parallel \int_{-\infty}^{\infty} \frac{dq}{2\pi} e^{iq\xi} V_{\text{tot}}^{\text{III}}(q, \zeta) \Big|_{\zeta=-b} = \\ &= i \frac{\sigma(\omega)}{\omega} \nabla \cdot \nabla^\parallel \int_{-\infty}^{\infty} \frac{dq}{2\pi} e^{iq\xi} B_3(q) e^{|q|\zeta} \Big|_{\zeta=-b} = \int_{-\infty}^{\infty} \frac{dq}{2\pi} e^{iq\xi} \left[ -i \frac{q^2 \sigma(\omega)}{\omega} B_3(q) e^{-|q|b} \right] = \\ &= \int_{-\infty}^{\infty} \frac{dq}{2\pi} e^{iq\xi} \sigma_S(q), \end{aligned} \quad (5.42)$$

where the label  $\parallel$  emphasizes that only the vector component parallel to the interface is taken into account. The dynamical susceptibility  $\chi_{2\text{D}}^\tau(\omega)$  and the conductivity  $\sigma(\omega)$  of graphene have been introduced in Chapter 1.

## 5. CALCULATIONS BASED ON THE TRANSFORMATION OPTICS METHOD

Inserting the above expression for the induced surface charge density into Equation (5.41), the system of the four linear equations can be after few rearrangments written in the following matrix form

$$\begin{pmatrix} 1 & -1 & e^{2|q|a} & 0 \\ \frac{\epsilon_1}{\epsilon_2} & -1 & e^{2|q|a} & 0 \\ 0 & -e^{2|q|b} & -1 & 1 \\ 0 & e^{2|q|b} & -1 & \frac{\epsilon_3}{\epsilon_2} + i \frac{|q|\sigma(\omega)}{\epsilon_0\epsilon_2\omega} \end{pmatrix} \begin{pmatrix} A_1 \\ B_2 \\ A_2 \\ B_3 \end{pmatrix} = \begin{pmatrix} A_0 \\ A_0 \\ A_0 \\ A_0 \end{pmatrix}. \quad (5.43)$$

Such matrix equation can be solved either by hand or with use of a suitable mathematical software. Taking the  $b \rightarrow 0$  limit and adopting the following notation  $\frac{\epsilon_1}{\epsilon_2} = \epsilon$ ,  $\frac{\epsilon_3}{\epsilon_2} + i \frac{|q|\sigma(\omega)}{\epsilon_0\epsilon_2\omega} = \delta$ ,  $e^{-2|q|a} = \gamma$ , the coefficients  $A_1(q)$ ,  $B_2(q)$ ,  $A_2(q)$ ,  $B_3(q)$  are found to be

$$A_1(q) = \frac{4A_0(q)}{(1 + \epsilon)(1 + \delta) - \gamma(1 - \epsilon)(1 - \delta)}, \quad (5.44)$$

$$A_2(q) = \frac{A_0(q)(1 - \delta)[(1 + \epsilon + \gamma(1 - \epsilon))]}{(1 + \epsilon)(1 + \delta) - \gamma(1 - \epsilon)(1 - \delta)}, \quad (5.45)$$

$$B_2(q) = \frac{2A_0(q)\gamma(1 - \epsilon)}{(1 + \epsilon)(1 + \delta) - \gamma(1 - \epsilon)(1 - \delta)}, \quad (5.46)$$

$$B_3(q) = \frac{2A_0(q)[(1 + \epsilon + \gamma(1 - \epsilon))]}{(1 + \epsilon)(1 + \delta) - \gamma(1 - \epsilon)(1 - \delta)}. \quad (5.47)$$

Nothing hinders us now from inserting the above coefficients back into the expressions for the electrostatic potentials given by Equations (5.34)-(5.37). Evaluating numerically the integrals over  $q$  and employing the conformal transformation prescribed by Equation (5.6), the distribution of the electrostatic potential, resp. the electric field within the metallic cylinder and its vicinity is recovered.

Figure 5.4 shows the profile of the electric field intensity in the neighbourhood of a golden cylinder with a radius  $R = 10$  nm placed on the top of a dielectric substrate covered by a single graphene sheet. The whole structure is illuminated by a plane wave propagating in the  $-z$  direction and the graphene sheet is doped enough to sustain TM surface plasmon modes. Notice that the scale is logarithmic, which would suggest that one can achieve a more than thousandfold field enhancement in graphene using only a small golden cylinder. Evidently, such effect is quite suspicious and requires a detailed investigation.

It turns out that even though the interface between the substrate and the superstrate seems to be perfectly planar, the source (uniform electric field) perceives it as a cylinder with a radius approaching infinity. Thus the above solution does not describe light scattering from a single cylinder lying on a substrate, but rather from two touching cylinders (although with diametrically different diameters). Since the larger cylinder is coated by doped graphene, it sustains localized surface plasmons on its own. The plasmons from both the cylinders tend to converge at their touching point, leading to the light-harvesting phenomenon observed in Figure 5.4 and earlier proposed by Aubry et al. [5].

Importantly, one can get rid of such (for our purposes intrusive) effect by neglecting the direct scattering of the incident plane wave from the larger cylinder and retaining only those terms corresponding to the mutual interaction with the smaller metallic cylinder. The procedure developed by the author of this thesis is based on the concept one can encounter while dealing with waveguides and interferometers.

When a plane wave is propagating inside a thin dielectric slab with parallel planar interfaces, it repetitively undergoes reflections on those interfaces and the total field inside, resp. outside the slab is then calculated as the superposition of all those reflected, resp. transmitted waves. One can straightforwardly extend this concept to the present electrostatic case of a dipolar source trapped inside a multilayer structure. We have already decomposed the potential of the line dipole into plane

### 5.3. POTENTIALS

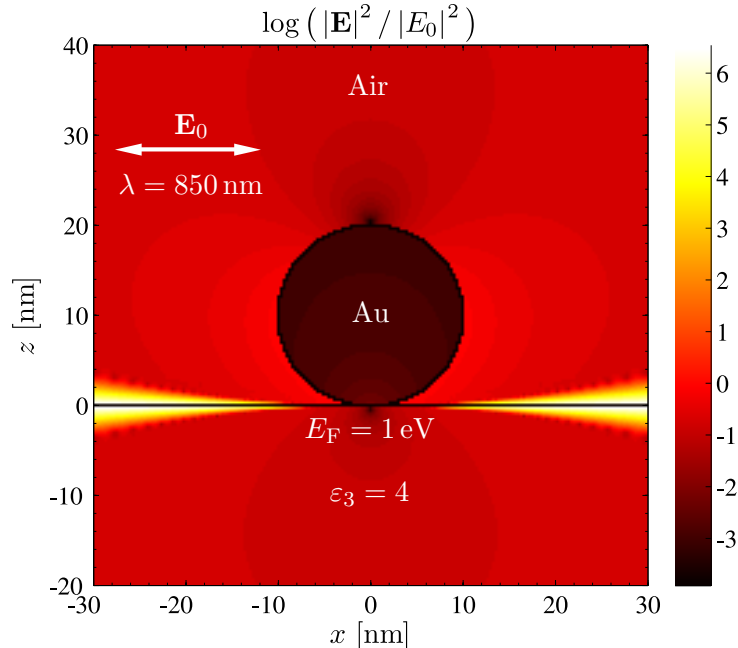


Figure 5.4: Map of the intensity of the electric field in the vicinity of an infinitely long golden cylinder with a radius  $R = 10$  nm lying on the top of a dielectric substrate covered by a graphene sheet. The whole structure is illuminated by an electromagnetic plane wave ( $\lambda = 850$  nm) propagating in the  $-z$  direction. The permittivity of the substrate was set to  $\varepsilon_3 = 4$ , the superstrate is assumed to be air and the graphene sheet is electrostatically doped to  $E_F = 1$  eV with the relaxation time  $\tau = 10^{-13}$  s.

waves (notice that in the electrostatic case they are evanescent), all that now remains to do is to determine the reflection  $r_p$  and transmission  $t_p$  coefficients at the individual interfaces. Apparently, one can obtain them easily from the above set of boundary conditions (Equations (5.38)-(5.41)) by taking the  $b \rightarrow -\infty$  and the  $a \rightarrow \infty$  limits

$$r_p^{21} = \frac{\varepsilon_2 - \varepsilon_1}{\varepsilon_2 + \varepsilon_1}, \quad t_p^{21} = \frac{2\varepsilon_2}{\varepsilon_2 + \varepsilon_1}, \quad (5.48)$$

$$r_p^{23} = \frac{\varepsilon_2 - \varepsilon_3 - i \frac{|q|\sigma(\omega)}{\varepsilon_0\omega}}{\varepsilon_2 + \varepsilon_3 + i \frac{|q|\sigma(\omega)}{\varepsilon_0\omega}}, \quad t_p^{23} = \frac{2\varepsilon_2}{\varepsilon_2 + \varepsilon_3 + i \frac{|q|\sigma(\omega)}{\varepsilon_0\omega}}, \quad (5.49)$$

where the superscript indicates with which interface is the particular coefficient associated.

The last step resides in summing the amplitudes of all the reflected and transmitted waves using the above coefficients  $r_p$  and  $t_p$ , which also appears to be the key moment of the whole derivation. If all the reflections are taken into account, one obtains the same expressions for the coefficients  $A_1(q)$ ,  $A_2(q)$  etc. as before, but if all the waves created as the result of the direct reflection of the source wave from the lower interface are omitted and retained only those reflected for the first time at the upper interface, one shall acquire coefficients, which in the end describe the light scattering from a single metallic cylinder placed on the top of a planar substrate. In mathematical terms

5. CALCULATIONS BASED ON THE TRANSFORMATION OPTICS METHOD

$$\begin{aligned}
V_{\text{tot}}^{\text{II}}(q, \zeta) &= A_0 e^{-|q|\zeta} + A_0 r_{\text{p}}^{21} e^{-|q|a} e^{|q|(\zeta-a)} + A_0 r_{\text{p}}^{21} r_{\text{p}}^{23} e^{-2|q|a} e^{-|q|\zeta} + A_0 (r_{\text{p}}^{21})^2 r_{\text{p}}^{23} e^{-3|q|a} e^{|q|(\zeta-a)} + \dots = \\
&= A_0 e^{-|q|\zeta} + \sum_{n=0}^{\infty} \left( r_{\text{p}}^{21} r_{\text{p}}^{23} e^{-2|q|a} \right)^n A_0 r_{\text{p}}^{21} r_{\text{p}}^{23} e^{-|q|\zeta} + \sum_{n=0}^{\infty} \left( r_{\text{p}}^{21} r_{\text{p}}^{23} e^{-2|q|a} \right)^n A_0 r_{\text{p}}^{21} e^{-|q|\zeta} = \\
&= A_0 e^{-|q|\zeta} + \underbrace{A_0 \frac{r_{\text{p}}^{21} r_{\text{p}}^{23} e^{-2|q|a}}{1 - r_{\text{p}}^{21} r_{\text{p}}^{23} e^{-2|q|a}}}_{A_2(q)} e^{-|q|\zeta} + \underbrace{A_0 \frac{r_{\text{p}}^{21} e^{-2|q|a}}{1 - r_{\text{p}}^{21} r_{\text{p}}^{23} e^{-2|q|a}}}_{B_2(q)} e^{|q|\zeta}, \tag{5.50}
\end{aligned}$$

where the lower interface was from the start set to  $\zeta = 0$ . Replacing  $r_{\text{p}}^{21}$  and  $r_{\text{p}}^{23}$  by their full forms, one finally obtains the desired corrected expressions for the coefficients  $A_2(q)$  and  $B_2(q)$

$$A_2(q) = \frac{A_0(q) \gamma (1 - \epsilon) (1 - \delta)}{(1 + \epsilon) (1 + \delta) - \gamma (1 - \epsilon) (1 - \delta)}, \tag{5.51}$$

$$B_2(q) = \frac{A_0(q) \gamma (1 - \epsilon) (1 + \delta)}{(1 + \epsilon) (1 + \delta) - \gamma (1 - \epsilon) (1 - \delta)}, \tag{5.52}$$

Let us now repeat the above procedure for the waves transmitted through the interfaces. Abiding by the above decision to omit the waves originating in the direct scattering from the substrate, the potentials in the regions I,III become

$$\begin{aligned}
V_{\text{tot}}^{\text{I}}(q, \zeta) &= A_0 t_{\text{p}}^{21} e^{-|q|a} e^{-|q|(\zeta-a)} + A_0 t_{\text{p}}^{21} r_{\text{p}}^{21} r_{\text{p}}^{23} e^{-3|q|a} e^{-|q|(\zeta-a)} + \dots = \\
&= \sum_{n=0}^{\infty} \left( r_{\text{p}}^{21} r_{\text{p}}^{23} e^{-2|q|a} \right)^n A_0 t_{\text{p}}^{21} e^{-|q|\zeta} = \underbrace{A_0 \frac{t_{\text{p}}^{21}}{1 - r_{\text{p}}^{21} r_{\text{p}}^{23} e^{-2|q|a}}}_{A_1(q)} e^{-|q|\zeta}, \tag{5.53}
\end{aligned}$$

$$\begin{aligned}
V_{\text{tot}}^{\text{III}}(q, \zeta) &= A_0 r_{\text{p}}^{21} t_{\text{p}}^{23} e^{-2|q|a} e^{|q|\zeta} + A_0 (r_{\text{p}}^{21})^2 r_{\text{p}}^{23} t_{\text{p}}^{23} e^{-4|q|a} e^{|q|\zeta} + \dots = \\
&= \sum_{n=0}^{\infty} \left( r_{\text{p}}^{21} r_{\text{p}}^{23} e^{-2|q|a} \right)^n A_0 r_{\text{p}}^{21} t_{\text{p}}^{23} e^{-2|q|a} e^{|q|\zeta} = \underbrace{A_0 \frac{r_{\text{p}}^{21} t_{\text{p}}^{23} e^{-2|q|a}}{1 - r_{\text{p}}^{21} r_{\text{p}}^{23} e^{-2|q|a}}}_{B_3(q)} e^{|q|\zeta}, \tag{5.54}
\end{aligned}$$

Substituting for  $r_{\text{p}}^{21}$ ,  $r_{\text{p}}^{23}$ ,  $t_{\text{p}}^{21}$ ,  $t_{\text{p}}^{23}$  as before, one recovers the two remaining coefficients  $A_1(q)$  and  $B_3(q)$

$$A_1(q) = \frac{2A_0(q) (1 + \delta)}{(1 + \epsilon) (1 + \delta) - \gamma (1 - \epsilon) (1 - \delta)}, \tag{5.55}$$

$$B_3(q) = \frac{2A_0(q) \gamma (1 - \epsilon)}{(1 + \epsilon) (1 + \delta) - \gamma (1 - \epsilon) (1 - \delta)}, \tag{5.56}$$

The field profile for the same structure as in Figure 5.4, but calculated with use of the above corrected coefficients, is shown in Figure 5.5. Evidently, the disturbing field enhancement in graphene has been successfully suppressed in exchange for an apparent discontinuity in the tangential component of the electric field at the superstrate-substrate interface arising from the omission of the direct scattering from the substrate.

It turns out that one can easily remedy this inconsistency by adding to the potential in the region III an extra term  $A_0^{\text{t}}(q) e^{|q|\zeta}$  corresponding to an ordinarily transmitted plane wave. Furthermore, in the absence of the metallic cylinder, the amplitudes and the polarization directions of the fields should reduce to those prescribed by the Fresnel coefficients  $r_{\text{p}}$  and  $t_{\text{p}}$  introduced in Section 1.7. This

### 5.3. POTENTIALS

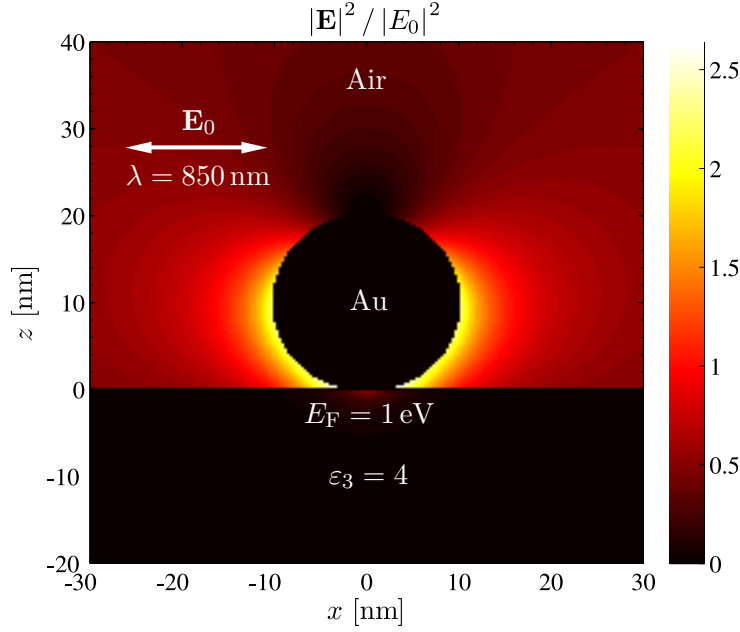


Figure 5.5: Map of the intensity of the electric field in the vicinity of an infinitely long golden cylinder with a radius  $R = 10$  nm lying on the top of a dielectric substrate covered by a graphene sheet. The distribution of the potential was calculated using the corrected coefficients given by Equations (5.51), (5.52), (5.55) and (5.56), otherwise the material and illumination parameters were the same as in Figure 5.4. Obviously, the electric field does not satisfy the customary boundary conditions at the superstrate-substrate interface.

is ensured by adjusting properly the amplitude and the orientation of the dipolar source  $\mathbf{p}$ . Adopting the above modifications, the coefficients  $A_1(q)$ ,  $B_2(q)$ ,  $A_2(q)$ ,  $B_3(q)$  eventually become

$$A_1(q) = \frac{2A_0(q)(1+\delta)}{(1+\epsilon)(1+\delta) - \gamma(1-\epsilon)(1-\delta)}, \quad (5.57)$$

$$A_2(q) = \frac{A_0(q)\gamma(1-\epsilon)(1-\delta)}{(1+\epsilon)(1+\delta) - \gamma(1-\epsilon)(1-\delta)}, \quad (5.58)$$

$$B_2(q) = \frac{A_0(q)\gamma(1-\epsilon)(1+\delta)}{(1+\epsilon)(1+\delta) - \gamma(1-\epsilon)(1-\delta)}, \quad (5.59)$$

$$B_3(q) = A_0^t(q) + \frac{2A_0(q)\gamma(1-\epsilon)}{(1+\epsilon)(1+\delta) - \gamma(1-\epsilon)(1-\delta)}, \quad (5.60)$$

$$\begin{aligned} A_0(q) &= \frac{e}{2\epsilon_0\epsilon} \left[ -i(1+r_p) \frac{q}{|q|} \Delta_\xi + \text{sgn}(\zeta)(1-r_p) \Delta_\zeta \right] = \\ &= \pi g^2 E_0 [-i(1+r_p) \text{sgn}(q) \cos \theta_i + (1-r_p) \text{sgn}(\zeta) \sin \theta_i], \end{aligned} \quad (5.61)$$

$$\begin{aligned} A_0^t(q) &= \frac{e}{2\epsilon_0\epsilon} t_p \left[ -i \frac{q}{|q|} \sqrt{\Delta_\xi^2 + \Delta_\zeta^2} \left( 1 - \frac{\epsilon_2}{\epsilon_3} \right) + \text{sgn}(\zeta) \Delta_\zeta \sqrt{\frac{\epsilon_2}{\epsilon_3}} \right] = \\ &= \pi g^2 E_0 t_p [-i \text{sgn}(q) \cos \theta_t + \text{sgn}(\zeta) \sin \theta_t], \end{aligned} \quad (5.62)$$

where  $E_0 = \frac{e}{2\pi\epsilon_0\epsilon g^2} \sqrt{\Delta_\xi^2 + \Delta_\zeta^2}$  stands for the amplitude of the incident electric field and  $\theta_i$ , resp.  $\theta_t = \arcsin\left(\sqrt{\frac{\epsilon_2}{\epsilon_3}} \sin \theta_i\right)$  denotes the angle formed by the wavevector of the incident, resp. ordinarily refracted wave with the normal vector of the superstrate-substrate interface.

Figure 5.6 proves that the proposed modifications indeed resolve the discussed discontinuity in the potential. Furthermore, the amplitude and the polarization of the external fields should now correspond to those prescribed by the Fresnel reflection and transmission coefficients. In order to support this assertion, we present in Figure 5.7 the distribution of the electric field within the same structure, except this time illuminated under a non-zero incident angle.

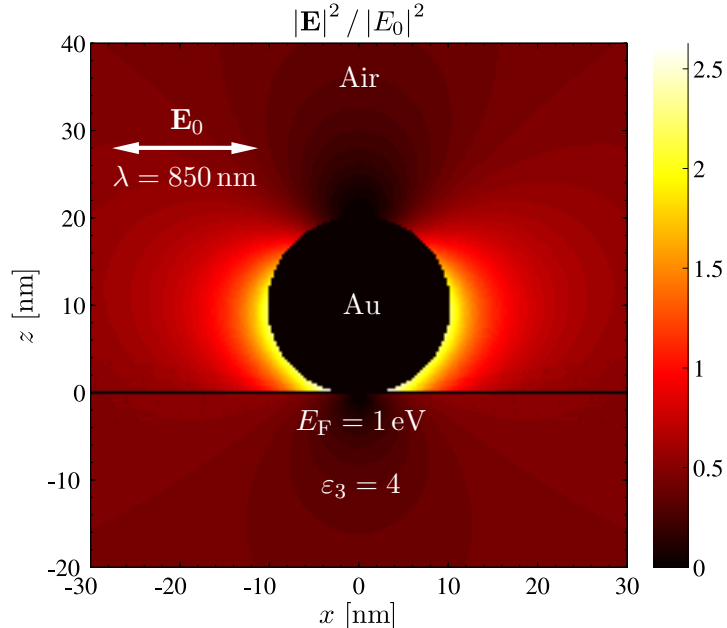


Figure 5.6: Map of the intensity of the electric field in the vicinity of an infinitely long golden cylinder with a radius  $R = 10$  nm lying on the top of a dielectric substrate covered by a graphene sheet. The distribution of the potential was calculated using the modified coefficients given by Equations (5.57)-(5.62), otherwise the material and illumination parameters were the same as in Figure 5.4. Apparently, the discontinuity in the potential has been successfully removed.

Having the tool allowing one to calculate the distribution of the electric field within the hybrid structure consisting of a metallic cylinder lying on the top of a graphene sheet, we can turn our attention to what happens and how the interaction between those two objects changes, when the Fermi energy in graphene is varied through the electrostatic gating. First of all one needs a quantity, which would reflect the changes in the response of the metallic cylinder. The amplitude and the phase of the dipole moment induced within the cylinder appear to be a natural choice, since they can be, besides other things, further employed to calculate the scattering and extinction efficiencies of the plasmonic antenna.

#### 5.4. Dyadic Green's functions

The frequency-dependent electrodynamic response of a plasmonic antenna basically prescribes, how much the antenna will be polarized when exposed to external electromagnetic radiation of a given frequency  $\omega$ . The state of the polarization within the antenna is characterized by the polarization vector  $\mathbf{P}(\mathbf{r}, \omega)$  defined as the induced dipole moment per a unit volume and within the local linear response theory it is directly proportional to the electric field at the same position  $\mathbf{r}$

$$\mathbf{P}(\mathbf{r}, \omega) = \varepsilon_0 (\varepsilon(\omega) - 1) \mathbf{E}(\mathbf{r}, \omega), \quad (5.63)$$

#### 5.4. DYADIC GREEN'S FUNCTIONS

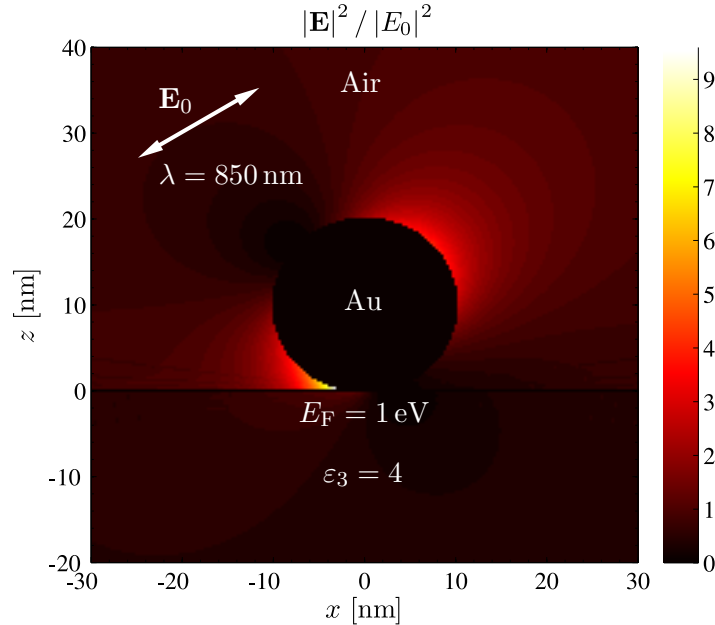


Figure 5.7: Map of the intensity of the electric field in the vicinity of an infinitely long golden cylinder with a radius  $R = 10$  nm lying on the top of a dielectric substrate covered by a graphene sheet. The illumination was tilted by 30 degrees, otherwise the parameters of the calculation were the same as in Figure 5.4.

where  $\varepsilon(\omega)$  is the frequency dependent dielectric function of the material constituting the antenna. To some extent, one can describe the response of the antenna by the total dipole moment

$$\mathbf{p}(\mathbf{r}_T, \omega) = \int_{\Omega} d^3\mathbf{r} \mathbf{P}(\mathbf{r}, \omega), \quad (5.64)$$

where the integration spans the whole volume of the antenna  $\Omega$  and where  $\mathbf{r}_T$  denotes the dipole's "center of the mass" calculated as

$$\mathbf{r}_T = \frac{\int_{\Omega} d^3\mathbf{r} |\mathbf{P}(\mathbf{r}, \omega)| \mathbf{r}}{\int_{\Omega} d^3\mathbf{r} |\mathbf{P}(\mathbf{r}, \omega)|}. \quad (5.65)$$

Apparently, by characterizing the antenna with a single dipole, one neglects the small scale variations in the polarization state of the antenna, but that should not play a significant role as long as the size of the antenna is much smaller than the wavelength of the incident radiation.

In the spirit of the quasistatic approximation, we shall assume that the fields calculated by the transformation optics method vary harmonically in time and so does the dipole moment induced within the antenna. An oscillating dipole emits energy in the form of electromagnetic waves with a radiation pattern we are now going to calculate.

The starting point are the Maxwell's equations for the six unknown components of the electric and magnetic fields  $\mathbf{E}(\mathbf{r}, \omega)$  and  $\mathbf{H}(\mathbf{r}, \omega)$ . Usually, the problem of solving them is simplified by the transition to the scalar and vector potentials  $V(\mathbf{r}, \omega)$  and  $\mathbf{A}(\mathbf{r}, \omega)$ , which reduces the number of the equations

## 5. CALCULATIONS BASED ON THE TRANSFORMATION OPTICS METHOD

and unknowns in exchange for an increase in their differential order. In homogenous non-magnetic media, the scalar and vector potentials are required to satisfy the following equations

$$\nabla^2 V(\mathbf{r}, \omega) + \varepsilon(\omega) \frac{\omega^2}{c^2} V(\mathbf{r}, \omega) = -\frac{\rho(\mathbf{r}, \omega)}{\varepsilon_0 \varepsilon(\omega)}, \quad (5.66)$$

$$\nabla^2 \mathbf{A}(\mathbf{r}, \omega) + \varepsilon(\omega) \frac{\omega^2}{c^2} \mathbf{A}(\mathbf{r}, \omega) = -\mu_0 \mathbf{j}(\mathbf{r}, \omega), \quad (5.67)$$

where  $\varepsilon(\omega)$  denotes the dielectric function of the medium,  $\rho$  and  $\mathbf{j}$  stand for the external charge and current densities and  $\mu_0$  is the vacuum susceptibility. Notice that the Lorenz-Lorentz gauge  $\nabla \cdot \mathbf{A} = i\omega\varepsilon_0\mu_0\varepsilon V$  has been implicitly assumed. Importantly, the electric and magnetic fields can be calculated from the potentials through

$$\mathbf{E}(\mathbf{r}, \omega) = -\nabla V(\mathbf{r}, \omega) + i\omega \mathbf{A}(\mathbf{r}, \omega), \quad \mathbf{B}(\mathbf{r}, \omega) = \nabla \times \mathbf{A}(\mathbf{r}, \omega). \quad (5.68)$$

The general solutions for the potentials satisfying Equations (5.67) and (5.66) can be written in the following integral form

$$V(\mathbf{r}, \omega) = \int_{-\infty}^{\infty} d^3 \mathbf{r}' G_0(\mathbf{r}, \mathbf{r}', \omega) \frac{\rho(\mathbf{r}', \omega)}{\varepsilon_0 \varepsilon(\omega)}, \quad (5.69)$$

$$\mathbf{A}(\mathbf{r}, \omega) = \mu_0 \int_{-\infty}^{\infty} d^3 \mathbf{r}' G_0(\mathbf{r}, \mathbf{r}', \omega) \mathbf{j}(\mathbf{r}', \omega), \quad (5.70)$$

where  $G_0(\mathbf{r}, \mathbf{r}', \omega)$  is a yet to be specified Green's function describing the response of the system to a point source positioned at  $\mathbf{r}'$

$$\nabla^2 G_0(\mathbf{r}, \mathbf{r}', \omega) + \varepsilon(\omega) \frac{\omega^2}{c^2} G_0(\mathbf{r}, \mathbf{r}', \omega) = -\delta(\mathbf{r} - \mathbf{r}'). \quad (5.71)$$

In the present case of a single oscillating dipole, the current density is readily calculated as the time derivative of the induced dipole moment  $\mathbf{j}(\mathbf{r}', \omega) = -i\omega \mathbf{p}(\omega) \delta(\mathbf{r} - \mathbf{r}_T)$ , but one can not claim the same concerning the charge density. Fortunately, the electric and magnetic fields can be expressed exclusively in terms of the current density by exploiting the above gauge condition, which links together the scalar and the vector potential

$$\mathbf{E}(\mathbf{r}, \omega) = \left( i\omega + i \frac{\nabla \nabla \cdot}{\omega \varepsilon_0 \mu_0 \varepsilon(\omega)} \right) \mathbf{A}(\mathbf{r}, \omega) = i\omega \left( 1 + \frac{1}{k^2} \nabla \nabla \cdot \right) \int_{-\infty}^{\infty} d^3 \mathbf{r}' G_0(\mathbf{r}, \mathbf{r}', \omega) \mathbf{j}_{\text{ext}}(\mathbf{r}', \omega), \quad (5.72)$$

where the wavevector  $k = \sqrt{\varepsilon(\omega)} \frac{\omega}{c}$  has been introduced. Recalling that the operator  $\nabla$  acts only on functions depending on the unprimed coordinates and assuming one can reverse the order of differentiation and integration, the above equation becomes

$$\begin{aligned} \mathbf{E}(\mathbf{r}, \omega) &= i\omega \mu_0 \int_{-\infty}^{\infty} d^3 \mathbf{r}' \left\{ G_0(\mathbf{r}, \mathbf{r}', \omega) \mathbf{j}(\mathbf{r}', \omega) + \frac{1}{k^2} \nabla [\nabla G_0(\mathbf{r}, \mathbf{r}', \omega) \cdot \mathbf{j}(\mathbf{r}', \omega)] \right\} = \\ &= i\omega \mu_0 \int_{-\infty}^{\infty} d^3 \mathbf{r}' \left[ G_0 \mathbf{j} + \frac{1}{k^2} \left( \mathbf{n}_x \frac{\partial^2 G_0}{\partial x^2} + \mathbf{n}_y \frac{\partial^2 G_0}{\partial x \partial y} + \mathbf{n}_z \frac{\partial^2 G_0}{\partial x \partial z} \right) j_x + \dots \right], \end{aligned} \quad (5.73)$$

#### 5.4. DYADIC GREEN'S FUNCTIONS

where  $\mathbf{n}_x$ ,  $\mathbf{n}_y$  and  $\mathbf{n}_z$  are the unit vectors of the cartesian coordinate system and where the arguments of the functions have been dropped in exchange for a more compact notation. The dots indicate that the terms containing  $j_y$  and  $j_z$  are analogous to that one associated with  $j_x$ . The above equation can be rewritten into a more lucid matrix form

$$\begin{aligned} \mathbf{E}(\mathbf{r}, \omega) &= i\omega\mu_0 \int_{-\infty}^{\infty} d^3\mathbf{r}' \frac{1}{k^2} \begin{pmatrix} k^2 + \frac{\partial^2}{\partial x^2} & \frac{\partial^2}{\partial x\partial y} & \frac{\partial^2}{\partial x\partial z} \\ \frac{\partial^2}{\partial x\partial y} & k^2 + \frac{\partial^2}{\partial y^2} & \frac{\partial^2}{\partial y\partial z} \\ \frac{\partial^2}{\partial x\partial z} & \frac{\partial^2}{\partial y\partial z} & k^2 + \frac{\partial^2}{\partial z^2} \end{pmatrix} G_0(\mathbf{r}, \mathbf{r}', \omega) \begin{pmatrix} j_x(\mathbf{r}', \omega) \\ j_y(\mathbf{r}', \omega) \\ j_z(\mathbf{r}', \omega) \end{pmatrix} = \\ &= i\omega\mu_0 \int_{-\infty}^{\infty} d^3\mathbf{r}' \overset{\leftrightarrow}{\mathbf{G}}(\mathbf{r}, \mathbf{r}', \omega) \mathbf{j}(\mathbf{r}', \omega). \end{aligned} \quad (5.74)$$

The tensor  $\overset{\leftrightarrow}{\mathbf{G}}(\mathbf{r}, \mathbf{r}', \omega)$  is usually called as the dyadic Green's function and having a known distribution of currents, it allows one to calculate the electric field due to those currents at all points of the space.

In a homogenous two-dimensional space, the Green's function  $G_0(\mathbf{r}, \mathbf{r}', \omega)$  is represented by the zeroth order Hankel function of the first kind  $H_0^{(1)}$  [8]

$$G_0(\mathbf{r}, \mathbf{r}', \omega) = \frac{i}{4} H_0^{(1)}(k|\mathbf{r} - \mathbf{r}'|) = \frac{i}{4\pi} \int_{-\infty}^{\infty} dk_x \frac{e^{ik_x(x-x') + ik_z|z-z'|}}{k_z}, \quad (5.75)$$

where  $k_x$  and  $k_z = \sqrt{k^2 - k_x^2}$  are the components of the wavevector  $\mathbf{k}$ .

The above integral representation shall become handy once we start to consider the present geometry containing a superstrate-substrate interface, which disturbs the homogeneity of the space and forces us to find a modified expression for the Green's function. Interestingly, after inserting the prescription for its "homogenous" version into Equation (5.74), the electric field becomes a superposition of many propagating plane waves

$$\begin{aligned} \mathbf{E}(\mathbf{r}, \omega) &= i\omega\mu_0 \int_{-\infty}^{\infty} d^2\mathbf{r}' \int_{-\infty}^{\infty} dk_x \frac{i}{4\pi k^2} \overset{\leftrightarrow}{\mathbf{M}}_0(k_x, \omega) \frac{e^{ik_x(x-x') + ik_z|z-z'|}}{k_z} \mathbf{j}(x', z', \omega), \\ \overset{\leftrightarrow}{\mathbf{M}}_0(k_x, \omega) &= \begin{pmatrix} k_z^2 & 0 & -k_x k_z \operatorname{sgn}(z-z') \\ 0 & k^2 & 0 \\ -k_x k_z \operatorname{sgn}(z-z') & 0 & k_x^2 \end{pmatrix}. \end{aligned} \quad (5.76)$$

One can account for the presence of a planar interface by introducing two extra terms to the present homogenous dyadic Green's function. The first one should capture reflections of the emitted radiation from the interface, whereas the latter is supposed to characterize the radiation transmitted through. The integral form enables straightforward implementation, since one only needs to multiply the amplitudes of the plane waves by the Fresnel coefficients  $r_p$  and  $t_p$  given by Equations (1.100) and (1.99) and to adjust properly the polarization of the reflected and transmitted waves. Adopting the above suggestions, the dyadic Green's function in the presence of a planar interface set at  $z = 0$  reads

$$\begin{aligned}
 z > 0: \quad \overset{\leftrightarrow}{\mathbf{G}}(\mathbf{r}, \mathbf{r}', \omega) &= \frac{i}{4\pi k_2^2} \left[ \overset{\leftrightarrow}{\mathbf{M}}_0(k_x) \frac{e^{ik_x(x-x') + ik_{2z}|z-z'|}}{k_{2z}} + \overset{\leftrightarrow}{\mathbf{M}}_{\text{ref}}(k_x) r_p(k_x) \frac{e^{ik_x(x-x') + ik_{2z}(z+z')}}{k_{2z}} \right], \\
 \overset{\leftrightarrow}{\mathbf{M}}_0(k_x) &= \begin{pmatrix} k_{2z}^2 & -k_x k_{2z} \operatorname{sgn}(z-z') \\ -k_x k_{2z} \operatorname{sgn}(z-z') & k_x^2 \end{pmatrix}, \\
 \overset{\leftrightarrow}{\mathbf{M}}_{\text{ref}}(k_x, \omega) &= \begin{pmatrix} k_{2z}^2 & k_x k_{2z} \\ -k_x k_{2z} & -k_x^2 \end{pmatrix}, \tag{5.77}
 \end{aligned}$$

$$\begin{aligned}
 z < 0: \quad \overset{\leftrightarrow}{\mathbf{G}}(\mathbf{r}, \mathbf{r}', \omega) &= \frac{ik_3}{4\pi k_2} \overset{\leftrightarrow}{\mathbf{M}}_{\text{tr}}(k_x) t_p(k_x) \frac{e^{ik_x(x-x') + ik_{2z}z' - ik_{3z}z}}{k_{2z}}, \\
 \overset{\leftrightarrow}{\mathbf{M}}_{\text{tr}}(k_x) &= \begin{pmatrix} k_{2z}k_{3z} & k_x k_{3z} \\ k_x k_{2z} & k_x^2 \end{pmatrix}, \tag{5.78}
 \end{aligned}$$

where the indices indicate, whether one should take the dielectric function of the superstrate  $\varepsilon_2$  or the substrate  $\varepsilon_3$ . Notice that for the present two-dimensional geometry, one can drop the matrix elements associated with the  $y$ -coordinate.

The integrals contained in the above equations do not have generally a simple analytic solution and they have to be calculated numerically, which might be computationally demanding. Fortunately, we are interested mainly in the far-field distribution of the electromagnetic fields, which permits us to use their approximate asymptotic representation. We successfully employed the method of stationary phase (Mandel [21], p. 128), which is applicable to certain integrals with rapidly oscillating arguments. Since the actual calculation of the integrals is rather a mathematical problem, we present here only the final expressions, referring the reader for the detailed derivation to Appendix B. Hence, the scattered electric field far away from the sources can be calculated using the following approximate form of the dyadic Green's function

$$\begin{aligned}
 z > 0: \quad \overset{\leftrightarrow}{\mathbf{G}}^{\text{FF}}(\mathbf{r}, \mathbf{r}', \omega) &= \frac{i}{4\pi} \sqrt{\frac{2\pi}{k_2 r}} e^{ik_2 r} e^{-i\pi/4} e^{-ik_2 s_x x'} \left[ e^{-ik_2 s_z z'} \overset{\leftrightarrow}{\mathbf{M}}_0^{\text{FF}}(s_x) + r_p(s_x k_2) e^{ik_2 s_z z'} \overset{\leftrightarrow}{\mathbf{M}}_{\text{ref}}^{\text{FF}}(s_x) \right], \\
 \overset{\leftrightarrow}{\mathbf{M}}_0^{\text{FF}}(s_x) &= \begin{pmatrix} s_z^2 & -s_x s_z \\ -s_x s_z & s_x^2 \end{pmatrix}, \\
 \overset{\leftrightarrow}{\mathbf{M}}_{\text{ref}}^{\text{FF}}(s_x) &= \begin{pmatrix} s_z^2 & s_x s_z \\ -s_x s_z & -s_x^2 \end{pmatrix}, \\
 z < 0: \quad \overset{\leftrightarrow}{\mathbf{G}}^{\text{FF}}(\mathbf{r}, \mathbf{r}', \omega) &= \frac{ik_3}{4\pi k_2} \sqrt{\frac{2\pi}{k_3 r}} e^{ik_3 r} e^{-i\pi/4} t_p(s_x k_3) e^{-ik_3 s_x x'} e^{i\sqrt{k_2^2 - s_x^2} k_3 z'} \overset{\leftrightarrow}{\mathbf{M}}_{\text{tr}}^{\text{FF}}(s_x), \\
 \overset{\leftrightarrow}{\mathbf{M}}_{\text{tr}}^{\text{FF}}(s_x) &= \begin{pmatrix} s_z^2 & s_x s_z \frac{k_3}{\sqrt{k_2^2 - s_x^2} k_3} \\ s_x s_z & s_x^2 s_z \frac{k_3}{\sqrt{k_2^2 - s_x^2} k_3} \end{pmatrix}, \tag{5.79}
 \end{aligned}$$

where the upper index FF emphasizes the fact that we used the far-field approximation,  $r = \sqrt{x^2 + z^2} \gg \sqrt{x'^2 + z'^2}$  denotes the radial distance from the origin and  $s_x = \frac{x}{r}$ ,  $s_z = \sqrt{1 - s_x^2}$  determine the direction, in which the scattered radiation is measured. Interestingly, all the plane waves cancel each other out except the one propagating exactly in the direction of the observer and the resulting wavefront has the form of an outgoing cylindrical wave with the angular distribution modulated by the Fresnel coefficients  $r_p$  a  $t_p$ .

The amount of energy scattered by the plasmonic antenna into a particular direction is determined by the time-averaged Poynting vector (Bohren and Huffman [7], p. 23) defined as

$$\langle \mathbf{S}(s_x, \omega) \rangle = \frac{1}{2} \operatorname{Re} \{ \mathbf{E}(s_x, \omega) \times \mathbf{H}^*(s_x, \omega) \}. \tag{5.80}$$

## 5.5. RESULTS

The far-field auxilliary magnetic field  $\mathbf{H} = \frac{\mathbf{B}}{\mu_0}$  can be obtained in a similar manner as the electric field or one can take advantage of the fact that far away from the origin, the cylindrical wave can be locally regarded as a plane wave, thus the electric and magnetic fields should be perpendicular to each other and their magnitudes related through  $|\mathbf{H}| = \frac{\sqrt{\epsilon}}{\mu_0 c} |\mathbf{E}|$ . Exploiting these properties, the far-field magnetic field reads

$$\mathbf{H}(s_x, \omega) = \int_{-\infty}^{\infty} d^2\mathbf{r}' \overset{\leftrightarrow}{\mathbf{G}}_{\mathbf{H}}^{\text{FF}}(s_x, \mathbf{r}', \omega) \mathbf{j}(\mathbf{r}', \omega), \quad (5.81)$$

$$\begin{aligned} z > 0: \quad \overset{\leftrightarrow}{\mathbf{G}}_{\mathbf{H}}^{\text{FF}}(s_x, \mathbf{r}', \omega) &= \mathbf{n}_y \frac{k_2}{4\pi} \sqrt{\frac{2\pi}{k_2 r}} e^{ik_2 r} e^{-i\pi/4} e^{-ik_2 s_x x'} \left[ e^{-ik_2 s_z z'} \overset{\leftrightarrow}{\mathbf{N}}_0^{\text{FF}}(s_x) + r_p(s_x k_2) e^{ik_2 s_z z'} \overset{\leftrightarrow}{\mathbf{N}}_{\text{ref}}^{\text{FF}}(s_x) \right], \\ \overset{\leftrightarrow}{\mathbf{N}}_0^{\text{FF}}(s_x) &= \begin{pmatrix} -s_z & s_x \end{pmatrix}, \\ \overset{\leftrightarrow}{\mathbf{N}}_{\text{ref}}^{\text{FF}}(s_x) &= \begin{pmatrix} -s_z & -s_x \end{pmatrix}, \\ z < 0: \quad \overset{\leftrightarrow}{\mathbf{G}}_{\mathbf{H}}^{\text{FF}}(s_x, \mathbf{r}', \omega) &= \frac{ik_3^2}{4\pi k_2} \sqrt{\frac{2\pi}{k_3 r}} e^{ik_3 r} e^{-i\pi/4} t_p(s_x k_3) e^{-ik_3 s_x x'} e^{i\sqrt{k_2^2 - s_x^2 k_3^2} z'} \overset{\leftrightarrow}{\mathbf{N}}_{\text{tr}}^{\text{FF}}(s_x), \\ \overset{\leftrightarrow}{\mathbf{N}}_{\text{tr}}^{\text{FF}}(s_x) &= \begin{pmatrix} s_z & s_x s_z \frac{k_3}{\sqrt{k_2^2 - s_x^2 k_3^2}} \end{pmatrix}. \end{aligned} \quad (5.82)$$

In order to calculate the total power scattered  $P_{\text{sca}}$  by a plasmonic antenna, one has to integrate the Poynting vector over all the possible scattering directions. Analytical integration is probably out of the question, since the Fresnel coefficients spoil the simple and integrable form of the "homogenous" dyadic Green's function. The numerical approach resides in expressing the far-field electric and magnetic fields at the boundary of a large imaginary circle (in 3D it would be a sphere), then constructing the Poynting vector and eventually integrating it numerically over the whole circle

$$P_{\text{sca}}(\omega) = \int_{\text{circle}} ds_x \langle \mathbf{S}(s_x, \omega) \rangle \cdot \mathbf{n}(s_x), \quad (5.83)$$

where  $\mathbf{n}(s_x)$  is the outer normal of the circle.

In the following section, we shall discuss the scattering properties of hybrid plasmonic structures in terms of the scattering efficiency, which is defined as the ratio of the scattered power  $P_{\text{sca}}$  to the geometrical cross-section  $G$  of the structure multiplied by the intensity of the incident electromagnetic radiation  $I_0 = \frac{1}{2} \epsilon_0 \sqrt{\epsilon_2} c |E_0|^2$

$$Q_{\text{sca}}(\omega) = \frac{P_{\text{sca}}}{I_0 G}. \quad (5.84)$$

## 5.5. Results

Having the tools enabling us to characterize scattering properties of plasmonic structures, we shall proceed with their application to the present case of a metallic cylinder lying on the top of a dielectric substrate covered by a single sheet of electrostatically doped graphene. From the viewpoint of the device proposed in Chapter 4, the most important characteristic is whether the spectral position of the cylinder's plasmonic resonance is being shifted as one varies the doping level in graphene through the gating voltage.

To estimate the strength of the interaction between those two objects, series of calculations with a varying doping level in graphene have been performed. The distribution of the electric field within the cylinder has been used to calculate the total induced dipole moment (Eq. (5.63) and (5.64)).

## 5. CALCULATIONS BASED ON THE TRANSFORMATION OPTICS METHOD

Subsequently, employing the above apparatus of the dyadic Green's functions, the angular distributions of the electric and magnetic fields far away from the plasmonic antenna have been calculated. Finally, by constructing the Poynting vector and integrating it over all the possible scattering directions, the scattering efficiency of the metallic cylinder, which also takes into account the influence of the substrate, has been obtained.

Figure 5.8 shows the spectral dependence of the scattering efficiency  $Q_{\text{sca}}$  as a function of the graphene's Fermi energy  $E_{\text{F}}$  for a golden cylinder with a radius  $R = 30$  nm. The permittivity of the substrate has been set to  $\varepsilon_3 = 4$  and the polarization of the incident electric field is parallel with the superstrate-substrate interface. The dotted curve is plotted to give the reader a better impression of the shape of the plasmonic resonance. It would seem that the variation of the graphene's doping level has absolutely no effect on the resonance of the cylinder. That is quite a surprise, because one would expect at least a slight broadening of the plasmonic peak for the low values of  $E_{\text{F}}$  due to the increased probability of photons and localized plasmons to decay directly into electron-hole pairs in graphene.

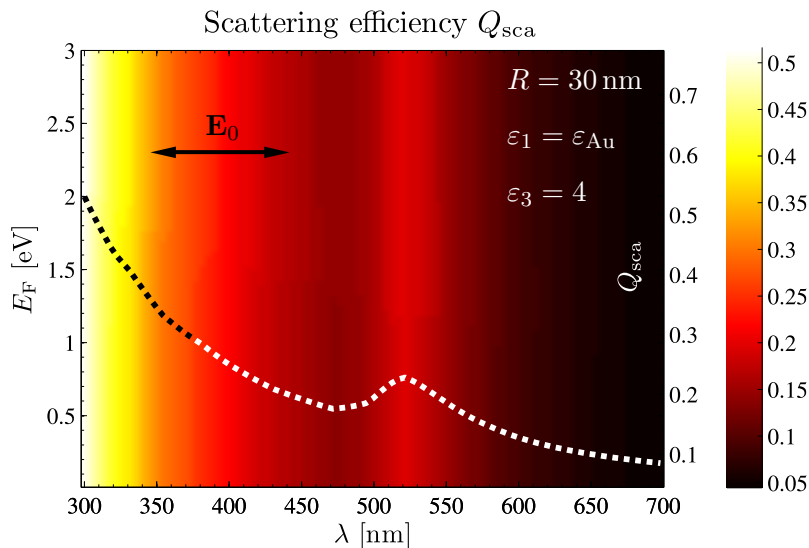


Figure 5.8: Spectral dependence of the scattering efficiency  $Q_{\text{sca}}$  of a golden cylinder situated on the top of a dielectric substrate covered by a graphene sheet as a function of the graphene's Fermi energy  $E_{\text{F}}$ . The dotted line reveals in a more detail the shape of the resonance peak. The radius of the cylinder and the permittivity of the substrate have been set to  $R = 30$  nm and  $\varepsilon_3 = 4$ . The incident electric field is polarized parallelly to the superstrate-substrate interface and the relaxation time associated with the scattering of electrons from impurities and phonons in graphene is assumed to be  $\tau = 10^{-13}$  s. Evidently, the changes in the Fermi energy do not affect at all the plasmonic resonance of the golden cylinder.

The performance of the hypothetical device from Chapter 4 is based on the assumption that one can use graphene to control the phase shift of the oscillating dipoles induced within the plasmonic antennas. The spectral dependence of the scattering efficiency  $Q_{\text{sca}}$  from Figure 5.8 clearly does not support such hypothesis. Just to be sure, we plot in Figure 5.9 the phase shift  $\Phi$  of the total induced dipole moment with respect to the incident electric field as a function of both the wavelength and the graphene's Fermi energy. The absence of observable changes in the phase shift with the varying doping level confirms the preceding findings.

The characteristic yellow colouring of gold is caused by its strong absorptivity in the blue part of the visible spectrum, reflecting the existence of optical interband transitions at these frequencies. They also strongly affect the spectral width of the plasmonic resonances falling within their proximity. For these reasons another series of calculations has been performed, but this time using silver instead

## 5.5. RESULTS

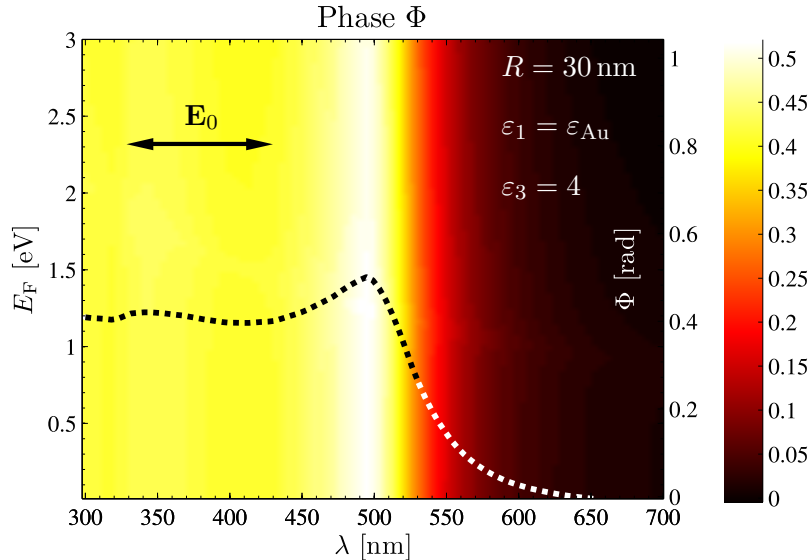


Figure 5.9: The phase shift  $\Phi$  of the dipole moment  $\mathbf{p}$  induced within the golden cylinder with respect to the incident electric field  $\mathbf{E}_0$  as a function of the wavelength  $\lambda$  and the graphene's Fermi energy  $E_F$ . The parameters of the calculation are the same as in Figure 5.8.

of gold, since the onset of interband transitions in silver is shifted to the UV part of the spectrum. Furthermore, the polarization of the incident plane wave has been tilted by 30 degrees in order to increase the intensity of the electric field near the substrate and hence the mutual interaction with the cylinder (the field enhancement is apparent from Figure 5.7).

The resulting spectral dependences of the scattering efficiency and the phase shift as a function of the doping level in graphene are plotted in Figures 5.10 and 5.11. Even though both the spectral width of the plasmonic resonance and the range of attainable phase shifts have been improved, there are no indications that a single graphene sheet is capable of the control over the electrodynamic response of ordinary plasmonic structures in the visible range of the spectrum.

Such unexpected results pose a question, whether the transformation optics method is indeed a suitable technique for the investigation of the interaction between the plasmonic structures and graphene. In order to confirm or refute such hypothesis, we performed similar calculations using a different, fully numerical method, which does not neglect retardation effects and allows one to consider more complex geometries.

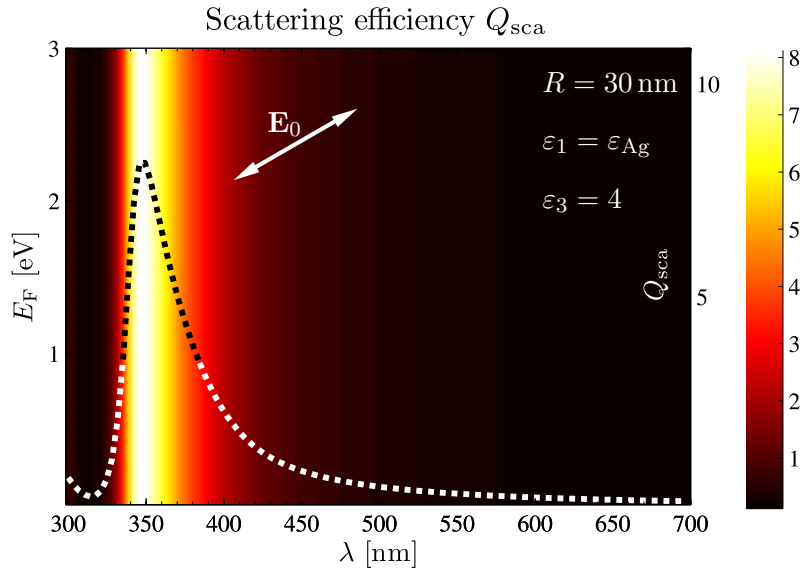


Figure 5.10: Spectral dependence of the scattering efficiency  $Q_{\text{sca}}$  of a silver cylinder situated on the top of a dielectric substrate covered by a graphene sheet as a function of the graphene's Fermi energy  $E_F$ . The illumination is tilted by 30 degrees, otherwise the parameters of the calculation are the same as in Figure 5.8.

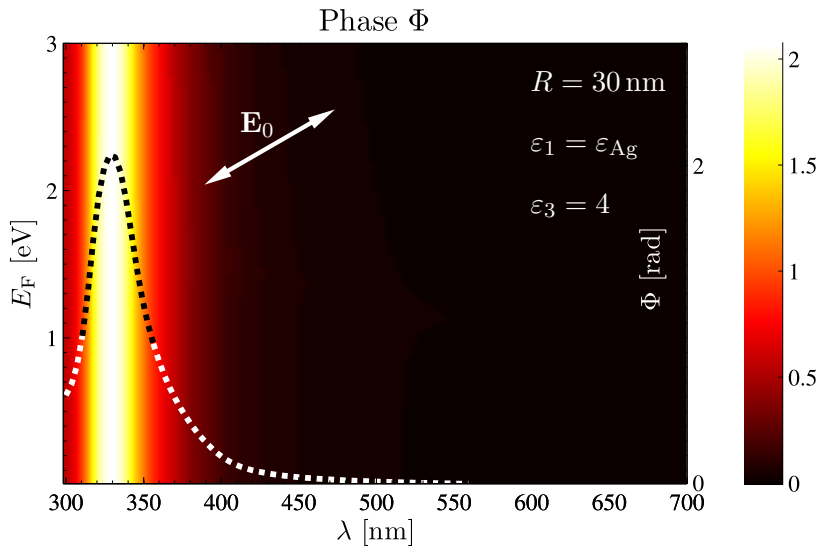


Figure 5.11: The phase shift  $\Phi$  of the dipole moment  $\mathbf{p}$  induced within the silver cylinder with respect to the incident electric field  $\mathbf{E}_0$  as a function of the wavelength  $\lambda$  and the graphene's Fermi energy  $E_F$ . The parameters of the calculation are the same as in Figure 5.10.

## 5.5. RESULTS

## 6. Calculations based on the boundary element method

From the variety of techniques suitable for light scattering simulations, we have chosen the boundary element method (BEM), which should not be computationally demanding and which offers a good control over the various parameters of the simulations. The core of this method resides in expressing the solution to Maxwell's equations in terms of surface integrals involving interface charges and currents, which act as sources of the induced electromagnetic field. We shall present here only the outline of the BEM, since it has already been nicely and comprehensively described in the paper by Abajo and Howie [10]. More attention will be dedicated to passages, where the formalism needs to be modified in order to ensure its applicability also to problems with a 2D geometry.

### 6.1. Formalism

The starting point are the second order differential equations for the scalar and vector potentials  $V$  and  $\mathbf{A}$  presented in Chapter 5, except this time we shall account for the possibility that the dielectric function  $\varepsilon$  might depend on the spatial coordinates, which corresponds to the situation of a space formed by more than one medium and containing various inhomogeneities. Recalling that  $\mathbf{E} = -\nabla V + i\omega\mathbf{A}$  and  $\mathbf{B} = \nabla \times \mathbf{A}$ , the Maxwell's equations can be combined to give

$$\nabla \cdot [\varepsilon(\mathbf{r}) \mathbf{E}(\mathbf{r}, \omega)] = \nabla \varepsilon(\mathbf{r}) \cdot \mathbf{E}(\mathbf{r}, \omega) + \varepsilon(\mathbf{r}) \nabla \cdot \mathbf{E}(\mathbf{r}, \omega) = \frac{\rho(\mathbf{r}, \omega)}{\varepsilon_0}, \quad (6.1)$$

$$-\nabla^2 V(\mathbf{r}, \omega) + i\omega \nabla \cdot \mathbf{A}(\mathbf{r}, \omega) = \frac{\rho(\mathbf{r}, \omega)}{\varepsilon_0 \varepsilon(\mathbf{r})} - \frac{\nabla \varepsilon(\mathbf{r})}{\varepsilon(\mathbf{r})} \cdot \mathbf{E}(\mathbf{r}, \omega) \quad (6.2)$$

and

$$\nabla [\nabla \cdot \mathbf{A}(\mathbf{r}, \omega)] - \nabla^2 \mathbf{A}(\mathbf{r}, \omega) = \mu_0 \mathbf{j}(\mathbf{r}, \omega) - i\omega \mu_0 \varepsilon_0 \varepsilon(\mathbf{r}, \omega) [-\nabla V(\mathbf{r}, \omega) + i\omega \mathbf{A}], \quad (6.3)$$

where the media are implicitly assumed to be non-magnetic. Employing the Lorentz-Lorenz gauge condition  $\nabla \cdot \mathbf{A} = i\omega \mu_0 \varepsilon_0 \varepsilon V$  and dropping the arguments of functions in exchange for a more compact notation, the above equations reduce to

$$\nabla^2 V + \varepsilon \frac{\omega^2}{c^2} V = -\frac{\rho}{\varepsilon_0 \varepsilon} - \varepsilon \mathbf{E} \cdot \nabla \left( \frac{1}{\varepsilon} \right) \quad (6.4)$$

and

$$i\omega \mu_0 \varepsilon_0 \nabla(\varepsilon V) - \nabla^2 \mathbf{A} = \mu_0 \mathbf{j} + \varepsilon \frac{\omega^2}{c^2} \mathbf{A} + i\omega \mu_0 \varepsilon_0 \varepsilon V, \quad (6.5)$$

$$\nabla^2 \mathbf{A} + \varepsilon \frac{\omega^2}{c^2} \mathbf{A} = -\mu_0 \mathbf{j} + i\omega \mu_0 \varepsilon_0 V \nabla \varepsilon. \quad (6.6)$$

Evidently, Equations (6.4) and (6.6) are coupled to each other through the terms containing the gradient of the dielectric function. Let us now assume that the space consists of several regions (particles, media etc.) with different dielectric properties and that they are separated by abrupt interfaces. Then the terms associated with inhomogeneities are non-zero only at the boundaries of those regions and they can be interpreted as additional charge and current sources. Invoking the general solutions for scalar and vector potentials in a homogenous space given by Equations (6.7) and (6.8),

## 6.1. FORMALISM

the solution in a particular region can be expressed as a sum over the contributions from the external sources enclosed within and the additional sources induced at its boundaries

$$V_\nu(\mathbf{r}, \omega) = \int_{\Omega_\nu} d^2\mathbf{r}' G_\nu(\mathbf{r}, \mathbf{r}', \omega) \frac{\rho(\mathbf{r}', \omega)}{\varepsilon_0 \varepsilon_\nu(\omega)} + \int_{\partial\Omega_\nu} d\mathbf{s} G_\nu(\mathbf{r}, \mathbf{s}, \omega) \sigma_\nu(\mathbf{s}, \omega), \quad (6.7)$$

$$\mathbf{A}_\nu(\mathbf{r}, \omega) = \mu_0 \int_{\Omega_\nu} d^2\mathbf{r}' G_0(\mathbf{r}, \mathbf{r}', \omega) \mathbf{j}(\mathbf{r}', \omega) + \int_{\partial\Omega_\nu} d\mathbf{s} G_\nu(\mathbf{r}, \mathbf{s}, \omega) \mathbf{h}_\nu(\mathbf{s}, \omega), \quad (6.8)$$

where  $\sigma_\nu$ ,  $\mathbf{h}_\nu$  stand for the yet unknown auxilliary boundary charges and currents assigned to the  $\nu$ -th region and  $\Omega$ ,  $\partial\Omega$  indicate, whether the integration is performed over the region's volume or along its boundary. As pointed out in Chapter 5, the 2D Green's function  $G_\nu$  is given by the zeroth order Hankel function of the first kind  $G_\nu(\mathbf{r}, \mathbf{r}', \omega) = \frac{i}{4} H_0^{(1)}(k_\nu |\mathbf{r} - \mathbf{r}'|)$ ,  $k_\nu = \sqrt{\varepsilon_\nu} \frac{\omega}{c}$ .

Although the presented formalism can be applied, in principle, to any conceivable geometry, only for few of them there exists an analytical solution. Nevertheless, these integral solutions can become a powerful tool when combined with the computational resources we are nowadays provided. The transformation into a form suitable for numerical calculations relies on the discretization of the region boundaries into a limited set of small surface elements  $\Delta\mathbf{s}$ . Assuming both the electromagnetic fields and the auxilliary sources exhibit only small variations between two contiguous discretization points, one can consider these quantities to be nearly constant within a single surface element and discretize them as well. However, we have to be careful when applying such approximation to the Green's function, since it varies dramatically for small values of its argument (this holds both in 3D and 2D)

$$\lim_{k_\nu r \rightarrow 0} H_0^{(1)}(k_\nu r) \approx 1 + i \frac{2}{\pi} \left[ \ln \left( \frac{k_\nu r}{2} \right) + \gamma \right], \quad (6.9)$$

with  $\gamma \doteq 0.57721$  denoting the Euler-Mascherani constant. Nevertheless far away from the boundary sources, where the Green's function is "well-behaving", the solutions to the potentials after the discretization assume the following form

$$V_\nu(\mathbf{r}, \omega) = \int_{\Omega_\nu} d^2\mathbf{r}' G_\nu(\mathbf{r}, \mathbf{r}', \omega) \frac{\rho(\mathbf{r}', \omega)}{\varepsilon_0 \varepsilon_\nu(\omega)} + \sum_{\mathbf{s}_j} \Delta\mathbf{s}_j G_\nu(\mathbf{r}, \mathbf{s}_j, \omega) \sigma_\nu(\mathbf{s}_j, \omega), \quad (6.10)$$

$$\mathbf{A}_\nu(\mathbf{r}, \omega) = \mu_0 \int_{\Omega_\nu} d^2\mathbf{r}' G_0(\mathbf{r}, \mathbf{r}', \omega) \mathbf{j}(\mathbf{r}', \omega) + \sum_{\mathbf{s}_j} \Delta\mathbf{s}_j G_\nu(\mathbf{r}, \mathbf{s}_j, \omega) \mathbf{h}_\nu(\mathbf{s}_j, \omega), \quad (6.11)$$

where the summations run over all the surface elements associated with the given region.

Apparently, the auxilliary boundary charges and currents are determined through the requirement that the potentials should satisfy the customary boundary conditions at the interfaces separating the individual regions. Since the whole procedure has already been comprehensibly and educatively described in the paper by Abajo and Howie [10], we shall restrict ourselves only to those parts, in which the 2D geometry of the present problem might lead to expressions slightly different from those derived in the aforementioned paper. It turns out, however, that the reduced dimensionality affects just the Green's function  $G_\nu$  and its surface derivative  $H_\nu$ , where the latter appears in connection with the boundary conditions for the normal components of the vector potential and the electric displacement.

Let us start with an important remark concerning the evaluation of the potentials and their derivatives at the individual elements  $\Delta\mathbf{s}_i$  constituting the region boundaries. As pointed out earlier, one can not disregard the small-scale variations in the Green's function, nor in its surface derivative

close to the interfaces. Moreover, both these quantities diverge in the  $\mathbf{s}_i \rightarrow \mathbf{s}_j$  limit. Fortunately, one can solve these difficulties by taking the average over the small interface elements

$$G_\nu(\mathbf{s}_i, \mathbf{s}_j, \omega) = \int_{\Delta \mathbf{s}_j} d\mathbf{s} G_\nu(\mathbf{s}_i, \mathbf{s}, \omega) = \frac{i}{4} \int_{\Delta \mathbf{s}_j} d\mathbf{s} H_0^{(1)}(k_\nu |\mathbf{s}_i - \mathbf{s}|), \quad (6.12)$$

$$H_\nu(\mathbf{s}_i, \mathbf{s}_j, \omega) = \int_{\Delta \mathbf{s}_j} d\mathbf{s} \mathbf{n}_{\mathbf{s}_i} \cdot \nabla G_\nu(\mathbf{s}_i, \mathbf{s}, \omega) = \frac{ik_\nu}{4} \int_{\Delta \mathbf{s}_j} d\mathbf{s} \frac{-\mathbf{n}_{\mathbf{s}_i} \cdot (\mathbf{s}_i - \mathbf{s})}{|\mathbf{s}_i - \mathbf{s}|} H_1^{(1)}(k_\nu |\mathbf{s}_i - \mathbf{s}|). \quad (6.13)$$

The divergence in the  $\mathbf{s}_i \rightarrow \mathbf{s}_j$  limit turns out to be analytically integrable after replacing the Hankel functions with their asymptotic expansions for small values of the argument

$$G_\nu(\mathbf{s}_j, \mathbf{s}_j, \omega) \approx \frac{i}{4} \int_{-\frac{L_j}{2}}^{\frac{L_j}{2}} dx \left( 1 + \frac{2i}{\pi} \left[ \ln \left( \frac{k_\nu x}{2} \right) + \gamma \right] \right) = \frac{i}{4} L_j + \frac{1-\gamma}{2\pi} L - \frac{L_j}{2\pi} \ln \left( \frac{k_\nu L_j}{4} \right), \quad (6.14)$$

where  $L_j$  denotes the length of the  $j$ -th interface element. The evaluation of the surface derivative  $H_\nu(\mathbf{s}_j, \mathbf{s}_j)$  may be a little tricky, but following the procedure presented in [10], one finds it to be

$$H_\nu(\mathbf{s}_j, \mathbf{s}_j, \omega) = \pm 2\pi \quad (6.15)$$

which is the same as in 3D. The two possible signs in Equation (6.15) reflect the liberty of choosing whether the interface normal points inside (−) or outside (+) the region in question.

Eventually, by combining together all the boundary conditions one arrives at a system of  $8N$  linear equations for  $8N$  unknowns ( $N$  denotes the total number of surface elements), which can be directly solved either by an iterative method or through the direct inversion of the matrix representing the system. As suggested by Abajo and Howie, the computational time can be significantly reduced by following a procedure, in which instead of inverting the large  $8N \times 8N$  matrix, one separately manipulates several smaller matrices of dimension  $N \times N$ . Once the auxiliary charges and currents are known, the electric and magnetic fields at any point in the space are readily calculated using the above relations.

## 6.2. Modeling of graphene and substrates in BEM

Having prepared the grounds for light scattering calculations in arbitrary geometries, we can turn our attention to the composite plasmonic structure presented in Chapter 5. Apparently, the current formulation of the BEM does not take into account charge and current densities induced at the interfaces due to a presence of 2D crystals like graphene. Fortunately, the electrodynamic response of such planar structures is in many aspects similar to that of a very thin film with a dielectric function constructed in the following way [30]

$$\varepsilon_{3D}(\omega) = 1 + i \frac{\sigma(\omega)}{\varepsilon_0 \omega t}, \quad (6.16)$$

where  $\sigma(\omega)$  is the 2D dynamical conductivity and  $t$  marks the thickness of the layer. The above expression can be derived either by comparing the Fresnel coefficients obtained in Chapter 1 with those for a thin layer sandwiched between two dielectric halfspaces (Novotny and Hecht [28], p. 342)

## 6.2. MODELING OF GRAPHENE AND SUBSTRATES IN BEM

or through a simple model, in which we adopt an assumption that the current density  $\sigma \mathbf{E}$  associated with the 2D crystal is uniformly spread over the whole thickness of the thin film

$$j_{3D}(\omega) = \frac{\sigma(\omega)}{t} \mathbf{E}(\omega). \quad (6.17)$$

The resulting current density  $j_{3D}$  is also directly related to the polarization vector  $\mathbf{P}$  and thus the dielectric properties of the film

$$j_{3D}(\omega) = -i\omega \mathbf{P}(\omega) = -i\omega \varepsilon_0 [\varepsilon_{3D}(\omega) - 1] \mathbf{E}(\omega). \quad (6.18)$$

Combining those two equations, one recovers the above approximate expression for the dielectric function.

The last issue, we shall address before proceeding with the actual light scattering calculations, concerns the shape of the used external electromagnetic field. The semi-analytical technique introduced in the previous chapter is naturally able to cope with the infinite extent of the superstrate-substrate interface and thus the whole structure can be illuminated by a single plane wave without any intrusive effects. That does not hold for the BEM with a finite simulation region because of the diffraction effects at its edges. One might suppress those artifacts by including a larger portion of the superstrate-substrate interface into the calculation, but that would also mean a substantial increase in the number of the surface elements and hence even larger increase in the computation time. This can be avoided by using a spatially confined beam instead of an infinite plane wave as the illumination source. The most common and also the one we shall employ is the Gaussian beam.

Summoning the expression for the vector potential of a single plane wave with an amplitude  $E_0$  and a wavevector  $k$ , propagating under an angle  $\theta$  with respect to the  $x$ -axis

$$\mathbf{A}(\theta) = -\frac{i}{\omega} \mathbf{E}_0 e^{ik(x \cos \theta + z \sin \theta)}, \quad \mathbf{E}_0 = E_0 (\sin \theta, -\cos \theta), \quad (6.19)$$

the vector potential of a Gaussian beam traveling in a certain direction  $\theta_0$  is calculated as a superposition of an infinite number of plane waves with a gaussian angular distribution centered around  $\theta_0$  [22]

$$\mathbf{A}_{\text{Gauss}}(\theta_0) = -\frac{i E_0}{\omega} \int_{\theta_0 - \frac{\pi}{2}}^{\theta_0 + \frac{\pi}{2}} d\theta \exp \left[ -\frac{k^2 w^2}{4} (\theta - \theta_0)^2 \right] e^{ik(x \cos \theta + z \sin \theta)} (\sin \theta, -\cos \theta). \quad (6.20)$$

The parameter  $w$  prescribes, how much the angular distribution is smeared, and as we shall see, it also determines the spatial confinement of the beam. Changing the integration variable to  $t = \theta - \theta_0$  and assuming the angular distribution is sufficiently sharp so that the integration limits can be extended to infinity, the vector potential acquires the following integral form

$$\mathbf{A}_{\text{Gauss}}(\theta_0) = -\frac{i E_0}{\omega} \int_{-\infty}^{\infty} dt \exp \left( -\frac{k^2 w^2}{4} t^2 \right) e^{ik(x' \cos t + z' \sin t)} [\sin(t + \theta_0), -\cos(t + \theta_0)], \quad (6.21)$$

where we have defined new spatial coordinates  $x' = x \cos \theta_0 + z \sin \theta_0$  and  $z' = -x \sin \theta_0 + z \cos \theta_0$ . Apparently, the above integral is still too complicated to be calculated analytically, but one can improve the situation by replacing the sines and the cosines in the second exponential factor with the first few terms of their Taylor's expansions. Provided the first exponential factor approaches the zero

## 6. CALCULATIONS BASED ON THE BOUNDARY ELEMENT METHOD

fast enough, one is entitled to take into account only the terms up to the second power in  $t$  and the previous equation becomes

$$\mathbf{A}_{\text{Gauss}}(\theta_0) = -\frac{i E_0}{\omega} \int_{-\infty}^{\infty} dt \exp \left[ -\left( \frac{k^2 w^2}{4} + \frac{i k x'}{2} \right) t^2 \right] e^{i k z' \sin t + i k x'} [\sin(t + \theta_0), -\cos(t + \theta_0)], \quad (6.22)$$

The solution to integrals of this form can be found in tables (Gradshteyn [14], p. 504-505)

$$\int_{-\infty}^{\infty} dx e^{-(ax^2+bx+c)} \sin(px+q) = -\sqrt{\frac{\pi}{a}} \exp\left(\frac{b^2-p^2}{4a} - c\right) \sin\left(\frac{pb}{2a} - q\right), \quad (6.23)$$

$$\int_{-\infty}^{\infty} dx e^{-(ax^2+bx+c)} \cos(px+q) = \sqrt{\frac{\pi}{a}} \exp\left(\frac{b^2-p^2}{4a} - c\right) \cos\left(\frac{pb}{2a} - q\right), \quad (6.24)$$

and one eventually obtains, after some manipulations, the final expression for the vector potential of the Gaussian beam

$$\mathbf{A}_{\text{Gauss}}(\theta_0) = -\frac{2i \sqrt{\pi} E_0}{\omega k w} \frac{e^{i k x'}}{\kappa} \exp\left(-\frac{z'^2 + \frac{1}{k^2}}{\kappa w^2}\right) \left[ \sin\left(\frac{2i z'}{\kappa k w^2} + \theta_0\right), -\cos\left(\frac{2i z'}{\kappa k w^2} + \theta_0\right) \right], \quad (6.25)$$

where  $\kappa = 1 + \frac{2i x'}{k w^2}$ . As mentioned earlier, the parameter  $w$  evidently controls the spatial confinement of the beam.

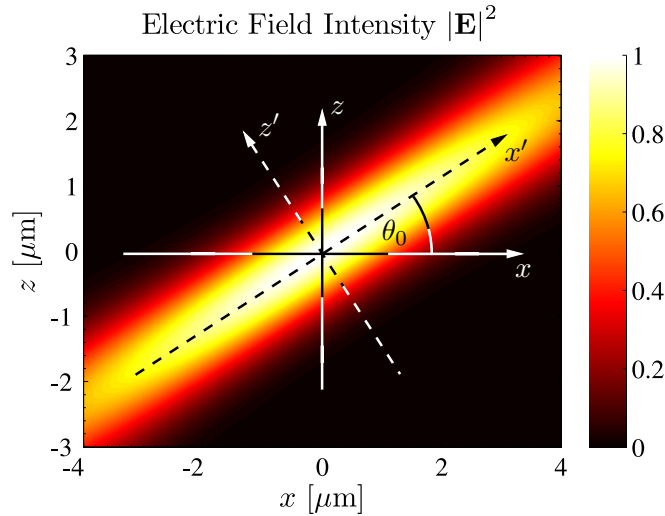


Figure 6.1: The spatial profile of the intensity of the electric field  $|\mathbf{E}|^2$  within the Gaussian beam. The beam propagates in the positive direction of the  $x'$ -axis.

Since the discussion on the properties of Gaussian beams can be found in many textbooks, we refer the reader for further information to Novotny [28], Chap. 3. For clarity, we show in Figure 6.1 the mutual orientation of the primed and unprimed spatial coordinates together with the map of the intensity of the electric field within the propagating Gaussian beam.

### 6.3. BEM calculations

Relying on the formalism presented in [10] and employing the above modifications for problems with a 2D geometry, an algorithm for light scattering simulations based on the boundary element method has been developed. The program operates fully within the framework of Matlab, a commercial software from the Mathworks company ([www.mathworks.com](http://www.mathworks.com)). Although programs in Matlab tend to run slower than their equivalents written in other languages, it is partially compensated through its user-friendly environment accompanied by an extensive library of built-in functions and effective debugging tools.

To verify the proper and correct functionality of the created program, a series of benchmark simulations with known analytical solutions has been performed. As an example, we have picked the classical problem of scattering of light from an infinitely long cylinder embedded in a homogenous medium. Figure 6.2 shows the comparison between the exact analytical solution provided by the Mie theory [7] and results calculated by the BEM and the transformation optics method. Meanwhile the latter captures only the qualitative aspects of the cylinder's plasmonic resonance, the boundary element method reproduces it perfectly even for a modest number of discretization points.

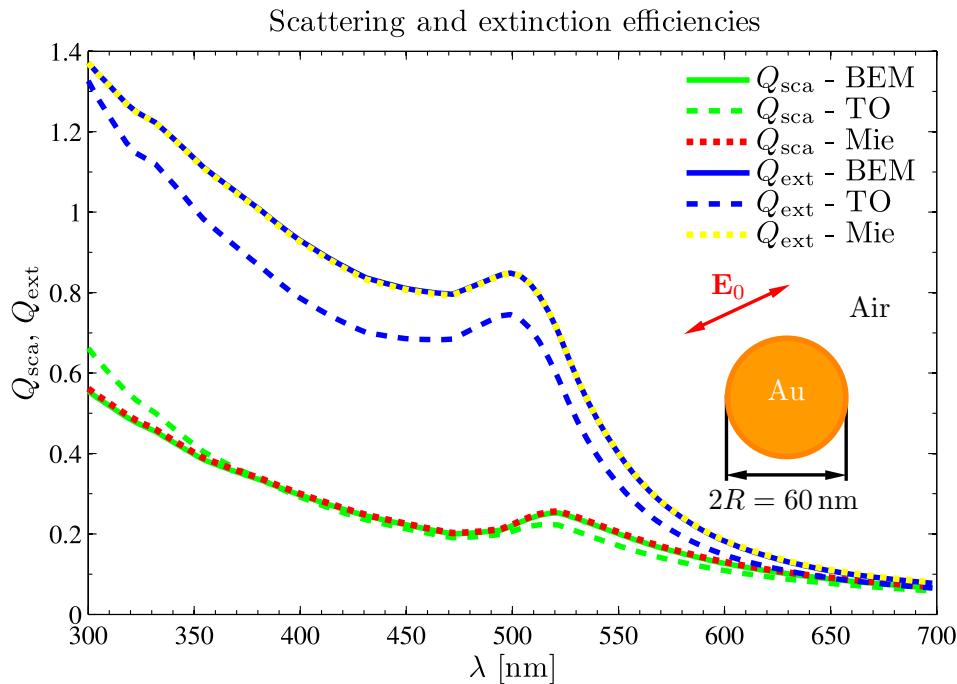


Figure 6.2: Scattering and extinction efficiencies of an infinitely long golden cylinder of radius  $R = 30$  nm surrounded by air. Unlike the transformation optics method, the curves calculated by the BEM correspond perfectly with the analytical solution provided by the Mie theory. The interface between the cylinder and air has been discretized into 100 elements.

For completeness, the extinction efficiency reflects, how much power has been removed from the incident beam due to the presence of the metallic cylinder and it can be calculated either as the sum of scattering and absorption efficiencies, where the latter represents the amount of power dissipated within the cylinder, or by means of the optical theorem (Bohren and Huffman [7], p. 73), which states that the extinction efficiency depends solely on the scattering amplitude in the forward direction (original direction of the incident plane wave).

Once we are confident that the program produces correct and physically reasonable results, nothing hinders us from utilizing BEM for the calculations investigating the mutual interaction between graphene and ordinary plasmonic structures. Recalling that the development of the whole program

## 6. CALCULATIONS BASED ON THE BOUNDARY ELEMENT METHOD

was motivated by the need to find a suitable and reliable technique, which would either confirm or refute the hypothesis proposed in the preceding chapter, we present in Figure 6.3 the map of the intensity of the electric field in the vicinity of a golden cylinder situated on a dielectric substrate covered by a single graphene sheet. Except the cylinder radius, the parameters of the calculation are the same as in Figure 5.6.

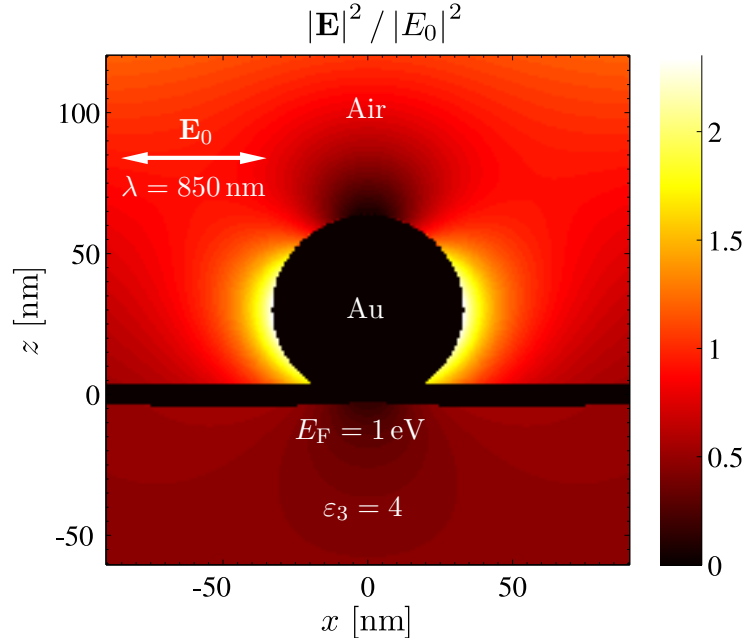


Figure 6.3: The spatial profile of the electric field intensity  $|\mathbf{E}|^2$  within a hybrid structure composed of a golden cylinder with a radius  $R = 30$  nm lying on the top of a dielectric substrate  $\epsilon_3 = 4$  covered by electrostatically doped graphene ( $E_F = 1$  eV). A reasonable convergence was achieved for approximately 800 discretization points.

The distribution of the electric field appears to be similar to that calculated by means of the transformation optics method, including the magnitude of the enhancement factor, although the latter predicts a slightly higher intensity close to the touching point between the cylinder and the substrate. Importantly, the blackened regions do not represent the actual boundaries of the individual structures, but they are created artificially to suppress spikes in the intensity of the electric fields, which occur as the result of the discretization (more precisely due to the divergence of the Green's function, when its argument tends to zero).

Encouraged by the agreement between those two approaches, the next series of calculations was aimed to reproduce the spectral dependences of the scattering efficiency and the phase shift of the induced dipole moment with respect to the excitation field for various values of the doping level in graphene. During these simulations, the ability to control the spatial confinement of the incident beam proved to be of great merit, because the vanishing thickness of the graphene sheet (we used rather large value  $t = 3$  nm) forces us to use very fine discretization and the smaller is the portion of the graphene sheet we have to include into the simulation region, the shorter computation time is required to obtain the results.

The spectral dependences of the scattering efficiency plotted in Figure 6.4 represent a certain compromise between the accuracy of the model and the required computation time. In order to keep the number of interface elements small, the graphene extends only one micron in each direction from the golden cylinder and the width of incident beam is set to be approximately one half of the created graphene "ribbon". Even though such configuration resembles only partially the original one, the presented dependences indicate that the employment of this model is justifiable.

### 6.3. BEM CALCULATIONS

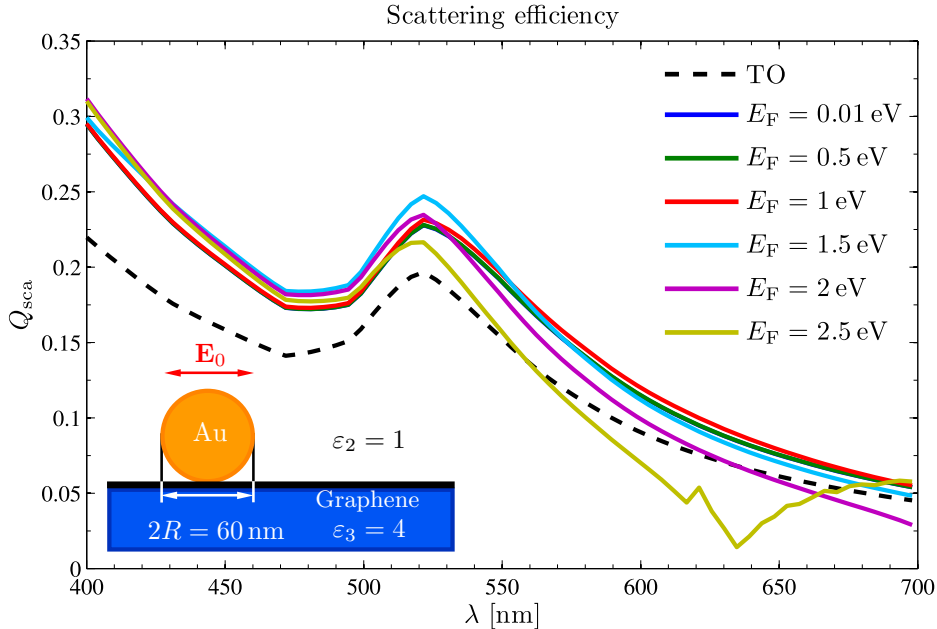


Figure 6.4: The scattering efficiency of the structure presented in Chapter 5 as a function of the wavelength for various values of the doping level in graphene. The graphene is modeled as a ribbon of a finite width and the whole system is illuminated by a highly focused Gaussian beam. The interfaces have been discretized into 1700 elements.

Along with the curves calculated using the BEM (solid lines), we present for comparison also one of the spectral dependences obtained by means of the transformation optics method (dashed line). Apparently, the BEM simulations are in concordance with those obtained earlier, in the sense that the variation of the doping level in graphene brings no changes into the dynamical response of the cylinder.

The substitution of the graphene sheet by a ribbon becomes especially important once the Fermi energy reaches the threshold value, at which photons cease to decay directly into electron-hole pairs. The finite dimensions of the graphene ribbon provide the additional momentum necessary to overcome the wavevector mismatch between photons and plasmon polaritons, resulting in the antenna-like behaviour observed commonly in ordinary metals. The plasmonic modes of the cylinder and the newly formed graphene antenna can couple to each other, leading to strange features in the spectra. Although we hoped to suppress these effects in the present structure by decreasing the width of the incident beam so that the graphene would appear to the source as infinite, the feature observed at the wavelength  $\lambda = 630$  nm for the doping level  $E_F = 2.5$  eV (yellow line) speaks otherwise. It becomes even more prominent, when one looks at the spectral dependences of the phase shift between the induced dipole moment and the driving electromagnetic force plotted in Figure 6.5.

The results of the BEM calculations prove to be in correspondence with those acquired through the semi-analytical technique based on conformal transformations between various geometries, but before making the final conclusion regarding the possibility to control the dynamical response of a single plasmonic antenna through the electrostatic doping in graphene, the author has decided to perform another series of simulations with a slightly modified geometry of the metallic antenna (see Figure 6.6).

The transition from the cylindrical to an elongated rectangular antenna is motivated by the substantial increase in the contact surface area between the antenna and the substrate, which might enhance their mutual interaction. The perceptible change in the size of the whole structure reflects the current possibilities of graphene doping. Generally, the plasmonic resonance of a metallic antenna

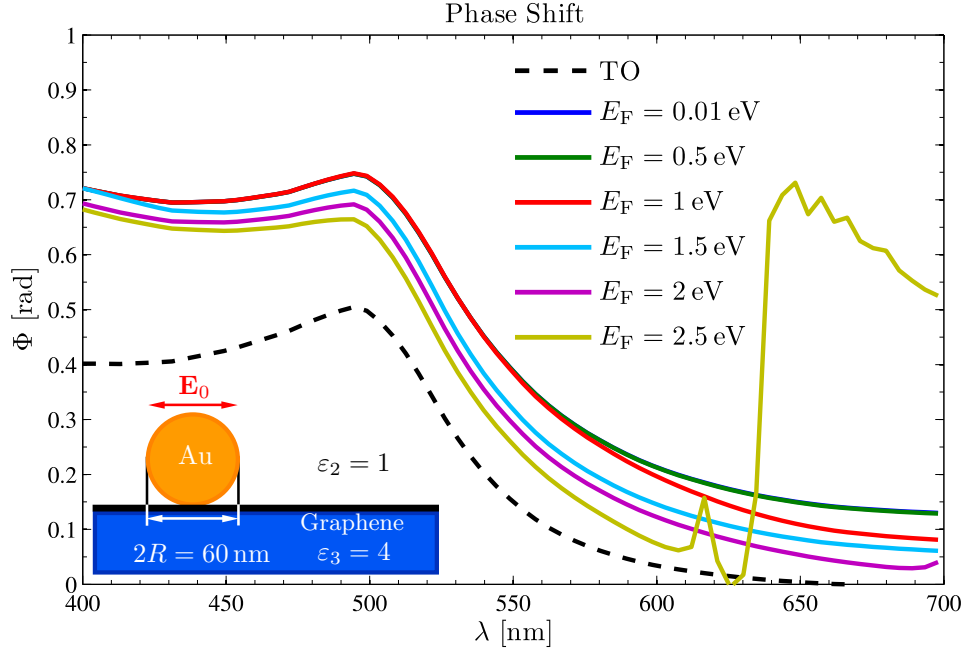


Figure 6.5: The phase shift  $\Phi$  of the dipole moment induced within the golden cylinder as a function of the wavelength  $\lambda$  for different values of the Fermi energy  $E_F$  in graphene. The abrupt change in the phase observed at  $\lambda = 630$  nm for  $E_F = 2.5$  eV (yellow line) originates in the finite extent of the graphene sheet. Parameters of the calculation are the same as in Figure 6.4

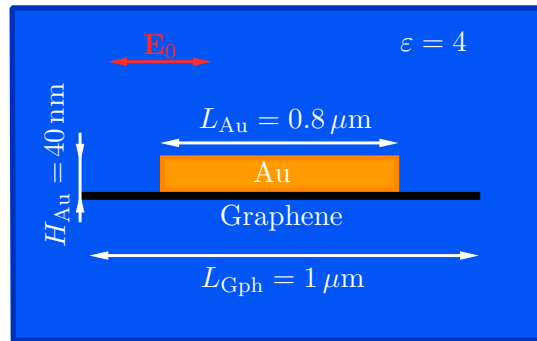


Figure 6.6: Schematic drawing of a modified hybrid structure with a larger contact surface area between the golden antenna and the graphene ribbon. The plasmonic resonance frequency of the system falls within the near infrared part of the spectrum.

is being shifted to longer wavelengths as its size is increased, which reduces the range of doping level in graphene one has to be able to achieve in order to switch between the different regimes of its conductivity. The proportions of the new plasmonic structure and the refractive index of its surroundings push the spectral position of the plasmonic resonance up to 4 microns so that the interval of Fermi energies needed to ensure the functionality of such device shrinks to  $E_F = 0.1 - 0.75$  eV, which appears to be a reasonable value considering the current state of the gating technology.

By embedding the whole structure in a single homogenous medium with permittivity  $\epsilon = 4$  we get rid of the superstrate-substrate interface so that the source of the external electromagnetic field can

### 6.3. BEM CALCULATIONS

assume the form of a single plane wave. Figures 6.7 and 6.8 show the spatial profiles of the electric field intensity in the vicinity of the hybrid antenna and near the edge of its golden constituent.

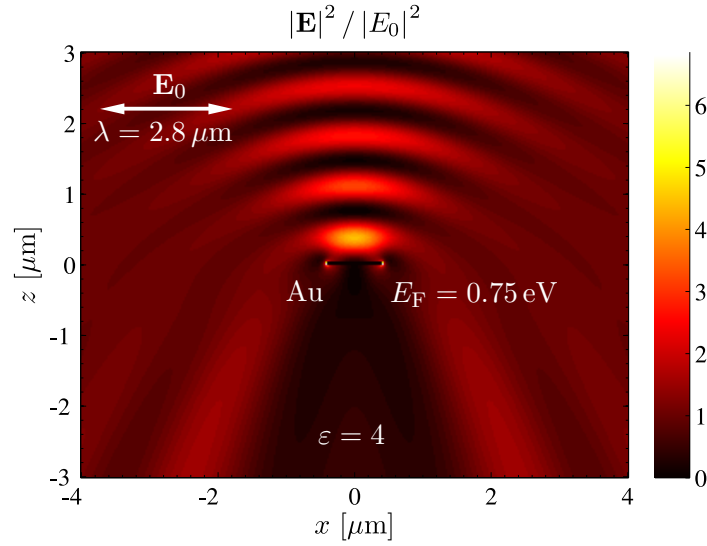


Figure 6.7: The map of the electric field intensity  $|\mathbf{E}|^2$  in the vicinity of a plasmonic antenna embedded in a homogenous medium with permittivity  $\varepsilon = 4$ . The geometry of the antenna is outlined in Figure 6.6.

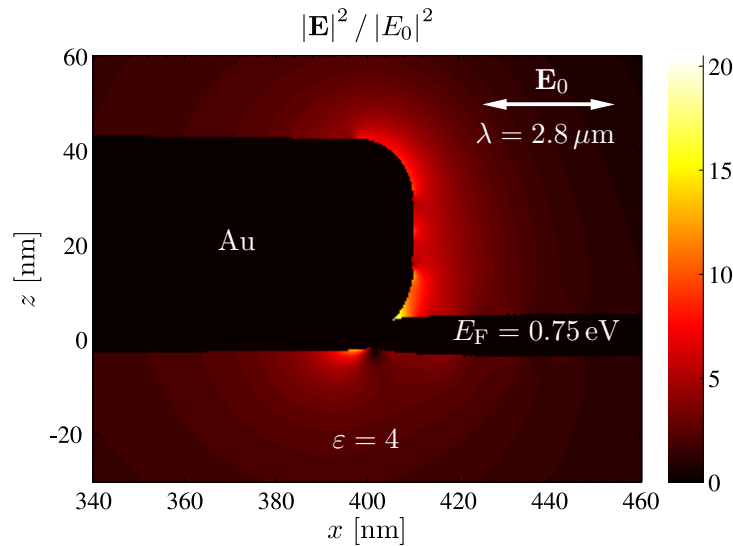


Figure 6.8: The map of the electric field intensity  $|\mathbf{E}|^2$  at the edge of the golden antenna constituting the hybrid structure from Figure 6.6. The large electric field enhancement indicates a strong interaction between the golden antenna and the graphene ribbon.

As pointed out earlier, the blackened regions do not represent the real boundaries of the structures, but they are created artificially to suppress artifacts originating in the discretization of the interfaces. The distribution of the electric field and its enhancement at the lower edge of the golden antenna manifest the increased interaction between the two materials constituting the hybrid structure. The question, whether it suffices to induce changes in the dynamical response of the system, or better to control it through gating voltage, can be answered by running a series of calculations similar to those performed for the golden cylinder.

## 6. CALCULATIONS BASED ON THE BOUNDARY ELEMENT METHOD

The spectral dependences of the scattering (dashed lines) and extinction (solid lines) efficiencies of the hybrid antenna for various values of the doping level in graphene are plotted in Figure 6.9. Clearly, the increase in the density of free charge carriers in graphene has practically no effect on the response of the system, which is further confirmed by looking at the phase shift between dipole moment induced within the golden antenna and the driving electromagnetic force (see Figure 6.10). Notice the slight drop in the scattering efficiency (red line), when the structure is electrostatically doped to  $E_F = 0.3$  eV, caused by the resonant coupling between the golden and graphene antennas.

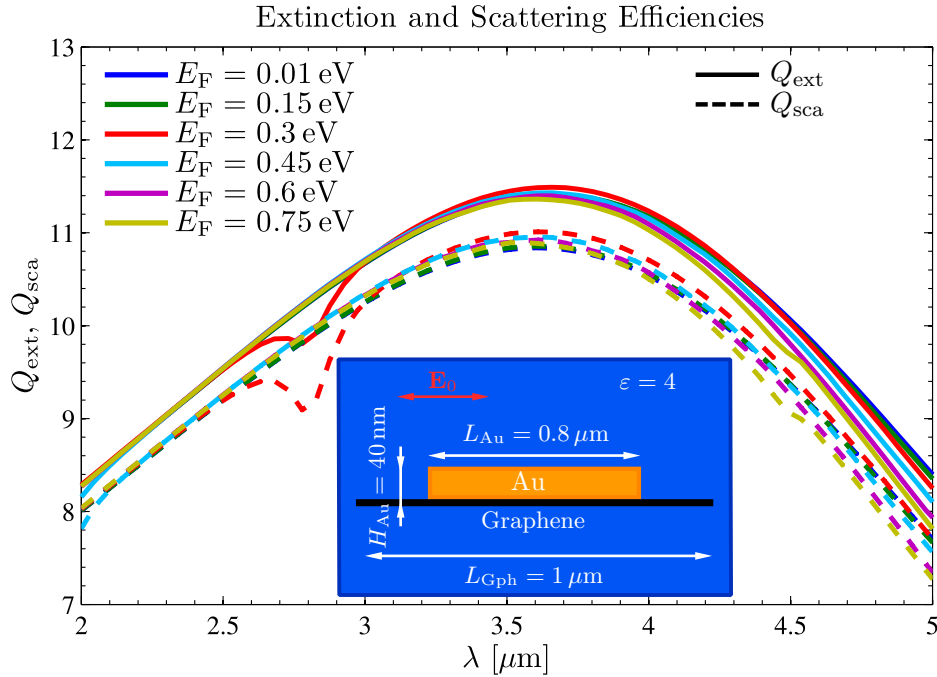


Figure 6.9: The scattering (dashed) and extinction (solid) efficiencies  $Q_{\text{sca}}$  and  $Q_{\text{ext}}$  of the hybrid antenna as a function of the wavelength for various values of the Fermi level in graphene. Except the slight drop in the efficiencies for  $E_F = 0.3$  eV (red line) caused by a resonant coupling between the golden and graphene antenna, the response of the systems remains unchanged as the density of free charge carriers in graphene is increased. The boundaries of the individual structures have been discretized into 2700 interface elements.

Relying on the above simulations, the author has eventually come to the conclusion that the proposed control over the dynamical response of single plasmonic structures made of noble metals by means of electrostatically doped graphene proves to be inefficient. To enhance this effect, one might consider utilization of more complex structures with a superb sensitivity to the ambient environment or exploit the coupling between the ordinary and graphene antennas, which seems to have, according to Figures 6.4 and 6.9, an interesting impact on their electrodynamic response.

### 6.3. BEM CALCULATIONS

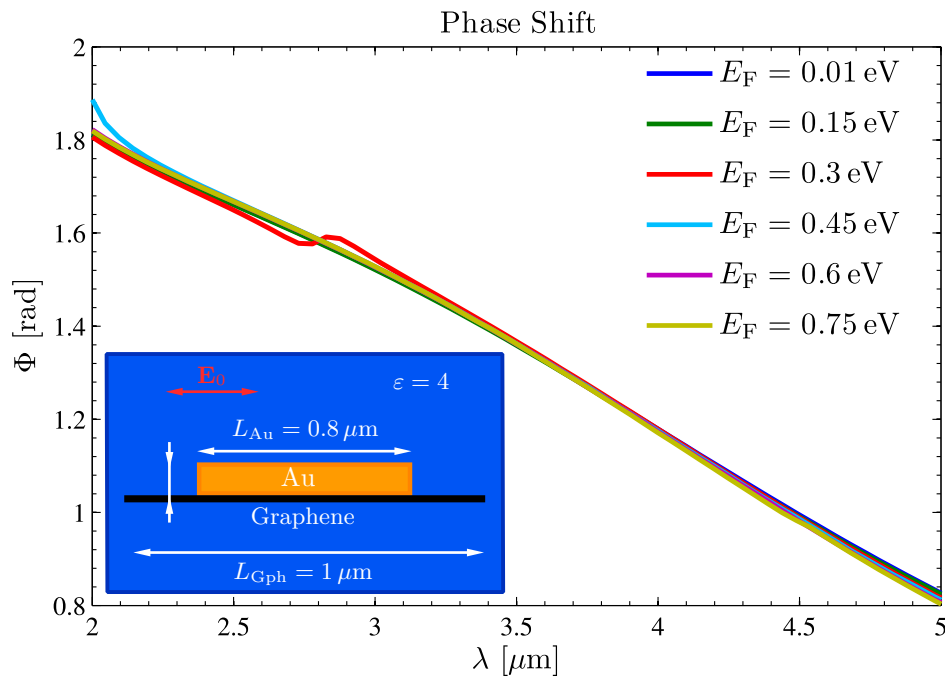


Figure 6.10: The phase shift between the dipole moment induced within the golden antenna and the external electromagnetic field as a function of the wavelength for various values of the doping level in graphene. The parameters of the simulation are the same as in Figure 6.9.

## 7. Conclusion

Graphene has drawn attention of many researchers in the past years, including those concerned with nanophotonics and plasmonics. The main reason for this increased interest resides probably in the tunable electrodynamic response of graphene. In this thesis, the author attempted to estimate theoretically the strength of the interaction between electrostatically doped graphene and ordinary plasmonic structures made of noble metals and to assess how the interaction changes when the doping level is varied.

The theory behind graphene and its response to electromagnetic radiation is rather extensive and comprises many parts of physics including quantum mechanics, solid state physics and electrodynamics. The author took the liberty to create a compact and relatively short text, which would allow the reader to follow the key steps in the derivation of the graphene's dynamical conductivity and to grasp its main features including the influence of interband transitions and non-local effects.

Pursuing one of the goals of the thesis, to propose an experiment, which would demonstrate the ability of graphene to control the response of surrounding plasmonic structures, the author presented a hypothetical design of a hybrid structure consisting of an array of ordinary plasmonic antennas positioned on the top of a dielectric substrate covered by an electrostatically gated graphene. It was suggested that inhomogeneously doped graphene might induce a slight phase shift in the dipole moments of the individual antennas, leading to the anomalous refraction. Furthermore, by varying the voltage between the graphene and the gating electrode, one would be able to tune the deviation angle of the anomalous light ray.

Most of the effort was focused on the search for a suitable technique, which would allow us to investigate the influence of the varying density of free charge carriers in graphene on surrounding metallic structures. The author decided to employ the transformation optics method, which enables to find a solution within the quasistatic approximation to problems with a complex geometry through a transition into a space, where the geometry assumes a more appealing form.

A structure consisting of an infinitely long metallic cylinder placed on the top of a dielectric substrate covered by a single graphene sheet and illuminated by a plane wave was chosen as the object of the investigation. Utilizing the method of conformal transformations, analytical expressions for the distribution of the electrostatic potential within that structure were derived. Subsequently, the scattering properties of the metallic cylinder were calculated using the formalism of the far-field Green's dyadic functions.

In order to estimate, whether the variations in the doping level of graphene affect the plasmonic resonance of the metallic cylinder, a series of calculations for different values of the Fermi energy were performed. The absence of any changes in the response of the system with the varying density of free charge carriers in graphene indicates that either the transformation optics method is not suitable for such simulations or the changes in the graphene's conductivity are not large enough to cause any perceptible shift in the plasmonic resonance of the cylinder.

The author decided to verify the preceding findings by another, fully numerical boundary element method (BEM), in which the solution is expressed in terms of surface integrals over the interfaces between regions with different dielectric properties. Unlike the transformation optics method, the BEM takes into account the retardation effects and is applicable to arbitrary geometries. Performing the same series of calculations as before, the spectral dependences of the scattering efficiency and the phase shift between the dipole moment induced within the metallic cylinder and the driving electromagnetic force for various doping levels in graphene were obtained. Importantly, the results of the BEM simulations were in concordance with those acquired by the method of conformal transformations.

Before making the final conclusion regarding the possibility to control the response of metallic structures through electrostatically doped graphene, another series of calculations were performed, but this time for a structure with a substantially larger contact surface area between the metallic

antenna and graphene. Once again, the variations in the density of free charge carriers in graphene proved to have no effect on the response of the metallic antenna.

The results of the simulations presented in this thesis suggest that one could improve the situation by considering an arrangement of plasmonic structures more sensitive to the ambient environment or exploiting the resonant coupling between ordinary antennas and those made of graphene.

# Appendix A

The starting point of the derivation of the quantum-mechanical Liouville equation is the time-dependent Schrödinger equation for a state  $|\psi\rangle$

$$\hat{H}|\psi\rangle = i\hbar \frac{\partial}{\partial t}|\psi\rangle. \quad (7.1)$$

By the assumption  $|\psi\rangle = \hat{\rho}|\varphi\rangle$ , the above equation reads

$$\hat{H}\hat{\rho}|\varphi\rangle = i\hbar \frac{\partial}{\partial t}\hat{\rho}|\varphi\rangle = i\hbar \frac{\partial \hat{\rho}}{\partial t}|\varphi\rangle + i\hbar \hat{\rho} \frac{\partial}{\partial t}|\varphi\rangle. \quad (7.2)$$

Requiring that the state  $|\varphi\rangle$  should satisfy the time-dependent Schrödinger equation as well and applying the density operator  $\hat{\rho}$  on its both sides leads to

$$\hat{\rho}\hat{H}|\varphi\rangle = i\hbar \hat{\rho} \frac{\partial}{\partial t}|\varphi\rangle. \quad (7.3)$$

Clearly, by subtracting Equation (7.3) from Equation (7.2) one recovers the quantum-mechanical Liouville equation.

$$i\hbar \frac{\partial \hat{\rho}}{\partial t} = [\hat{H}, \hat{\rho}]. \quad (7.4)$$



# Appendix B

The method of stationary phase represents a useful tool for the approximate evaluation of various integrals occurring in the light scattering problems, one of them being the finding of the far-field expression for the dyadic Green's function presented in Chapter 5. Let us consider an integral of the form

$$F(p) = \int_{-\infty}^{\infty} dt f(t) e^{ipg(t)}, \quad (7.5)$$

where  $f(t)$ ,  $g(t)$  are well-behaving functions of the real variable  $t$ . Apparently, the parameter  $p$  determines how rapidly the integrand oscillates with varying  $t$  and in the present physical situation, it can be associated with the dimensionless distance  $kr = k\sqrt{x^2 + z^2}$  from the origin of the coordinate system.

Assuming  $f(t)$  is a slowly varying function of  $t$  and the parameter  $p$  is very large, the individual contributions to the above integral will tend to cancel each other out, with exception of intervals, in which  $g(t)$  is stationary. Relying on the derivation presented in Mandel and Wolf [21] (Chap. 3.3), the asymptotic approximation of the integral in Equation (7.5) reads

$$F(p) \underset{p \rightarrow \infty}{\approx} \sum_j \left[ \frac{2\pi}{p|g''(t_j)|} \right]^{1/2} f(t_j) e^{ipg(t_j)} e^{\pm i\pi/4}, \quad (7.6)$$

where the sum runs over all the integration points  $t_j$ , in which  $g'(t) = 0$  (the prime denotes the derivative with respect to  $t$ ) and the sign in the last exponential factor is taken according to whether the second derivative of  $g(t)$  is positive (+) or negative (-).

To demonstrate the applicability of the stationary phase method to the present problem of finding the angular distribution of the electromagnetic field, we shall use it to derive the approximate asymptotic expression for the 2D Green's function given by Equation 5.75

$$G_0(\mathbf{r}, \mathbf{r}') = \frac{i}{4} H_0^{(1)}(k|\mathbf{r} - \mathbf{r}'|) = \frac{i}{4\pi} \int_{-\infty}^{\infty} dk_x \frac{e^{ik_x(x-x') + ik_z|z-z'|}}{k_z}, \quad (7.7)$$

where  $H_0^{(1)}$  stands for the zeroth order Hankel function of the first kind and  $k_z = \sqrt{k^2 - k_x^2}$  is the wavevector component in the  $z$ -direction. In the far-field region, it is more convenient to use the dimensionless radial distance  $kr = k\sqrt{x^2 + z^2}$  and scattering direction  $s_x = \frac{x}{r}$ ,  $s_z = \pm\sqrt{1 - s_x^2}$  instead of the cartesian coordinates  $x$  and  $z$

$$G_0(s_x, s_z, \mathbf{r}') = \frac{i}{4\pi} \int_{-\infty}^{\infty} dk_x \frac{e^{-ik_x x'} e^{-ik_z z' \text{sgn}(s_z r - z')}}{k_z} e^{ikr \left( \frac{k_x}{k} s_x + \frac{k_z}{k} |s_z| \right)}. \quad (7.8)$$

Apparently, the sources are implicitly assumed to be confined within a small region around the origin of the coordinate system.

Identifying the normalized wavevector component  $\frac{k_x}{k}$ , resp. the dimensionless radial distance  $kr$  as the variable  $t$ , resp. the parameter  $p$  from Equation (7.5), the above integral acquires the form suitable for the utilization of the stationary phase method

$$G_0(s_x, s_z, \mathbf{r}') = \frac{i}{4\pi} \int_{-\infty}^{\infty} dt \underbrace{\frac{e^{-ikt x'} e^{-ik\sqrt{1-t^2} z' \text{sgn}(s_z r - z')}}{\sqrt{1-t^2}}}_{f(t)} \underbrace{e^{ikr (ts_x + \sqrt{1-t^2} |s_z|)}}_{e^{ikr g(t)}}. \quad (7.9)$$

The stationary points  $t_j$  correspond to zeros in the first derivative of  $g(t)$  with respect to  $t$

$$\frac{dg(t)}{dt} = s_x - \frac{t}{\sqrt{1-t^2}}|s_z| = 0. \quad (7.10)$$

The above equation has only one solution  $t_0 = s_x$  with  $g(t_0) = s_x^2 + s_z^2 = 1$ . According to Equation (7.6), we shall also need the second derivative of  $g(t)$  evaluated at the stationary point  $t_0$

$$\left. \frac{d^2g(t)}{dt^2} \right|_{t=t_0} = -\frac{|s_z|}{(1-t_0^2)^{3/2}} = -\frac{1}{s_z^2}. \quad (7.11)$$

Finally, by inserting all the above expressions into Equation (7.6), one obtains the asymptotic approximation for the 2D Green's function

$$G_0(s_x, s_z, \mathbf{r}') = \frac{i}{4} \left( \frac{2}{\pi k r} \right)^{1/2} e^{-i k s_x x'} e^{-i k s_z z' \operatorname{sgn}(s_z r - z')} e^{i k r} e^{-i\pi/4}, \quad (7.12)$$

corresponding to an outgoing cylindrical wave.

The above procedure can be readily extended to the integrals involved in the angular distribution of the electromagnetic field determined by the dyadic Green's function.

# Bibliography

- [1] ALLAIN, P., AND FUCHS, J. Klein tunneling in graphene: optics with massless electrons. *The European Physical Journal B - Condensed Matter and Complex Systems* 83, 3 (Oct. 2011), 301–317.
- [2] ANDO, T. Theory of electronic states and transport in carbon nanotubes. *Journal of the Physical Society of Japan* 74, 3 (2005), 777–817.
- [3] ANDO, T. Screening effect and impurity scattering in monolayer graphene. *Journal of the Physical Society of Japan* 75, 7 (2006), 074716.
- [4] ASHCROFT, N. W., AND MERMIN, D. N. *Solid state physics*, 1 ed. Thomson Learning, Toronto, Jan. 1976.
- [5] AUBRY, A., LEI, D. Y., FERNÁNDEZ-DOMÍNGUEZ, A. I., SONNEFRAUD, Y., MAIER, S. A., AND PENDRY, J. B. Plasmonic light-harvesting devices over the whole visible spectrum. *Nano Letters* 10, 7 (2010), 2574–2579.
- [6] BAE, S., KIM, H., LEE, Y., XU, X., PARK, J.-S., ZHENG, Y., BALAKRISHNAN, J., LEI, T., RI KIM, H., SONG, Y. I., KIM, Y.-J., KIM, K. S., OZYILMAZ, B., AHN, J.-H., HONG, B. H., AND IJIMA, S. Roll-to-roll production of 30-inch graphene films for transparent electrodes. *Nat Nano* 5, 8 (Aug. 2010), 574–578.
- [7] BOHREN, C. F., AND HUFFMAN, D. R. *Absorption and Scattering of Light by Small Particles*. Wiley-VCH, Apr. 1998.
- [8] CINCOTTI, G., GORI, F., SANTARSIERO, M., FREZZA, F., FURNO, F., AND SCHETTINI, G. Plane wave expansion of cylindrical functions. *Optics Communications* 95, 4-6 (Jan. 1993), 192–198.
- [9] COOPER, D. R., D’ANJOU, B., GHATTAMANENI, N., HARACK, B., HILKE, M., HORTH, A., MAJLIS, N., MASSICOTTE, M., VANDSBURGER, L., WHITEWAY, E., AND YU, V. Experimental review of graphene. *ArXiv e-prints* (Oct. 2011).
- [10] DE ABAJO, F. J. G., AND HOWIE, A. Retarded field calculation of electron energy loss in inhomogeneous dielectrics. *Phys. Rev. B* 65, 11 (Mar. 2002), 115418.
- [11] EHRENREICH, H., AND COHEN, M. H. Self-consistent field approach to the many-electron problem. *Phys. Rev.* 115 (Aug 1959), 786–790.
- [12] FALKOVSKY, L. A., AND VARLAMOV, A. A. Space-time dispersion of graphene conductivity. *The European Physical Journal B - Condensed Matter and Complex Systems* 56, 4 (Apr. 2007), 281–284–284.
- [13] FANO, U. Description of States in Quantum Mechanics by Density Matrix and Operator Techniques. *Reviews of Modern Physics* 29 (Jan. 1957), 74–93.
- [14] GRADSHTEYN, I. S., AND RYZHIK, I. M. *Table of Integrals, Series and Products*, 2nd ed. Academic Press Inc.
- [15] GRIFFITHS, D. J. *Introduction to Quantum Mechanics (2nd Edition)*, 2nd ed. Pearson Prentice Hall, Apr. 2004.
- [16] HWANG, E. H., AND DAS SARMA, S. Dielectric function, screening, and plasmons in two-dimensional graphene. *Phys. Rev. B* 75 (May 2007), 205418.

## BIBLIOGRAPHY

- [17] JABLAN, M., BULJAN, H., AND SOLJAČIĆ, M. Plasmonics in graphene at infrared frequencies. *Phys. Rev. B* 80 (Dec 2009), 245435.
- [18] KOPPENS, F. H. L., CHANG, D. E., AND GARCÍA DE ABAJO, F. J. Graphene plasmonics: A platform for strong light-matter interactions. *Nano Letters* 11, 8 (2011), 3370–3377.
- [19] KRAVETS, V. G., SCHEDIN, F., JALIL, R., BRITNELL, L., NOVOSELOV, K. S., AND GRIGORENKO, A. N. Surface hydrogenation and optics of a graphene sheet transferred onto a plasmonic nanoarray. *The Journal of Physical Chemistry C* 116, 6 (2012), 3882–3887.
- [20] MAIER, S. A. *Plasmonics: Fundamentals and Applications*, 1 ed. Springer, May 2007.
- [21] MANDEL, L., AND WOLF, E. *Optical Coherence and Quantum Optics*, 1 ed. Cambridge University Press, Sept. 1995.
- [22] MARADUDIN, A., MICHEL, T., MCGURN, A., AND MÄKONDEZ, E. Enhanced backscattering of light from a random grating. *Annals of Physics* 203, 2 (1990), 255 – 307.
- [23] MARCONCINI, P., AND MACUCCI, M. The k.p method and its application to graphene, carbon nanotubes and graphene nanoribbons: the Dirac equation. *ArXiv e-prints* (May 2011).
- [24] MERMIN, N. D. Lindhard dielectric function in the relaxation-time approximation. *Phys. Rev. B* 1 (Mar 1970), 2362–2363.
- [25] MIHAILA, B. Lindhard function of a d-dimensional Fermi gas. *ArXiv e-prints* (Nov. 2011).
- [26] MIKHAILOV, S. A., AND ZIEGLER, K. New electromagnetic mode in graphene. *Phys. Rev. Lett.* 99 (Jul 2007), 016803.
- [27] NOVOSELOV, K. S., FAL'KO, V. I., COLOMBO, L., GELLERT, P. R., SCHWAB, M. G., AND KIM, K. A roadmap for graphene. *Nature* 490, 7419 (Oct. 2012), 192–200.
- [28] NOVOTNY, L., AND HECHT, B. *Principles of Nano-Optics*. Cambridge University Press, June 2006.
- [29] SAITO, R., DRESSELHAUS, G., AND DRESSELHAUS, M. S. *Physical properties of carbon nanotubes*. Imperial College Press, 1998.
- [30] SERNELIUS, B. Graphene as a strictly 2D sheet or as a film of small but finite thickness. *Graphene* 1 (2012), 21–25.
- [31] VAKIL, A., AND ENGHETA, N. Transformation optics using graphene. *Science* 332, 6035 (June 2011), 1291–1294.
- [32] WUNSCH, B., STAUBER, T., SOLS, F., AND GUINEA, F. Dynamical polarization of graphene at finite doping. *New Journal of Physics* 8 (Dec. 2006), 318.
- [33] YU, N., GENEVET, P., KATS, M. A., AIETA, F., TETIENNE, J.-P., CAPASSO, F., AND GABURRO, Z. Light propagation with phase discontinuities: Generalized laws of reflection and refraction. *Science* 334, 6054 (Oct. 2011), 333–337.